

POLITECHNIC OF TURIN

SCUDO

Doctorate in Electron Devices – XXI Cycle

PhD Thesis

# Spintronic Devices



**Alessandro Chiolerio**

**Tutor**

Prof. Paolo Allia

**Coordinator**

Prof. Giovanni Ghione

11<sup>th</sup> February 2009



...  
la mayoría está  
recitando un rosario  
de mezquinas ambiciones  
de temores milenarios  
de inagotables astucias  
cultivando tranquila  
la horrible variedad  
de su propia soberbia la mayoría está

...  
Para quien viaja con obstinada  
y contraria dirección  
con su estigma especial  
de especial desesperanza  
y entre vomitos de rechazados  
sus últimos pasos va dando  
para entregarle a la muerte  
una gota de esplendor  
de humanidad de verdad

...  
**Álvaro Mutis**

...  
I fut en tle cinale  
I borbotte 'tli ciantun  
I saute giu ple rive  
Drocciando li bucciun

...  
Per antipaht li truni  
E saette pì de hent,  
Per prim la grela grossa  
Opura l'ahtravent

...  
Sunai da pioggi fina  
Chi ciante a meh dli pra  
Chi 'nvitte a repusasse  
E chi fait turnar maina

**Ivan Levrin**

# Summary

I report on the study of a Magnetic Tunnel Junction of the type Co/MgO/Co. The main structure was realized by a magnetron RF sputtering process, including the refurbishment and project of the prototypal deposition system itself; the growth of magnesium oxide was obtained from metallic magnesium, oxidised in an UV-generated ozone atmosphere. The junction geometry was defined by photolithographic techniques. After an annealing treatment at 350°C for 15 minutes, useful to reestablish a reticular order and to reduce mechanical stresses, a Tunnel MagnetoResistance (TMR) of 0.1% was measured at 100 K. Device/process optimisation has been done, starting from a different choice of the materials (CoCr alloy for the hard spin injector layer). Advanced numerical algorithms that have helped during the characterisation of the samples are illustrated in the latter part of the thesis, including an innovative entropic analysis that outputs a magnetic pattern stability diagram. This experimental activity has been done thanks to the Italian Ministero dell'Istruzione, dell'Università e della Ricerca and thanks to Regione Piemonte, that granted a multi-year loan to support research, within the projects: "Development of technologies for the realization of magnetic devices based on nanostructures with quantum architectures" (2003) and "Development of a demonstrator of a Magnetic Tunneling Transistor based on hybrid ferromagnet / semiconductor nanostructures " (2005), respectively.

This thesis has been written in **LATEX** using MiKTeX 2.7 open-source distribution, developed as a joint effort by all TeX user groups (<http://www.miktex.org/>).

## Acknowledgements

My most grateful thank goes to Prof. Paolo Allia, who coordinated nanomagnetism projects and offered me the opportunity to learn and research, and to Prof. Fabrizio Pirri, who leaded the Materials and Processes for Micro and Nanotechnologies group creating nearly ideal conditions to work and interact.

I wish to thank my colleagues working on magnetism and spintronics at Politecnico of Turin: Paola Martino, Salvatore Giurdanella, Paolo Pandolfi and Edvige Celasco, as well as colleagues working at INRIM, in particular Federica Celegato, Paola Tiberto, Marco Coisson and Franco Vinai, and colleagues in Parma and Ferrara.

I wish to thank ALL the colleagues working in the Materials and Processes for Micro and Nanotechnologies group, those who took a place in my hearth and those who went somewhere else.

Concludo ringraziando mamma e papà, che mi hanno accompagnato anche questa volta, le mie care zie, ed i nonni che sorridono di lassù.

# Contents

<b>1</b>	<b>Introduction</b>	<b>1</b>
1.1	Spintronics: an overview . . . . .	1
1.1.1	History . . . . .	1
1.1.2	Applications . . . . .	3
1.2	Magnetic tunneling junctions . . . . .	4
1.2.1	Physical models . . . . .	6
1.2.2	Parametres influencing TMR . . . . .	13
1.2.3	Materials . . . . .	15
<b>2</b>	<b>Prototypal Deposition Machine</b>	<b>21</b>
2.1	Refurbishment of an industrial sputtering apparatus . . . . .	21
2.2	Chamber frame and vacuum subsystem . . . . .	23
2.2.1	Materials . . . . .	23
2.2.2	Vacuum subsystem . . . . .	26
2.3	Deposition . . . . .	29
2.3.1	Sources and RF distribution system . . . . .	29
2.3.2	Sample operation and control . . . . .	30
2.4	Substrate thermal subsystem . . . . .	31
2.4.1	Vacuum radiative oven . . . . .	31
2.4.2	Dynamic electrical contacts . . . . .	33
2.5	Load-lock chamber . . . . .	35
<b>3</b>	<b>Device Engineering</b>	<b>39</b>
3.1	TMR in MgO-based MTJs . . . . .	39

3.2	Single films and rate determination . . . . .	41
3.2.1	Cobalt . . . . .	42
3.2.2	Magnesium . . . . .	48
3.2.3	Cromium . . . . .	49
3.3	MTJ: process and characterisation . . . . .	51
3.3.1	Morphological characterisation . . . . .	53
3.3.2	Electrical measurements . . . . .	54
3.4	Real-time measurements . . . . .	59
3.5	Problems presented by the first MTJ prototype . . . . .	62
3.6	CoCr alloys . . . . .	62
<b>4</b>	<b>Innovative numerical methods for data analysis and feature extraction</b>	<b>69</b>
4.1	Introduction to Vectorial and Matricial Data Handling . . . . .	69
4.2	Numerical extrapolation of curve characteristics . . . . .	70
4.2.1	Magnetisation measurements . . . . .	70
4.2.2	Magnetoresistance measurements . . . . .	72
4.3	Genetic Algorithm for Data Fitting . . . . .	73
4.3.1	Generalities . . . . .	73
4.3.2	Subroutines: roulette-wheel selection, crossover, mutation and elitism . . . . .	77
4.4	Correlation of 2-dimensional data matrices: an application to EDX and FESEM maps . . . . .	79
4.5	Regional analysis . . . . .	81
4.6	Image Registration for matricial data handling . . . . .	84
4.6.1	Introduction: MFM data acquisition . . . . .	84
4.6.2	Acquisitions with mutually orthogonal fast scan axis . . . . .	85
4.6.3	Preprocessing: thresholding and filtering . . . . .	86
4.6.4	Pair matching and inverse transforming . . . . .	88
4.6.5	Acquisitions with external magnetic field . . . . .	88
4.7	Statistical Analysis on 2-Dimensional Data Matrices . . . . .	91

<b>5 Future Developments</b>	<b>97</b>
5.1 Prototypal deposition system development . . . . .	97
5.2 Process development . . . . .	97
5.3 Numerical analysis . . . . .	98
<b>6 Conclusions</b>	<b>101</b>
<b>Bibliography</b>	<b>103</b>

# Chapter 1

## Introduction

### 1.1 Spintronics: an overview

#### 1.1.1 History

In the information era, a new promising science has been strongly addressed producing a breakthrough and diffusing in the market new technological products now ubiquitous; this science is called *spintronics*, the contracted form of spin based electronics. The 2007 Nobel prize for physics, with whom A. Fert and P. A. Grünberg have been awarded, is another clear signal that the importance of spintronics for society is worldwide understood. For more than thirty years physicists and engineers devoted their researches and efforts mostly to charge-transfer devices, developing the actual semiconductor industry and granting to it a tremendous growth rate, witnessed by the well-known Moore law: the doubling of computation speed (proportional to the transistor number per chip<sup>1</sup>) every 18 months [1]. In the far 1933 the physicist F. Mott published his innovative concept of spin dependent conduction and the possibility of considering within a ferromagnetic metal (FM) the two electron spin channels as separate noninteracting conduction ways [2]. Only forty years later experimental evidence of current spin-polarisation was reported by P. Tedrow and R. Meservey [3], carrying out experiments of tunneling between

---

<sup>1</sup>Intel ® Core<sup>TM</sup>2 Extreme QX9650 processor: 820 million transistors, over a die area of 214 mm<sup>2</sup> (2007).

FM and superconductors. In 1975 experiments on a Fe/GeO/Co junction led to the discovery of tunneling magnetoresistance (TMR) by M. Jullière [4], only verified in 1995 by T. Miyazaki and N. Tezuka [5] and J. S. Moodera [6]. This great delay was caused by the fact that the experiment was done at cryogenic temperatures; the interest on the phenomenon was purely physical since commercial electronics was and is still now unable to operate at such low temperatures, where the carriers are freezed in the semiconductor lattice. So in 1988 experiments on layered thin films of FMs alternated to a non-magnetic metal (NM) led to the simultaneous and independent discovery of the giant magnetoresistance (GMR) by A. Fert and P. A. Grünberg [7][8][9][10] (see figure 1.1). These cited

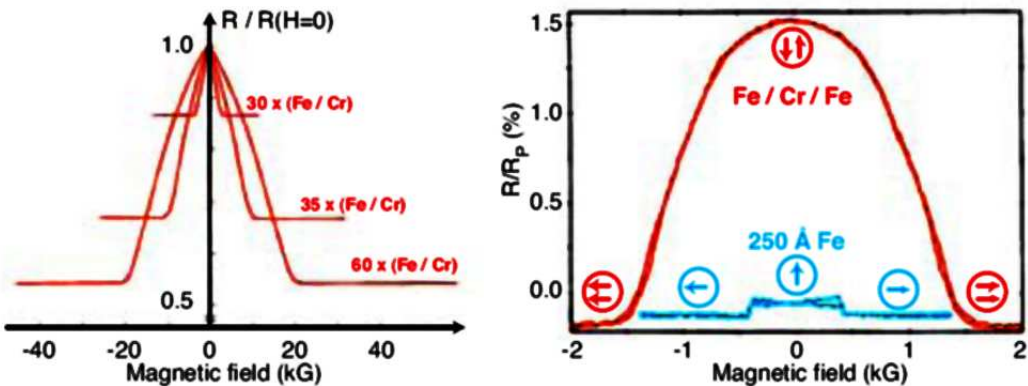


Figure 1.1. *Original findings about GMR that resulted in the Nobel prize for A. Fert (on the left, multilayered structure) and for P. A. Grünberg (right, anisotropic magnetoresistance in a thin Fe film is shown for comparison); adapted from [10].*

milestones and other published papers contributed to develop spintronics towards a better understanding of the spin polarisation, injection and diffusion in different classes of materials and to the engineering of devices that use the quantum intrinsic property of electrons to elegantly codify and elaborate binary information. Nowadays the principal application of spintronic devices is the magnetic data storage (figure 1.2), with an information density growth rate faster than the corresponding Moore law<sup>2</sup>.

<sup>2</sup>from the introduction of GMR read-heads in 1997 to 2007 a 17 month doubling of data storage density was registered, raising it from approximately 1 to 600 Gbit/in<sup>2</sup>.

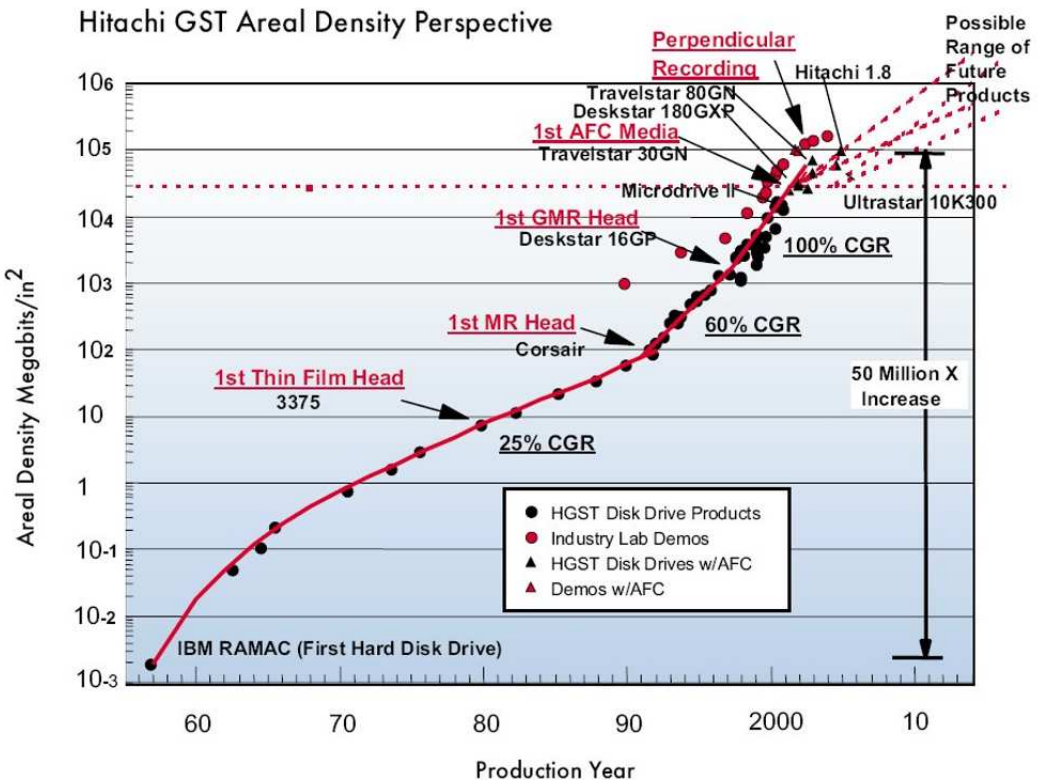


Figure 1.2. *Hitachi Global Storage roadmap; an increment of the areal density growth rate is observed in correspondence with the introduction of thin film GMR multilayers; commercial TMR read heads were not available at the time of publication (2005).*

### 1.1.2 Applications

The most important applications developed in spintronics are here presented (see figure 1.3):

- (1) spintronic logic devices, which may be based either on metals or on semiconductors; the difference between the two categories resides in the technology used to process them, which is not compatible, and in the fact that metal-based devices cannot amplify neither a charge transfer signal nor a spin transfer signal; some examples are given: the field effect spin transistor or Datta-Das transistor [11], the all-metal spin transistor or Johnson transistor [12], the hot electron spin transistor [13] and the spin-valve [14];

- (2) magnetic random access memories (MRAMs), realised with bistable spintronic logic elements, available as 16 Mb chips with 180 nm scale technology [15]; when these memories are operated using an external magnetic field the relative technology is addressed to as magnetic induced switching (MIS), while when an electrical signal injects spins rotating the magnetisation of the logic device the technology is called current induced switching (CIS);
- (3) magnetic field sensors, for example read-head sensors installed in commercial hard disks (HD);
- (4) microwave spin transfer torque nano-oscillators, devices in which a precessional mode of the magnetisation of a FM thin film is stabilised by the injection of a high density DC current and a microwave electromagnetic signal is emitted, often in the GHz range, with remarkable tuning properties of the emitted wave [16].

Starting from actual commercial applications that propose significant advantages over other available technologies, spintronic devices are addressing perhaps the most important computer subsystems: random access memories and high density non-volatile storage media. Straightforward applications will be represented by spin-based transistors and logical gates, as soon as new materials will be successfully experimented and the silicon technology will be adapted to spintronic devices. The use of spin currents in semiconductors thanks to spin-orbit coupling will enable dissipationless device operation [18], overcoming one of the greatest physical limits against size scaling, the power density growth. The road towards all-semiconductor spintronic devices goes through hybrid devices, like the hot electron transistor prototype which is composed by a tunnel barrier emitter, a semiconductor spin transport layer, a metallic spin filter and a semiconductor collector. Hybrid devices will be discussed in detail.

## **1.2 Magnetic tunneling junctions**

Rather than describing one single practical application, the main topic of this thesis is placed a step before, considering one particular physical system, the magnetic tunneling junction (MTJ) and not its applications. The MTJ is a multilayered thin film structure,

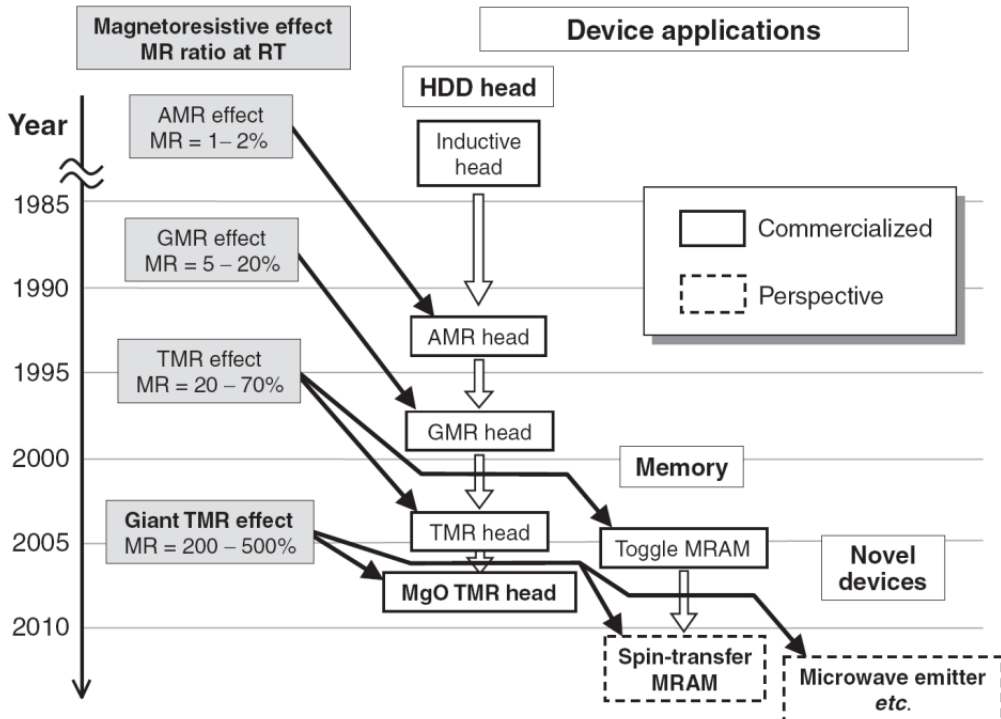


Figure 1.3. Temporal evolution of magnetoresistive devices, adapted from [17].

composed by the stacking of a inner hard ferromagnet, followed by an insulator (I) and completed by an outer soft ferromagnet. When the two ferromagnets are metallic materials, the stack is referred to as FM/I/FM. As anticipated in previous subsections the first ever realised MTJ was a Fe/GeO/Co hybrid heterostructure. Subsequently the use of amorphous alumina ( $\text{Al}_2\text{O}_3$ ) allowed to achieve much higher TMR; the following evolution was obtained by changing the morphological structure of the tunnel oxide, since some theoretical works predicted very high TMR values for completely ordered - said monocrystalline or epitaxial - oxide barriers [19] [20]; subsequently the substitution of alumina with magnesia ( $\text{MgO}$ ) contributed with a further increase in TMR, and finally the optimisation of the FM electrode materials with the introduction of CoFeB soft and CoCr hard alloys gave the last boost to MTJ fabrication technology. Figure 1.4 presents a group of early demonstrations of tunneling between FMs. In the following sections a brief description about the main physical phenomena involved in the MTJ operation,

about the technologies implemented to produce stable and reproducible MTJs and about used materials and their properties will be given.

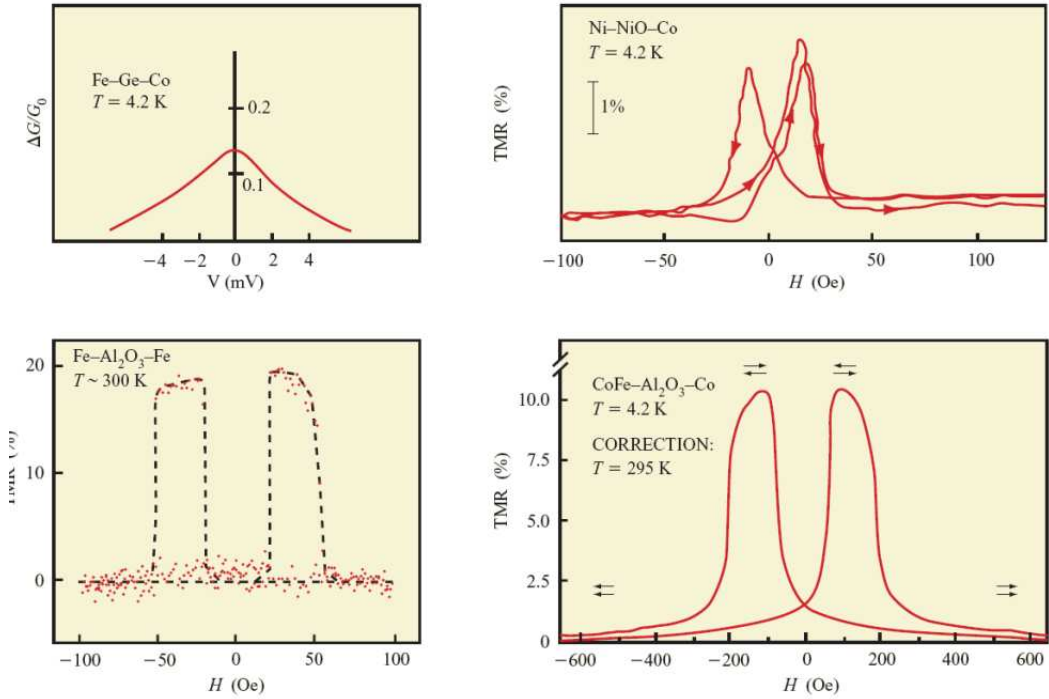


Figure 1.4. *Collection of early experimental evidences about TMR: first demonstration obtained by Jullière in 1975 (upper left panel), Maekawa and Gavfert in 1982 (upper right), Miyazaki and Tezuka in 1995 (lower left) and Moodera in 1995 (lower right), adapted from [15].*

### 1.2.1 Physical models

#### Simmons model

Spin dependent tunneling (SDT) of electrons across an insulating barrier, injected and collected by a FM (MTJ structure) has represented an extremely active and productive field, both for theoretical research communities and for experimental ones. The basis of these experiments are the first work relative to *classic* electric tunnel effect modeled in detail by Simmons in 1963 [21], showing an approximation that is still used to estimate the tunnel barrier height in modern MTJs. This model considers that a charge current

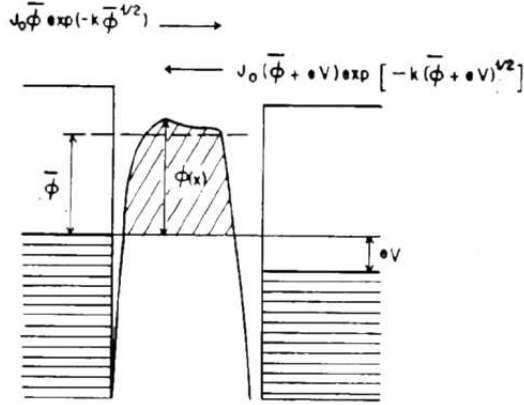


Figure 1.5. Current flow between metallic electrodes separated by an insulating barrier with complex shape  $\phi(x)$ , adapted from the original pictorial illustration in [21].

may develop across the insulator either when the incoming carriers are provided by a sufficiently high energy to overcome the potential barrier or when the said barrier is thin enough that there is a finite non-zero probability for the electron wavefunction to cross the interface. The expression for tunnel current density, without spin polarisation effects, is given by:

$$J = \frac{4\pi m^2 e}{h^3} \int_0^{E_m} D(E_x) [f(E) - (f(E) + eV)] dE_x \quad (1.1)$$

where  $m$  is the *effective* carrier mass,  $e$  the carrier charge,  $h$  the Planck's constant,  $D(E_x)$  the tunneling probability in the  $x$  direction,  $f(E)$  is the Fermi-Dirac distribution at energy  $E$ ,  $V$  the potential applied to the second electrode of the tunnel device and  $E_m$  the maximum energy achieved by itinerant carriers. A further development of the model and one obtains that:

$$J = J_0 \bar{\phi} \exp(-A \sqrt{\bar{\phi}}) - (\bar{\phi} + eV) \exp(-A \sqrt{\bar{\phi} + eV}) \quad (1.2)$$

where

$$J_0 = \frac{e}{2\pi h(\beta\Delta s)^2}, \quad A = \frac{4\pi\beta\Delta s}{h} \sqrt{2m}, \quad \beta = 1 - \frac{1}{8\bar{\phi}^2\Delta s} \int_{s_1}^{s_2} [\phi(x) - \frac{1}{\Delta s} \int \phi(x) dx]^2 dx \quad (1.3)$$

being:  $\phi(x)$  the barrier height profile,  $\bar{\phi}$  its mean,  $\Delta s = s_2 - s_1$  the barrier thickness, computed between the points where the potential balances the Fermi energy level. Equation 1.2 gives a useful instrument to estimate, as said, the tunnel barrier height starting from  $J$

- V characteristics. Figure 1.5 is the original sketch adapted from [21]. A further approximation in the linear regime, for low voltages, is given by

$$J = J_L \sqrt{\Phi} V \exp(-A \sqrt{\Phi}), \quad J_L = \frac{\sqrt{2m} e^2}{\Delta s h^2} \quad (1.4)$$

It appeared, since this early analysis, that the tunnel barrier dielectric constant  $K$  and temperature would have strongly influenced the conduction properties of the junction, as it may be noticed in figure 1.6, presenting a numerical approximation for tunnel resistance in the low voltage approximation.

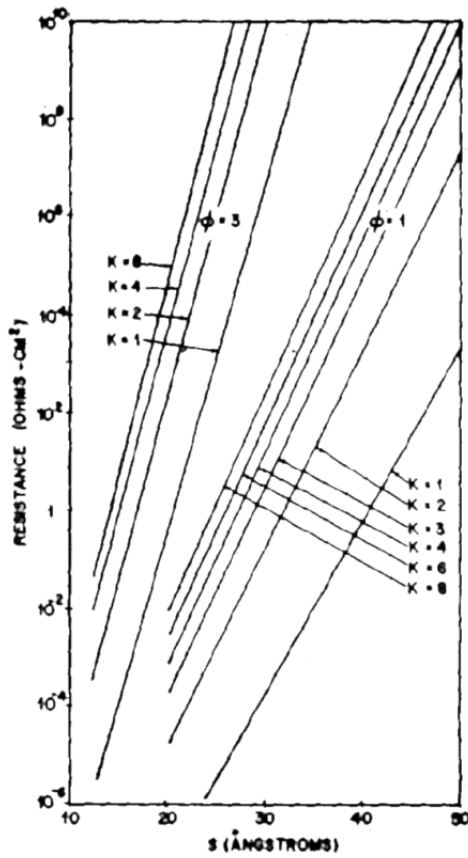


Figure 1.6. Tunnel barrier characteristics obtained with different values for the mean barrier height and dielectric constants, in the limit of low voltage signals, adapted from the original pictorial illustration in [21].

### Tedrow and Stearns models

In A MTJ the tunneling current depends on the relative orientation of the magnetisation of the two FM electrodes: due to band exchange splitting in FMs, up- and down-spin electrons have different Fermi wavevectors and hence a different tunneling probability. This means that, depending on the parallel (P) or antiparallel (AP) relative magnetic configuration of the two electrodes, one can experience respectively a high tunneling current or a low one. The relation existing between SDT and TMR was first addressed by the pioneering experiments of Tedrow and Meservey [3], where tunneling of electrons from a FM across an insulator base was detected in a thin superconducting Al layer. The density of states (DOS) in the superconductor splits into 4 sharp peaks due to Zeeman interaction between the external magnetic field and the electron spin magnetic moment. Such sharp peaks may be seen as raster detectors which give information about the separate contributions to tunnel current density by up- and down-spin electrons; since the total conductance curve is asymmetric, one obtains that the spin resolved DOS in the FM is asymmetric as well,  $\rho_{\uparrow} \neq \rho_{\downarrow}$ . Assuming separate spin channels, one can approximate the spin polarisation of the tunneling conductance with the spin polarisation of the FM DOS at Fermi level:

$$P \sim P_{FM} = \frac{\rho_{\uparrow} - \rho_{\downarrow}}{\rho_{\uparrow} + \rho_{\downarrow}} \quad (1.5)$$

The situation depicted in 1.5 is so far inconsistent: both Co and Ni DOS indicate a predominant contribution of the minority spins to the total carrier density, leading to a negative spin polarisation; experimental measurements give on the contrary a positive polarisation for the two elements. A partial solution to this problem was found by M. B. Stearns [22] by considering that the tunneling probability depends on the carrier effective mass (see equation 1.1). The electronic structure of a 3d FM is such that dispersive s bands are hybridised with localised d bands, having a stronger weight around Fermi level for the minority spin population in both Co and Ni, as indicated in figure 1.7.

Higher effective masses characteristic of localised electrons result in a fast coherence decay across the insulator and may be disregarded, while nearly-free electrons of a dispersive band crossing the Fermi energy provide the greatest part of the tunneling current. In the latter the DOS is roughly proportional to the Fermi wavevector of the carriers, and the conductance is roughly proportional to the DOS of the tunneling electrons; so it's

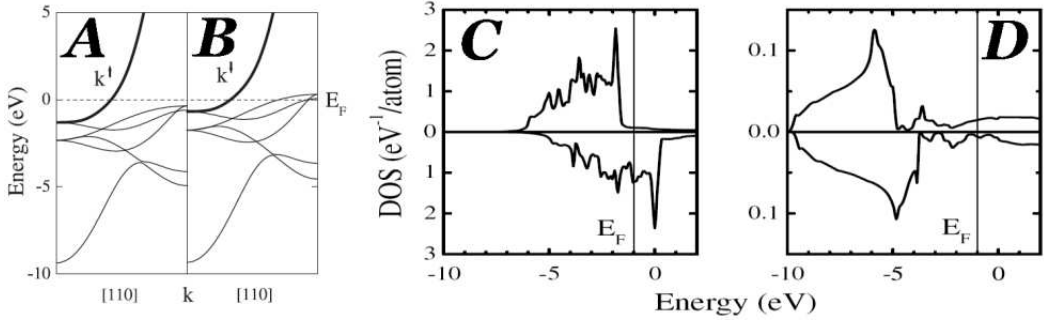


Figure 1.7. *Electronic bands in bulk fcc Ni for majority (A) and minority (B) spin electrons, showing the dispersive electron-free-like bands that give the maximum contribution to SDT (bold lines); DOS for bulk fcc Co, projected for the d orbitals (C) and s orbitals (D) for majority and minority spin electrons (top and bottom panels, respectively). Notice that the spin polarisation is opposite for the two orbitals. Figures adapted from [23].*

straightforward to write the Stearns approximation:

$$P \sim P_{FM} = \frac{k_\uparrow - k_\downarrow}{k_\uparrow + k_\downarrow} \quad (1.6)$$

where  $k_\uparrow$  and  $k_\downarrow$  are the Fermi wavevectors of electrons in the dispersive  $s$  bands for majority and minority spins respectively.

### Jullière and Slonczewski models

A further improvement of the model was achieved by Jullière [4], which assumed that

- (1) no spin-flip scattering process is produced across the insulator and transport in the two spin channels is independent (Mott's lemma);
- (2) the conductance is proportional to the product of the *tunneling* carrier DOS of the two electrodes.

The introduction of an *effective* DOS related only to the tunneling carriers transfers the problem to the definition of such a quantity. Indicating in the DOS superscript the reference electrode number (1 or 2) and codifying in the subscript the parallel or antiparallel relative alignment (P or AP) one has:

$$G_P \propto \rho_\uparrow^1 \rho_\uparrow^2 + \rho_\downarrow^1 \rho_\downarrow^2 \quad G_{AP} \propto \rho_\uparrow^1 \rho_\downarrow^2 + \rho_\downarrow^1 \rho_\uparrow^2 \quad (1.7)$$

The TMR is defined as the difference between the conductance in the P and AP states,

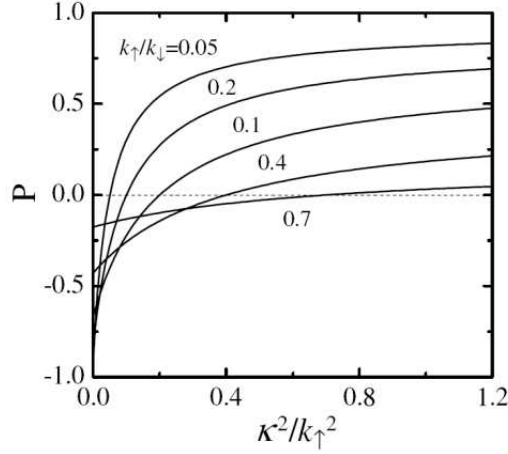


Figure 1.8. *Spin polarisation numerical evaluations based on the Slonczewski model, as a function of the normalised potential barrier height and for different majority-to-minority wavevector ratios, adapted from [23].*

normalised with respect to the conductance in the AP state:

$$TMR \equiv \frac{G_P - G_{AP}}{G_{AP}} = \frac{R_{AP} - R_P}{R_P} = \frac{2P^1 P^2}{1 - P^1 P^2} \quad (1.8)$$

where the effective spin polarisation in the  $i$ -th FM electrode is defined as follows:

$$P^i = \frac{\rho_{\uparrow}^i - \rho_{\downarrow}^i}{\rho_{\uparrow}^i + \rho_{\downarrow}^i} \quad (1.9)$$

This model overestimates slightly the spin polarisation of real MTJs: some phenomena are still to be included in the physical model of the device, particularly concerning the junction barrier interface and insulator properties. Furthermore, experimental results published by Jullière were never reproduced by other researchers.

A more accurate modelisation of the spin resolved tunneling conductance in MTJs was elaborated by J. Slonczewski in 1989 [24]. His approach consists in the solution of the Schrödinger equation over a symmetrical domain depicting the MTJ, imposing the matching of the carrier wavefunctions across the insulator barrier; in the limit of a thick barrier, the conductance turns out to be a linear function of the cosine of the angle  $\Theta$  between the

magnetisation of the FMs:

$$G(\Theta) \propto (1 + P^2 \cos(\Theta)) \quad (1.10)$$

where the *effective* polarisation of tunneling carriers is written as follows:

$$P = \frac{k_\uparrow - k_\downarrow}{k_\uparrow + k_\downarrow} \frac{\kappa^2 - k_\uparrow k_\downarrow}{\kappa^2 + k_\uparrow k_\downarrow} \quad (1.11)$$

In equation 1.11 the wavefunction decay constant has been introduced, which contains information relative to the potential barrier height  $U$  with respect to the Fermi energy  $E_F$ :

$$\kappa = \sqrt{\frac{2m(U - E_F)}{\hbar^2}} \quad (1.12)$$

What is worth mentioning is that the polarisation is now dependent on the barrier height (see figure 1.8: in the limit of an infinite barrier, one recovers the Jullière model 1.7; for finite barriers, the effective polarisation is reduced and even changes sign, well representing experiments that report negative values of TMR, for example found by Fert and his group studying Co FMs and SrTiO<sub>3</sub> barriers [25]. This has been the first clear evidence that the

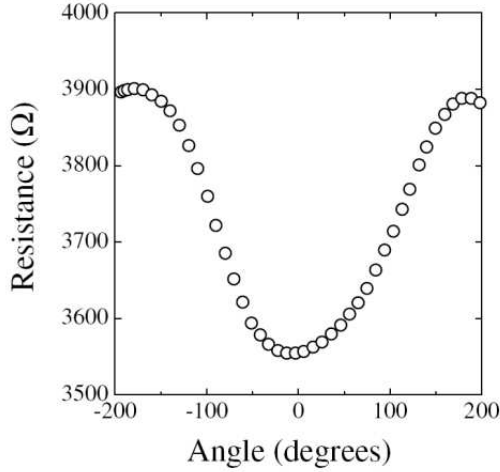


Figure 1.9. Angular dependence of TMR for a CoFe/Al<sub>2</sub>O<sub>3</sub>/Co junction measured with a magnetic field lower than the hard layer coercive field but higher than the free layer one, adapted from [23].

spin polarisation does not represent an intrinsic property of the ferromagnets. Equation 1.10 has been verified experimentally by Moodera on a CoFe/Al<sub>2</sub>O<sub>3</sub>/Co junction in 1996 [26], as shown in figure 1.9.

### 1.2.2 Parametres influencing TMR

In order to visualise and measure the TMR of an MTJ it is necessary to reproduce and stabilise the P and AP device states: one can provide an external magnetic field, for example, or couple the trilayer with some functional transducers that are optically or electrically operated and help in rotating the magnetisation. In both cases, the system is realised in such a way that the electrodes feature a different coercive field; one is usually a hard layer (CoFe, CoCr or thin Co, Fe, Ni) and the other a soft layer (CoFeB, FeNi or thick Co, Fe, Ni). The dipolar interaction that tends to lower the total energy by magnetically coupling the two electrodes, particularly when the difference between coercive fields is small, may be further reduced by adding an antiferromagnetic pinning layer (AFM) that pins the magnetisation of that FM which is placed in direct atomic contact.

TMR shows a strong dependence on the applied voltage, featuring a symmetric drop;

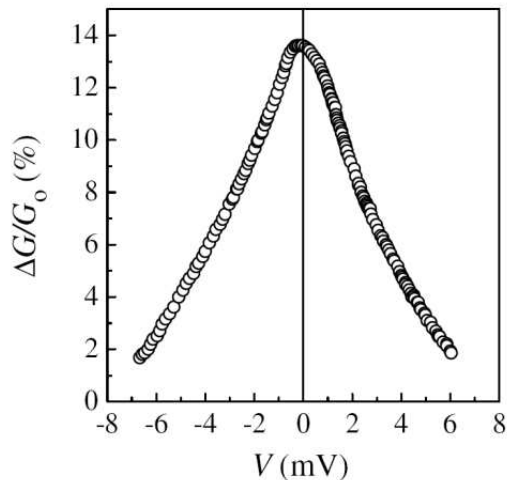


Figure 1.10. *The original finding of TMR by Jullière, bias effect on the device conductance, adapted from [23].*

the full width at half maximum (FWHM) was found to be 3 mV only in Jullière's MTJ (see figure 1.10) [4] and has been increased, improving the junction quality, up to 500 mV [27]. The bias dependence is ordinarily stronger for the AP state than for the P one, as indicated in figure 1.11. The cause for this steep drop is still under debate and no unambiguous correlation has been established between the bias dependence of TMR and

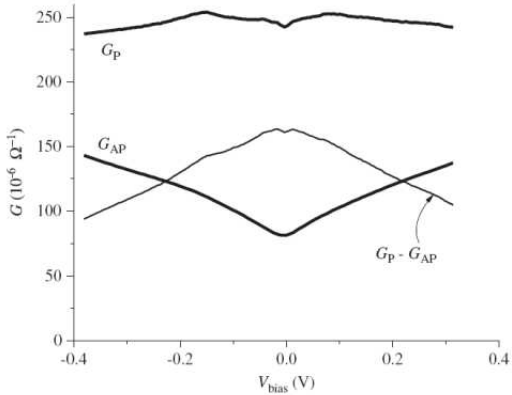


Figure 1.11. *Bias dependence of a MgO-based MTJ conductance, resolved for both parallel and antiparallel magnetic configurations (bold curves), as well as for overall conductance (light curve), revealing a different behaviour in the two states; adapted from [28].*

any particular mechanism. One possible cause may be found in magnons excitations that develop at FM interface, causing inelastic carrier scattering [29]. Another possible cause is the energy dependence of the band structure in the electrodes [30], which should be dependent on the electrode material; an experiment by LeClair and his group demonstrated the energy-band dependence using both fcc and hcp Co [31]. Finally, and most interestingly, it may be caused by trap states localised at the junction interface; this is supported by the experiment of Wulfhekel and his group [32], consisting in a vacuum tunneling of electrons from a magnetised scanning probe to a FM surface and showing a constant TMR up to 0.9 V bias. The vacuum eliminates the problem of a defective interface. By vacuum annealing above 350°C, the elimination of trap states and optimisation of the TMR bias dependence has been also demonstrated on MgO barrier MTJs [33].

The temperature dependence of TMR greatly exceeds the temperature dependence of non magnetic tunnel junctions; it tends to decrease for all kinds of MTJs, of about 25% from 4.2 to 300 K because of the corresponding decrease of both surface magnetisation and spin polarisation induced by the spin-wave excitations [34]. The model, which reproduces with enough care the TMR behaviour, assumes a  $T^{3/2}$  Bloch law (see figure 1.12). Another mechanism thermally activated is spin-flip scattering caused by magnetic impurities localised at the junction interface [35]. Heating in MTJs is a problem of great

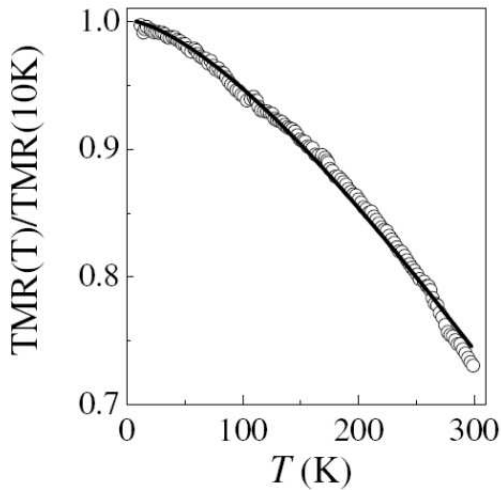


Figure 1.12. Temperature dependence of TMR for a Co/Al<sub>2</sub>O<sub>3</sub>/Co junction, showing both experimental data (open circles) and theoretical model (line); adapted from [23].

importance, particularly for those devices working as STNOs, where a condition of high bias and high current density is used to transfer spin in the soft free layer. Recent studies have shown that in those condition a heating of more than 400 K is generated by a *DC* current of only 1 mA.

Coulomb blockade effects develop in MTJs where the tunnel barrier has been grown on a nanosized FM cluster layer, such as Co nanoparticles embedded in Al<sub>2</sub>O<sub>3</sub> [36]; in this regime, tunneling towards the ferromagnetic islands is limited by the charge already stored in the clusters. A general increase in TMR has been found for such systems.

### 1.2.3 Materials

Motivated by the very high tunneling spin polarisations achievable by so called half-metallic materials, that feature only one spin channel occupied at Fermi energy with a consequent complete polarisation, many works have investigated those compounds that are expected to behave like half-metals: Heusler alloys, oxides and sulfides. Successful attempts individuated an appreciable TMR with NiMnSb [37], La<sub>0.67</sub>Sr<sub>0.33</sub>MnO<sub>3</sub> (LSMO) [38] and CrO<sub>2</sub> [39]. However, such compounds are expensive, difficult to grow and often

feature a Curie temperature below 300 K.

For what concerns standard metallic electrodes, research has been done towards the realisation of monocrystalline epitaxial stacks, resulting in a semi-epitaxial multilayer with only the first electrode completely ordered. In such structures a strong dependence of TMR on the crystallographic orientation has been found [27]: the structure Fe/Al<sub>2</sub>O<sub>3</sub>/CoFe shows, depending on the first layer orientation (100), (110) or (211), different TMR and a different influence of the amorphous alumina layer thickness (see figure 1.13). Theoretical

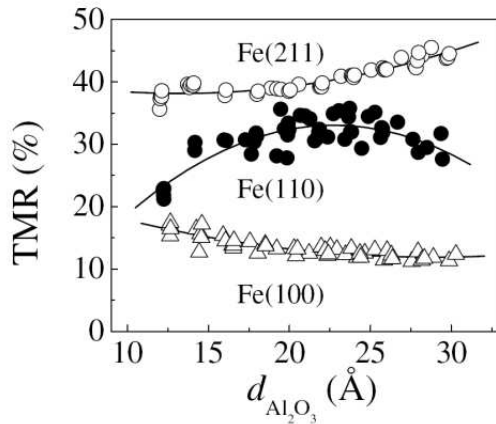


Figure 1.13. *Effect of the crystal orientation for epitaxial Fe bottom electrode on the TMR of a CoFe/Al<sub>2</sub>O<sub>3</sub>/Co junction, in function of the amorphous barrier thickness; adapted from [23].*

works suggest that for fully epitaxial Fe(100)/MgO/Fe(100) MTJs the AP conductance should drop to zero, eventually approaching TMR values as high as 15000% [40].

Since it is possible that small domains in the high coercivity hard ferromagnet switch at low fields, without any possibility of returning to the original state during the operation of the MTJ, it is common to use a pinning AFM layer or a synthetic antiferromagnet (SAF), consisting in a metallic stack of two FM separated by a diamagnetic metal, whose thickness is carefully chosen in order to promote exchange coupling and stabilise the AP state (which has the lowest energy). For example a common SAF is CoFe/Ru/CoFe, where Ru is 7 to 8 Å [41], producing no net magnetic bias on the free soft layer. Figure 1.14 provides a sketch of the evolution in device engineering, starting from single layer FMs, showing the intermediate step corresponding to the introduction of an AFM pinning layer

and finally presenting the SAF structure.

Tunnel barriers have been realised principally in  $\text{Al}_2\text{O}_3$  [5] and  $\text{MgO}$  [42], including

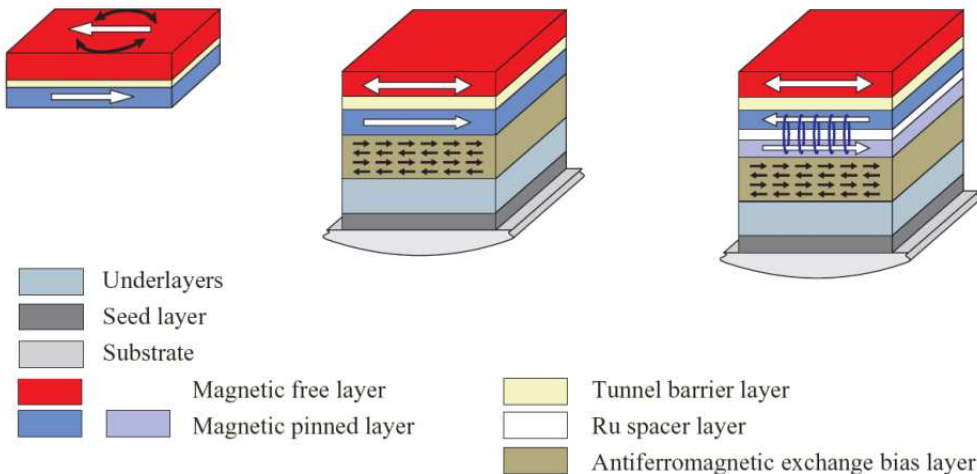


Figure 1.14. *Evolution of tunnel junction engineering, starting from a simple trilayered structure (left) with a soft (red) and a hard (blue) electrode; exchange coupling of the hard electrode with an AFM pinning layer (middle, pointed by black antiparallel arrows); elimination of dipolar interaction between pinned layer and free layer by antiparallel coupling in a SAF structure (right, pointed by blue rings).* Adapted from [15].

some hybrid materials containing  $\text{Ta}_2\text{O}_5$  [43],  $\text{SrTiO}_3$  [25] or  $\text{NiO}$  and other insulators such as  $\text{HfO}_2$  [44],  $\text{AlN}$  [45],  $\text{ZrO}_2$  [46],  $\text{EuS}$  [47] and  $\text{Ga}_2\text{O}_3$  [48]. Figure 1.15 shows the evolution of the TMR with respect to the tipology of tunnel barrier, considering the two most important oxides that gave so far the best results: alumina and magnesia.

For what concerns the exploration of the TMR dependence on interfaces, experiments have been realised inserting ultrathin *dusting* layers between the electrode and the insulator, both below the barrier and above it. LeClair found that only one monolayer (ML) of Cu is sufficient to exponentially decrease almost to zero the TMR [49], demonstrating that MTJs are extremely sensitive to the atomic arrangement across the tunnel barrier. An oscillatory dependence of giant TMR (GTMR) on the barrier thickness has been also observed in an epitaxial  $\text{Fe}/\text{MgO}/\text{Fe}$  system [50], as proposed in figure 1.16.

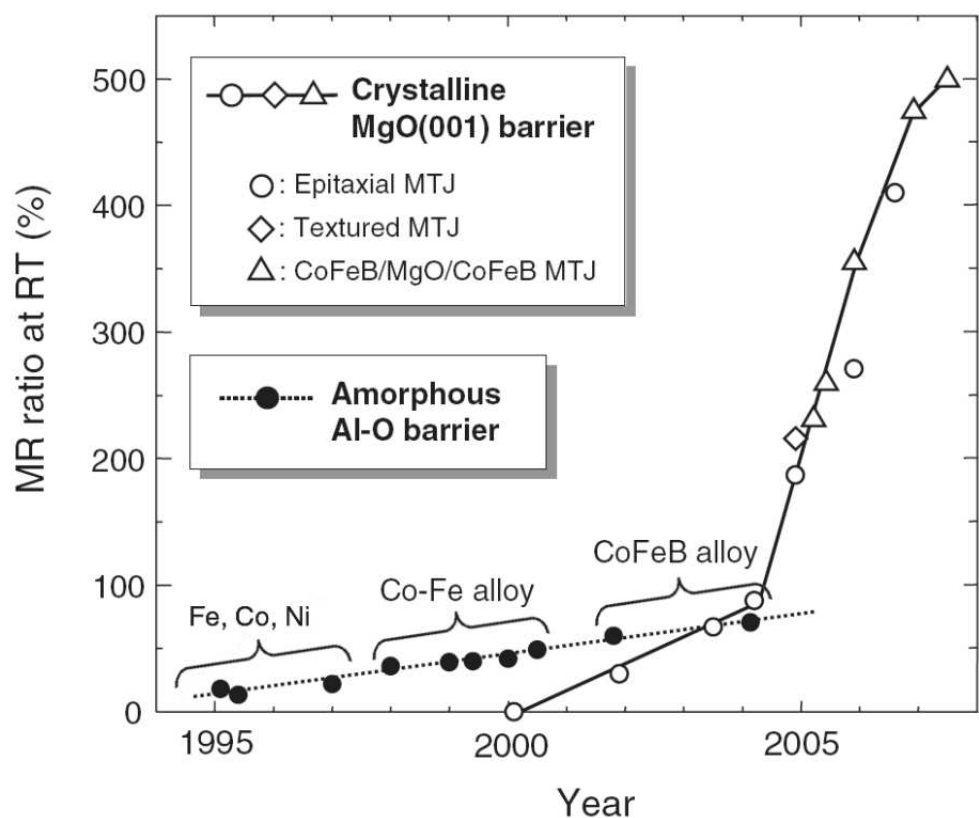


Figure 1.15. Temporal evolution of TMR with different tipologies of FM electrodes and crystallographic structures of alumina and magnesia tunnel barriers; adapted from [17].

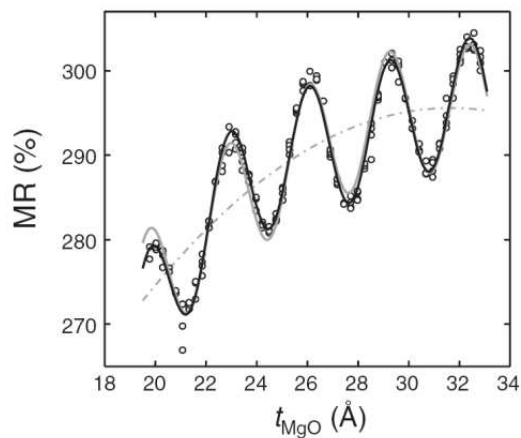


Figure 1.16. Periodic oscillations in the TMR for an epitaxial Fe/MgO/Fe system as a function of the barrier thickness; overimposed: quadratic background fitting (dashed grey), short period least-squares fitting (solid grey) and sum of the two fits (solid black). Adapted from [17].



# **Chapter 2**

## **Prototypal Deposition Machine**

Vacuum is instrumental for the realization of high quality thin films in many fields of both science and technology [51][52]. In particular the actual commercial MgO-based MTJs fabricated for the MRAM and HD read heads production have been first demonstrated and then optimised with an industrial multitarget sputtering system, the Canon-Anelva C-7100 [17]. Considering the cost of a sophisticated commercial high-end deposition system, we decided to re-utilise an old system with some substancial improvements and implementations. The three-sources RF magnetron sputtering apparatus in use at Physics Department, during the three-year period of this thesis, has been completely refurbished and brought in operative condition exploiting a high vacuum and cleanliness level and implementing multiple operative functionalities that are required for complex multilayered structure realisation.

### **2.1 Refurbishment of an industrial sputtering apparatus**

The old sputtering was equipped with a triple source for the reactive deposition of oxides and with a specific vacuum oven, used to grow textured complex oxides, positioned in the upside down configuration; the process gas was Ar, the radiofrequency source was operating at 13.56 MHz. Three types of vacuum gauges were connected to the vessel: a thermocouple (Pirani) low vacuum sensor, a capacitive sensor to assist the deposition step and a hot cathode (Bayard-Alperth) high vacuum sensor. The system was affected by the

following problems:

- (1) the stainless-steel vessel was oversized, having a volume of 423 litres, while the effective volume used during operation was much narrower; evacuation hence resulted very time-consuming;
- (2) the cooling plate installed beneath each cathode was suffering from corrosion and was potentially subject to vacuum leakage and water injection into the vessel;
- (3) considering cathode dislocation inside the chamber, the sample holder positioning system was unable to accomplish a full 360° rotation over the sources without breaking its electrical connections;
- (4) vacuum seals and fluoroelastomeric gaskets were weak, oxygen diffusing from the dynamic feedthrough could contaminate sputtered metal films;
- (5) no load-lock chamber was installed and removing/inserting each sample required the vacuum condition to be broken.

The following solutions have been specifically conceived to solve the problems:

- (1) a new stainless steel vessel has been produced re-utilising the old basement with flanges and cathodes, with a volume of 154 litres and a corresponding reduction of -275%;
- (2) a special closed circuit brass cooling plate has been designed and realised, to be inserted inside the magnetron; neither water injection nor vacuum loss would be possible;
- (3) a special dynamic electrical contact system has been designed to allow a full 360° rotation of the sample holder;
- (4) where possible, fluoroelastomeric gaskets have been replaced with copper flanges (CF), which are suitable for ultra-high-vacuum (UHV) applications; leaks have been detected and fixed;

- (5) a load-lock chamber has been installed on a spare flange, isolated from the main vessel by an electro-pneumatic gate valve.

All technological implementations on the prototypal sputtering machine and technical projects were done in collaboration with Mori Meccanica S.r.l. (Parma, Italy). Figure 2.1 represents the new deposition system during assembly; figure 2.2 is the original technical project elaborated by Eng. Paolo Mori. A number of original low cost and high yield solutions, as will be described in the following sections, have been experimented besides the critical points worked out above. For reference, see [53].

## 2.2 Chamber frame and vacuum subsystem

The chamber appears as a main vessel with some UHV fittings and flanges. On the front side, seven flanges with different diametres are present: three of them (CF16, CF40, and CF150, where the number denotes the pipe diametre in millimetres) are blind, two other flanges (CF40, CF100) have a glass inspection window. A capacitive vacuum sensor is installed on a CF16 flange, whereas the last one (CF200) connects the main vessel to the load-lock chamber via an (UHV) gate valve (VAT, stainless steel body). The vessel ceiling may be lifted by means of a rotating-screw motor actuator that can be both remotely and manually operated. The chamber basement is provided by a KF200 flange with a throttle valve used to partialise the original pumping group, keeping a control on the residual pressure. Samples are transferred to the holding slit inside the process chamber via a magnetic horizontal manipulator (CF40 flange), while an angular joint allows tilting of the transfer axis on both a vertical and a horizontal plane (simultaneous movement is permitted).

### 2.2.1 Materials

Materials used to realize high-temperature-resistant components, such as the specimen holder and oven frame, must be characterised by very low outgassing and diffusion rates, high resistance to oxidizing atmospheres and to thermal shock/temperature cycles, as well as low raw material costs, weldability and workability. The metal selected for the

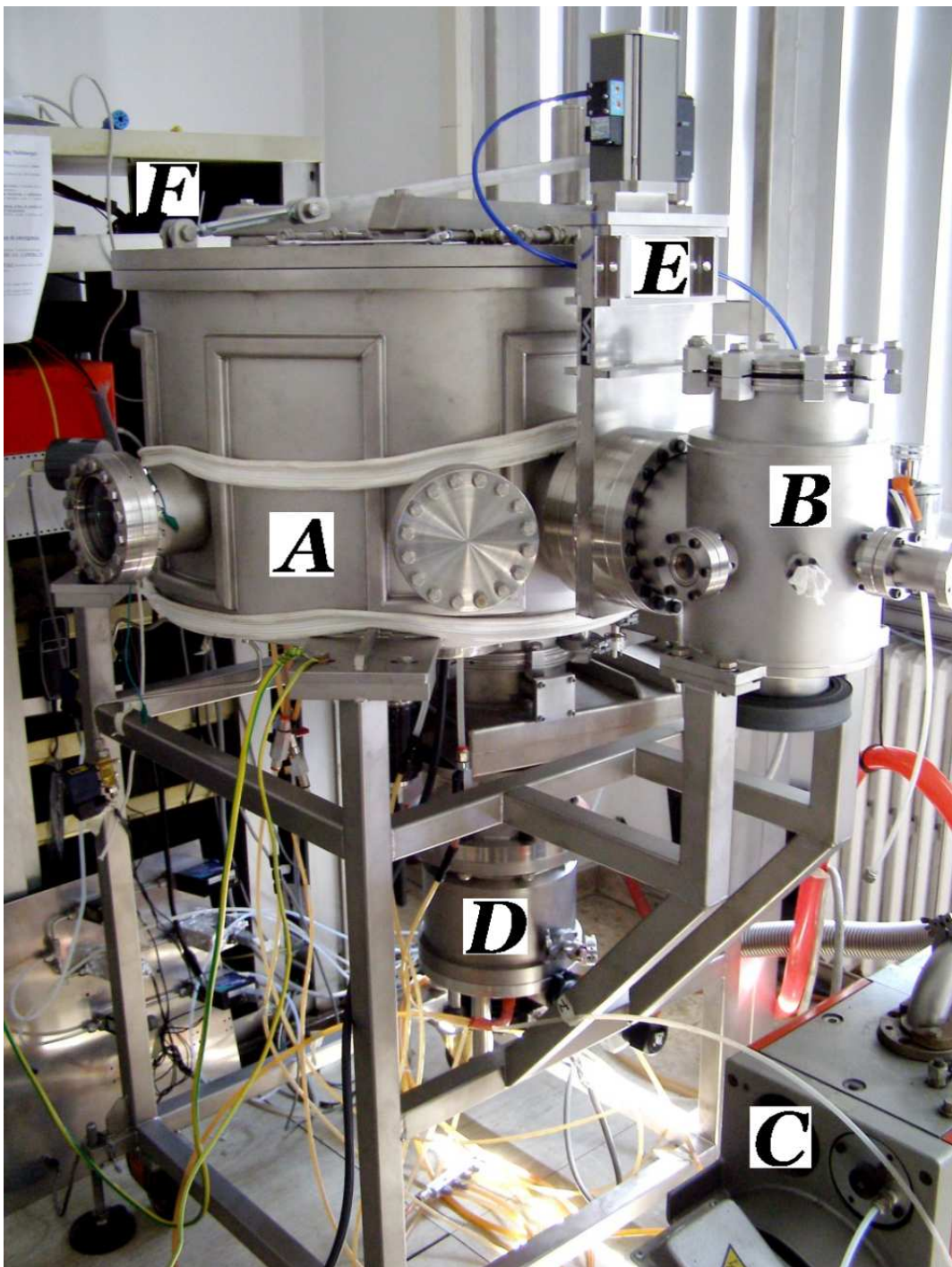


Figure 2.1. Picture of the new deposition system during assembly. A) stainless steel main vessel with cooling serpentines and heating ribbon; B) load-lock secondary chamber; C) two stage rotary pump for rough vacuum; D) high-throughput turbomolecular pump with high conductance arrangement, for secondary vacuum; E) electro-pneumatically operated stainless steel gate valve; F) control rack.

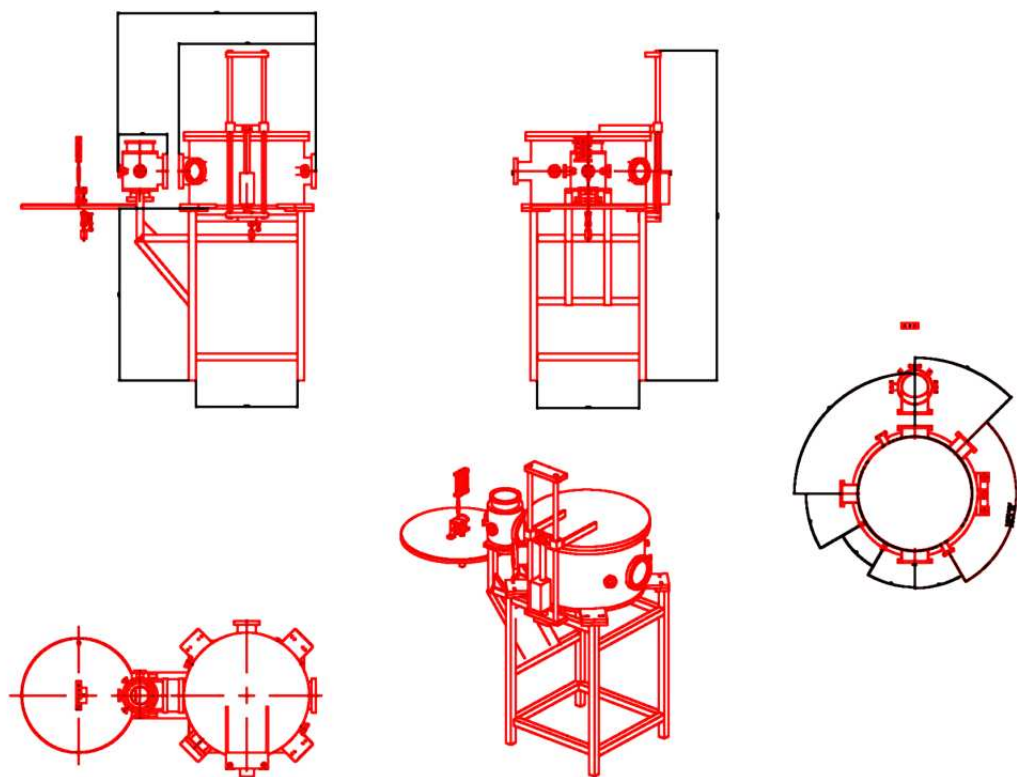


Figure 2.2. Lateral projections and isometric 3-dimensional draws of the new system, courtesy of Eng. Paolo Mori.

fabrication of the vessel wall, gearbox, shafts, and target screens is austenitic stainless steel AISI 316L<sup>1</sup>. Austenitic steels of the 300 series, compared to martensitic or ferritic stainless steels (400 series), give the opportunity to work from cryogenic to high temperatures with no ductile-to-fragile transition, are easily workable, they are not ferromagnetic and they don't shunt the field distribution within the vessel, generated by the magnetron sources. Other eligible materials would have included high-temperature stainless steels, which in turn are Ni-rich alloys and feature ferromagnetism; rapid steels, strongly alloyed with refractory elements such as W, Nb, Mo, Ti which in turn are much more brittle than austenitic steels; ferritic stainless steels, which in turn show dramatic embrittlement at operating temperatures of 600° C; extremely low interstitial stainless steels (ELI), which are actually superior to AISI 316L but are in turn much more expensive and poor in workability [54]. The inner surface of the vessel has been mirror-polished to minimise the outgassing rate. Steel is the best choice for structural components; particular applications may though require either other metals or brittle ceramics or soft polymers instead; they will be addressed case by case in the following subsections.

### 2.2.2 Vacuum subsystem

A proper thermal treatment, said *baking* of the walls, is usually done close to 100° C for some hours to promote desorption of condensed species and mostly of water molecules, using a heating ribbon with aluminum foil thermal shield. Heating at higher temperatures, a method frequently utilized to reduce the final pressure once at room temperature by desorption enhancement, has been recently found to be an inadequate step [55] [56]. These studies, supported by technological developments required for high-energy particle physics, found that prolonged heating at high temperatures excites hydrogen from deep states to surface states, increasing the amount of H<sub>2</sub> desorbed molecules; in fact in UHV applications the residual atmosphere composition has been found to be mainly H<sub>2</sub> with He and H<sub>2</sub>O. The predominant source of H<sub>2</sub> molecules has been found to be the metal-solubilised portion of said gas, source that formerly was believed to be the metal-diffused portion having an atmospheric origin; this means that very thin vessel walls are better than

---

<sup>1</sup>typical composition: C 0.02%, Cr 17.00%, Ni 13.00%, Mo 2.30%, S 0.02%, P 0.04%, Si 1.00%, Mn 2.00%, Fe 64.62%, also identified by the UNI code X 2CrNiMo1712).

massive ones. Fluoroelastomeric o-rings are used in those flanges whose size is either too big or not standard (the ceiling seal and the custom magnetron are examples). Such o-rings have been spread with APIEZON ® H grease to promote vacuum seal, resistant at high temperatures (maximum allowed baking at 240° C). The fluoroelastomer by itself, when charged under compressive stress and brought to rather high temperatures (> 100° C) may undergo to creep and loose its elastic response, becoming useless. A cooling circuit was created by a steel serpentine to maintain the temperature of the wall chamber at about 12° C during operation, allowing to reach the best pressure conditions, which may be quantified in  $9 \cdot 10^{-8}$  Torr, corresponding to a mean free path of the molecules/atoms in the residual atmosphere of  $\approx 1$  km; the evacuation time is in the order of 2 hours to reach a pressure  $< 5 \cdot 10^{-7}$  Torr. Periodical vacuum tests are scheduled on the vessel, consisting in a static pressure curve acquisition, after the isolation of the chamber from the evacuation group (see figure 2.3). Using the residual gas balance one can evaluate the outgassing level of the system:

$$P_{limit}\Sigma = -V\frac{dp}{dt} + O_{outgas}S \quad (2.1)$$

where  $P_{limit}$  is the lowest recorded pressure ( $9 \cdot 10^{-8}$  Torr),  $\Sigma$  is the pumping speed (1000 l/s),  $V$  is the vessel volume (154 l),  $\frac{dp}{dt}$  is the slope of the curve shown in figure 2.3 ( $6.4 \cdot 10^{-9}$  Torr/s) and  $O_{outgas}S$  is a leak term, due to outgassing from the metals, ceramics and polymers placed inside the chamber, on the active surface  $S$  ( $5 \text{ m}^2$ ). This leads to an effective outgassing rate of  $\approx 10^{-13}$  Torr · l/s · cm<sup>3</sup>, which is comparable with data available for the same material in literature, measured after degassing<sup>2</sup> in vacuum at 200° C for 2 h; the composition of outgassed flow was found to be: 94.74% H<sub>2</sub>, 2.10% CO, 1.58% H<sub>2</sub>O, 1.05% Ar and 0.53% CO<sub>2</sub>, in [57].

The vacuum subsystem is formed by two primary vane pumps (Edwards, 80 m<sup>3</sup>/h, KF40-flanged to the chamber; and Leybold, 16 m<sup>3</sup>/h, KF25-flanged to the load-lock) and one turbomolecular pump (Leybold, 1000 l/s ISO-K200 flanged). This system allows either chamber evacuation or the establishment of a regime pressure to control the Ar flux during the sputtering process. Both the main process chamber and the load-lock are connected with a mass flow control (MFC) gas supply that introduces argon for plasma generation, nitrogen for venting or oxygen for reactive processes, with a lower sensitivity bound of 1

---

<sup>2</sup>this term indicates an intentional outgassing of the system, obtained raising its temperature.

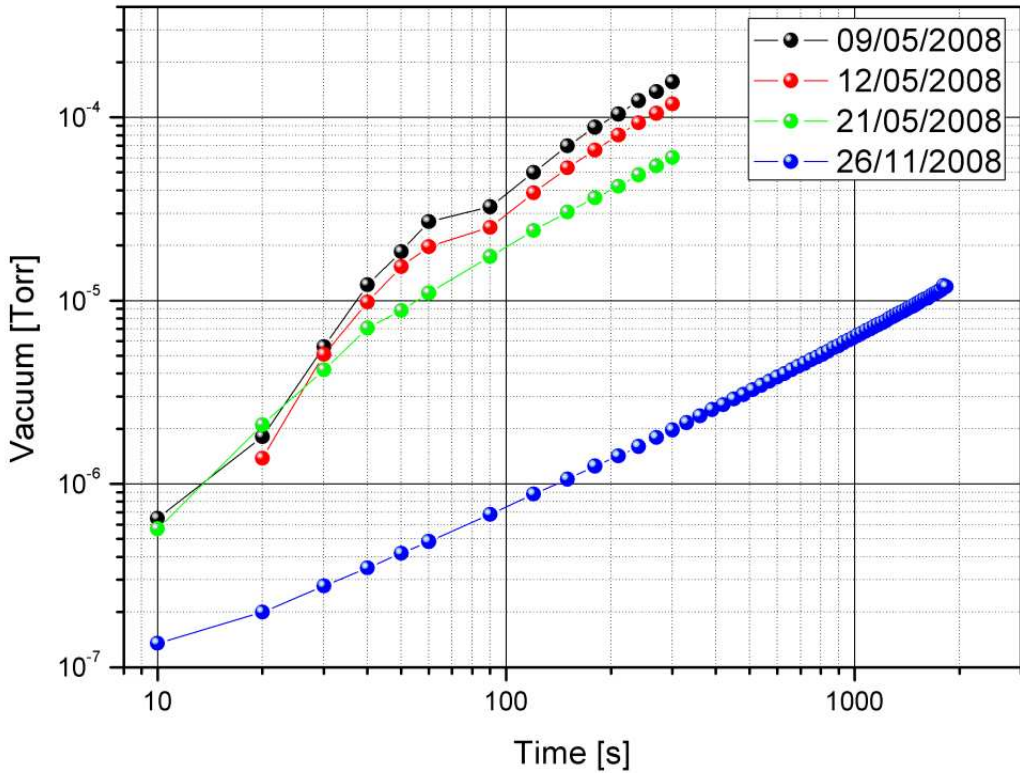


Figure 2.3. Outgassing curve showing different tests during 2008 operations; black and red curves have been acquired on the same system, but respectively before and after the baking, which has the effect of vertically translating the curves; the green curve shows a performance increment due to mirror-polishing of inner small parts; finally the blue curve corresponds to a long baking at  $90^{\circ} \text{ C}$  with one month of continuous operation of the evacuation subsystem.

sccm. Every gas line has been equipped with a special couple of cartridge filters: the first is a harsh sieve to remove microparticulate and the last is a coalescing porous ceramic barrier that dries the process gas.

## 2.3 Deposition

### 2.3.1 Sources and RF distribution system

The three sputtering sources are composed of an external stainless steel shell and an inner aluminum cylinder, containing the hydraulic cooling plate, the RF antenna, the copper target holder directly exposed to the vacuum and for two out of three the magnetron equipment. Since magnetron increases the yield, ultra-thin Mg layers are deposited using the simple RF source. Electrical insulation is provided by thick PTFE foils. The magnetron consists of a low-carbon steel disk surmounted by an outer cylindrical ring and an inner cylinder. An outer NdFeB permanent magnet ring (remanence  $\approx 1.2$  T) is surmounted by a low-carbon steel yoke that guides flux lines toward the vacuum zone, whereas the inner low-carbon steel cylinder contains a NdFeB permanent magnet tablet whose polarity is chosen to close the flux lines generated by the outer ring. In the dismissed system, the cooling-water circuit was directly placed inside the magnetron, which caused corrosion problems. Actual improvement consists in using a brass closed cooling plate, within the outer magnetic ring and inner magnetic cylinder, composed by two disks with an engraved path for the water flow. Each cooling plate is in thermal contact with the copper target holder via a special polymeric thermally conductive bi-adhesive; figure 3.12 (F) shows the inner part of a magnetron without the copper target holder. The target holder has been designed with an inner diametre in excess by some 0.1 mm with respect to the nominal 4-inches size, to easily install and remove the target from the source (see figure 2.6 D). The thermal and electrical contact with the holder is guaranteed by three copper slits that clamp the target tightly. Parts whose surfaces are exposed to vacuum have been manually mirror-polished.

RF signal is provided by a Dressler Hilight<sup>TM</sup> 133, with a maximum output of 300 W @ 13.56 MHz; a manual matching box is connected to the generator by a shielded power coaxial cable RG214 and subsequently directed to an electrically-operated RF switch that diverges the signal to the different cathodes. RF components have been assembled on the prototypal machine with a great economy.

### 2.3.2 Sample operation and control

The sample holder is positioned over the operated plasma source by two coaxial rotating axes both standing on the basement: the first one rotates the oven with the sample holder slit, whereas the second one is connected to a shutter, a circular steel shield whose circumference has been cut by one sector to allow the sputtered atoms flow to reach the substrate. Another axis transmits the torque provided by the DC brushless motor; mechanical coupling between the latter and the two coaxial shafts is accomplished by a group of bronze gears (see figure 3.12 D and E), installed inside the vacuum chamber, whose reciprocal position may be changed by manual z-axis regulation available on the feedthrough. The particular choice of bronze, regardless of its low melting point and closeness to upside-down radiative oven (it is partially shielded by the steel gearbox cage), was necessary to provide self-lubricating gears, since neither fluid (grease) nor solid (graphite, molybdenum sulphide) lubricants are allowed in a vacuum chamber. By shifting the position of the motor shaft with respect to the coaxial shaft, it is possible to select the desired coupling: motor and inner shaft (sample), motor and outer shaft (shutter), or motor and both shafts. The operator is thus free to choose whether to move just the heated substrate holder, or the shutter, or the two parts together. A fixed substrate position is useful in the case of deposition of a single-layer thin film, because the shutter may be used to properly control the deposition time. When the shutter is used as a mask carrier to implement the shadow-masking technique, a decoupled rotation of the two parts is required. On the contrary, synchronous rotation of the shutter and sample holder is required when growing a multilayered structure. This original solution reaches two goals: it's cost-effective since only one rotational feedthrough is installed to operate two shafts and it's safe since there is only one critical seal instead of two. Torques as high as 16 N·m are provided by an Oriental Motor BLF460 C-100 DC brushless unit (60 W) equipped with a parallel shaft reduction gear and digital operating panel, providing a positioning control accuracy within 20 minutes of a degree (6 mrad).

A desktop PC with LabView® software and a National Instrument NI USB-6009 analogue/digital input/output USB module, featuring 8 parallel inputs and 14 bits accuracy, is used to remotely control the machine. A customized workspace gathers information on the physical variables detected by sensors (e.g., pressures, DC bias, gas flows) and on the

status flags relative to the valves, chamber opening mechanism, and cooling circuit. All this information is recorded in a log file. An automated procedure routine allows the user to program the deposition steps, choosing the deposition time, source, number of layers, and set of mask to be used. A manual operation of the horizontal transfer feedthrough and control of the gate valve is still necessary to introduce a specimen inside the load-lock and transfer it to the process chamber, as well as to do the reverse action.

## 2.4 Substrate thermal subsystem

### 2.4.1 Vacuum radiative oven

A radiative oven is placed upside-down in the main vessel; maximum annealing temperature is 1200° C. The heating group consists of a sinterised boron nitride body, with two different resistive graphite serpentines buried in the nitride; a thin film of pyrolytic boron nitride covers the outer part of the oven. Electrical power is fed by two insulated and shielded multiwires: high density sintered alumina beads are used as electrical insulators while an aluminum thin foil covers the wires arranged in an helical shape. The aluminum shield is grounded on the inner surface of the vessel, while the oven is put at a floating potential, since the beam which holds it is insulated from the inner shaft (see figure 2.6, A). A chromel-alumel K type thermocouple is placed in the centre of the oven and its signal is used as a reference for the PID to control the oven duty-cycle. Since in molecular regime convection phenomena are inhibited and a great thermal inhomogeneity may rise within the vessel, a long thermalisation period has been waited for in a relatively high partial pressure of inert gas (Ar, 1 Torr) and a correlation with a nisil-nicrosil N type thermocouple, directly placed in contact with the sample, has been built (see figure 2.5). The rather good linear correlation that has been found between the two sensors demonstrates that the sample may be modeled as separated from the oven by a linear thermal resistance mounted in series, with a dissipation factor of roughly  $0.86 \pm 0.03 \text{ } ^\circ\text{C set} / \text{ } ^\circ\text{C read}$ .

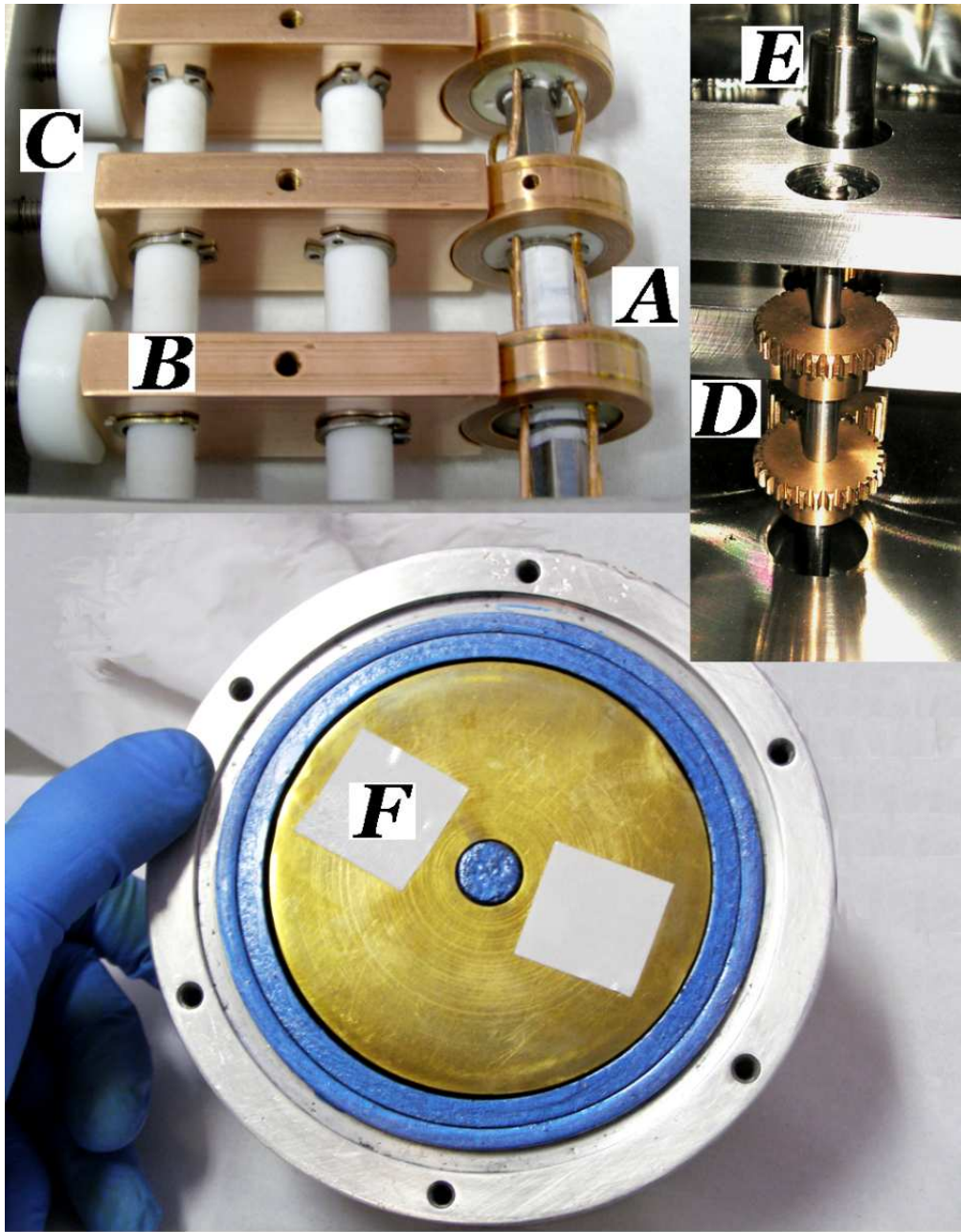


Figure 2.4. Top left: dynamic electrical contacts composed by copper discs connected with the sample shaft (A), insulated by means of macor<sup>TM</sup> workable ceramic and powered by enameled copper wires; copper counter-blocks suspended by two polytetrafluoroethylene bars (B); insulated compression screws to improve electrical contact (C). Right: gearbox with bronze multiple coupling mechanism (D) and coaxial sample operation shaft (E). Bottom: aluminum magnetron cathode with brass cooling plate (F), visible the blue anticorrosion enamel and white polymeric thermally conductive stickers.

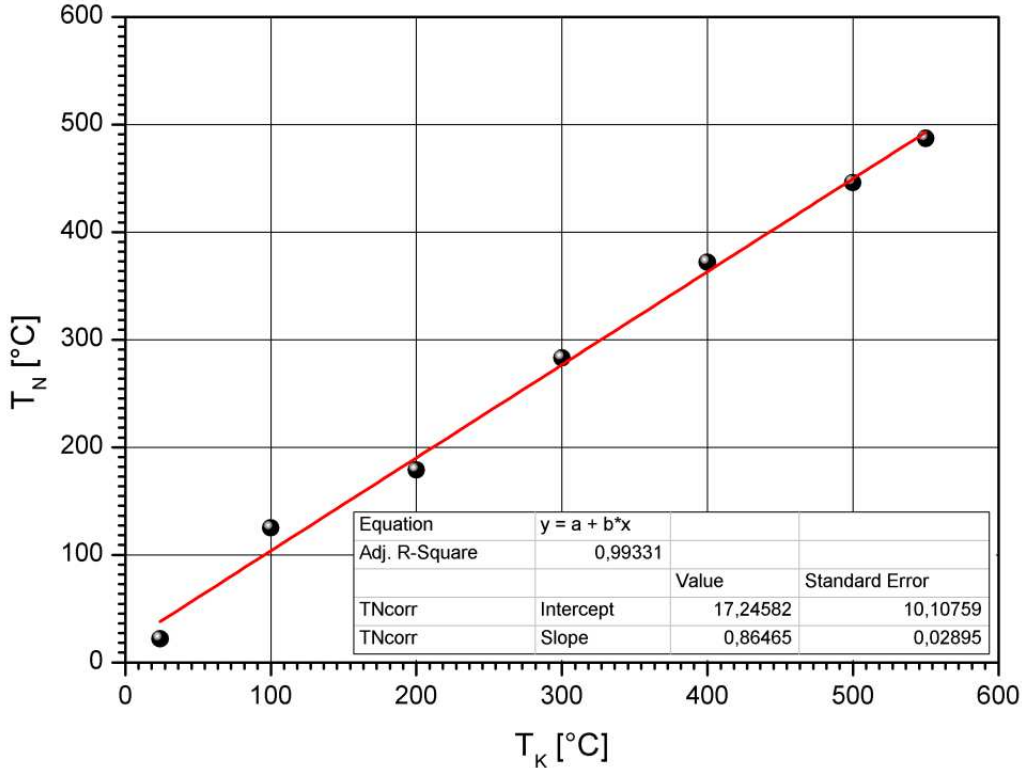


Figure 2.5. Oven set temperature versus sample effective temperature, experimental readings (black dots) and linear fit (red line). Indications are in  $^{\circ} C$ .

## 2.4.2 Dynamic electrical contacts

Inside the vacuum chamber, a dynamic electrical contact was realized to allow complete and multiple rotation of the sample holder shaft (see figure 3.12 A, B, C and figure 2.6 B); four different contacts allowed the correct power supply to the oven (two high-voltage AC channels) and its control via the thermocouple (two low-current analogue channels). The dynamic electrical contact consists in the mechanical coupling of a copper rotating disc (rotor), insulated from the chamber potential, coupled with a copper concave block (stator), connected to the feedthrough. The four stators are mounted on flexible polytetrafluoroethylene (PTFE) bars; the pressure exerted on the rotors is adjusted by the appropriate registration of four screws / springs, exerting a force on the stators. Used copper was electrochemically refined, oxygen free (OFC) grade , optimal choice for vacuum

applications; every surface has been manually mirror-polished. This original dynamic

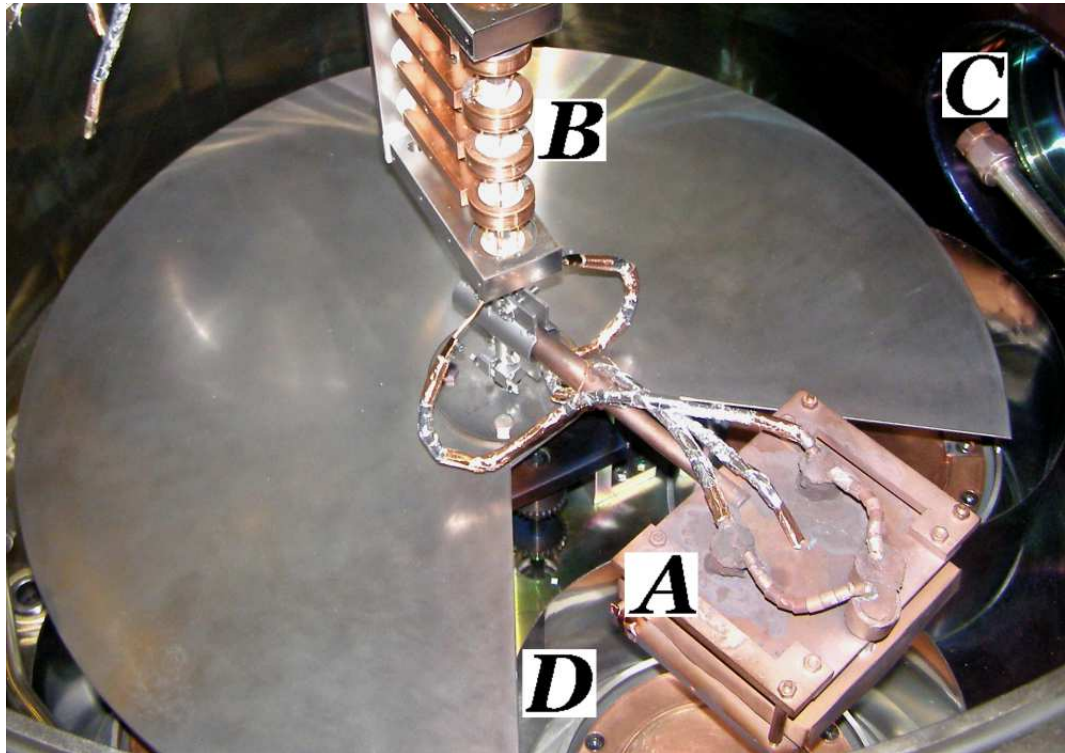


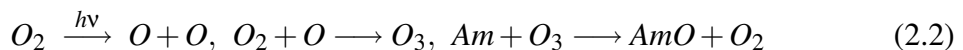
Figure 2.6. View of the inner part of main vessel; tantalum oven support head and arm (A) are suspended above cathodic sources, with their copper target holders and steel electrical shields (D); notice the alumina insulating beads and the aluminum RF shield positioned on both power and signal connections above the oven. Dynamic electrical contacts are mechanically coupled to sample shaft (B) and suspended by a side arm in the middle of the vessel; the Ar distribution tubing is visible close to the sample transfer flange connecting the load-lock (C). In this position, the shutter is ready for the deposition from the cathode facing the oven.

electrical contact design represented an innovative and cost effective solution to the problem of a full rotation around the inner shaft.

## 2.5 Load-lock chamber

Load-lock chamber helps in inserting and recovering samples without the breaking of vacuum. It is basically a stainless steel cylinder with an electrical feedthrough for the operation of thermocouples and/or Peltier cells, with a dedicated gas inlet port, a dedicated pressure detection port, a sapphire window for deep ultraviolet (DUV) light injection and a rapid port with DUV fused silica window for light detection. After the sample has been introduced using the rapid port, one has to make a primary vacuum in the load-lock and to increase pressure with an inert gas flow in the main vessel. After pressure equalisation below a differential pressure of 40 mTorr for the safety of the gate valve mechanism, having care to maintain a higher pressure in the main vessel in order to direct the gas flow towards the load-lock and avoid eventual contamination with oil microdroplets, the gate valve may be opened and the sample can be transferred. This operation requires careful alignment of the transfer beam screw with the sample holder fitting, achievable thanks to the tilting flange and to a mirror and powerful LED lamp installed on top of the beam, which allow the operator to accomplish positioning/recovering using the rapid port window.

The load-lock chamber is equipped to perform two different processes: the reactive UV-assisted oxidation of metallic samples and the magnetic field cooling treatment. A DUV deuterium lamp Hamamatsu L2D2 is installed in correspondence with the sapphire window, flanged 40CF; the emitted wavelength is localised in the interval from 185 to 400 nm. The lamp is operated by a proprietary electronic starter and allows ozone production in an oxygen-rich atmosphere (equation 2.2). The ozone acts as a strong oxidant specie and is used to convert alkaline metals (*Am*) into their respective oxides, based on the chemical reaction [58]:



A field cooling treatment consists in the recovery of a hot FM or AFM sample from the main vessel and in the positioning of the same in the gap of two soft iron electromagnet poles. A *DC* high power generator provides the necessary current to generate a stable magnetic field, uniform in the gap; maximum operative field is close to 700 Oe with an

injected current of 5 A, the field gap being 25 mm wide. This corresponds to a  $138.7 \pm 0.5$  Oe/A yield, as it is possible to see from the linear fit of figure 2.8; currents higher than 5 A are not recommended since in vacuum the thermal conductivity is poor and it is not possible to extract heat generated by the Joule heating of the coils. The field induces a magnetocrystalline anisotropy in the samples, which are let cool down slowly in vacuum, since the principal heat transmission mechanism, irradiation, is not effective at temperatures below 400° C inside a chamber with mirror-polished walls.

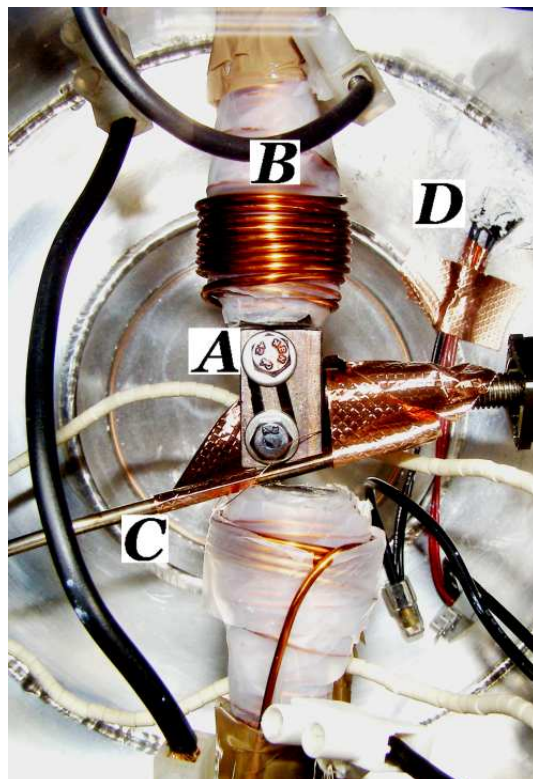


Figure 2.7. View of the inner part of the load-lock chamber. A sample has been retracted from the main vessel, held between screws (A) and subjected to a uniform magnetic field between the two poles of an electromagnet (B); a N type thermocouple acquires sample temperature (C). A Peltier cooling system is available for other experiments (D).

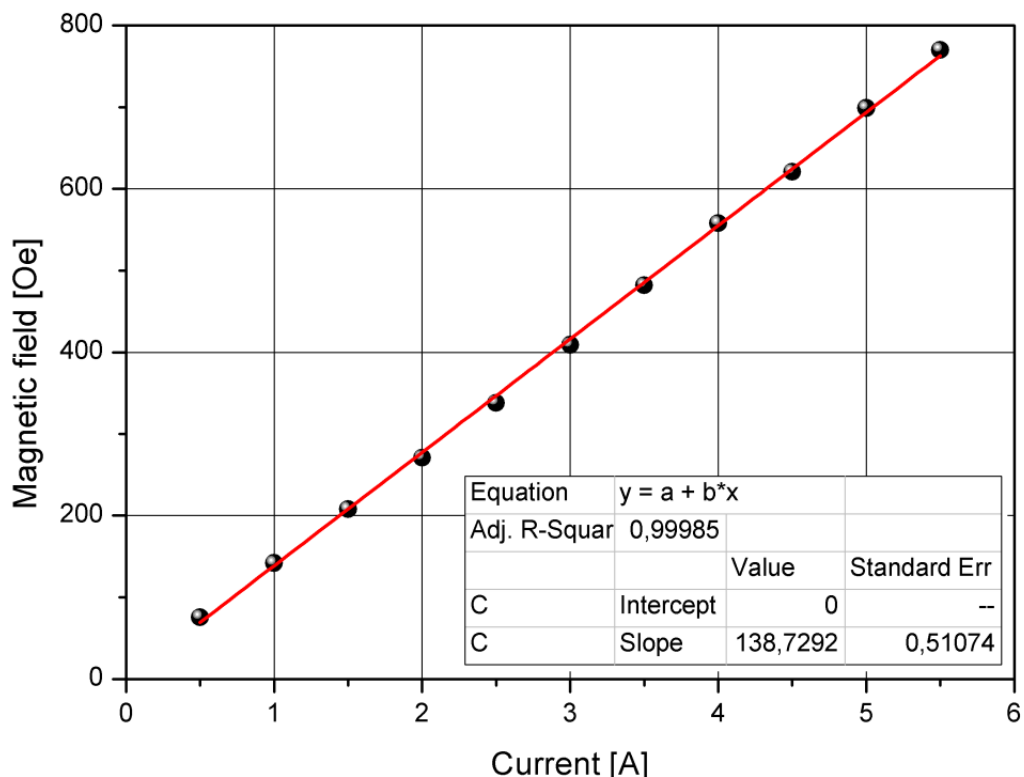


Figure 2.8. Experimental determination of the electromagnet setup yield: black dots experimental data, determined by a solid state Gaussmeter mounted in the middle of the gap between poles (see figure 2.7); red line, linear fit to data, with imposed a zero intercept. Found yield was  $138.7 \pm 0.5$  Oe/A.



# Chapter 3

## Device Engineering

### 3.1 TMR in MgO-based MTJs

Since the first works published relative to MgO-based MTJs, in 1997 [42], a great effort has been done by the international research community to develop extremely high TMR rates and also tune the absolute resistance value to the specific application. For example both MRAMs and HD read heads require an impedance matching, since high speed operation of an electronic circuit has to face with its impedance. HD read head sensor recommended values for the resistance per area ( $RA$ ) are below  $1 \Omega \cdot \mu\text{m}$ , with a  $\text{TMR} > 50\%$  to record data on a media with a density<sup>1</sup> of  $500 \text{ Gbit / in}^2$  [17]. An MRAM requires a higher RA product, in the range from 10 to  $1 \text{ k}\Omega \cdot \mu\text{m}$ , depending on the cell size. TMR effects as high as 200% are now addressed to as GTMR, as indicated at page 17. Theoretical work on monocrystalline epitaxial Fe/MgO/Fe (see figure 3.1) and Co/MgO/Co [59] MTJs was galvanising research towards these challenging systems: full epitaxial structures were reproducible only with MBE and the interface quality was not so good because of local oxidation of the FM electrodes [60]. Anyway important results have been obtained: one such example is room temperature 400% GTMR on Co/MgO/Co fully epitaxial systems with metastable bcc Co(001) electrodes [61]. A further development of the technique has evidenced the importance of texture: sputtering may be used to

---

<sup>1</sup>for comparison, commercial HDs feature a recording density around  $100 \text{ Gbit / in}^2$ .

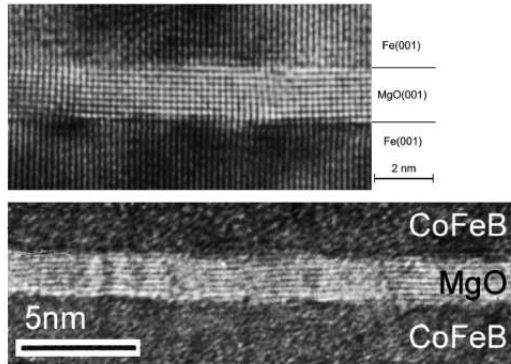


Figure 3.1. TEM images of the junction area: above, a fully epitaxial monocrystalline junction Fe/MgO/Fe, after [61]; below, a texturised polycrystalline junction CoFeB/MgO/CoFeB, after [63].

realise GTMR-ready highly oriented polycrystalline tunnel junctions if a seed layer transfers its texture to the growing system. It consists mainly of oriented grains and marginally of amorphous grain boundary regions and has been called textured MTJ [62]. The importance of texturing has been studied in detail, since GTMR has been observed also for systems which were believed to be amorphous, such as CoFeB/MgO/CoFeB MTJs, shown in the TEM micrograph of figure 3.1. An *in situ* [63] or *ex situ* [64] annealing at 360° C restores the crystallographic order of close-to-interface FM atomic layers, by so called solid phase epitaxy; the scheme of figure 3.2 is helpful for comprehension. Also a detrimental solid phase epitaxy has been individuated [65], observing that certain cap layers promote the recrystallisation of the top FM electrode, sometimes with a orientation different with respect to the tunnel barrier one, thus suppressing coherent tunneling.

The first simple system proposed in this thesis is a polycrystalline MTJ deposited on naturally oxidised silicon(100), with a structure Si/SiO<sub>2</sub>/Co/MgO/Co/Cr. One expects the native oxide to be amorphous, while Co appears to be in the fcc form without any preferential anisotropy. The outer Cr layer acts as an AFM pinning layer and is obtained *ex situ* by thermal evaporation.

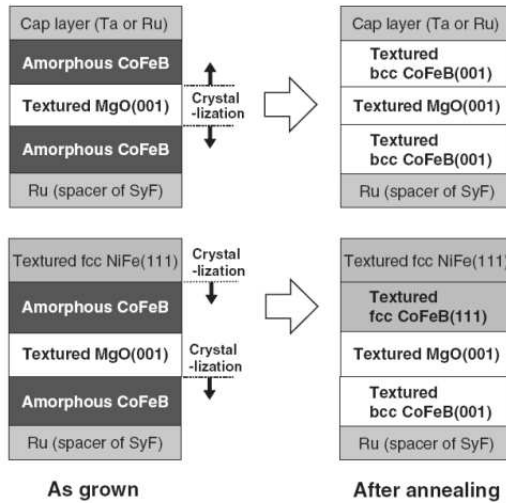


Figure 3.2. Scheme showing the solid phase epitaxy effect on MTJ: above the positive crystallisation effect induced by MgO on CoFeB; below the negative crystallisation effect induced by NiFe on CoFeB; adapted from [17].

## 3.2 Single films and rate determination

During the deposition process four parametres may be varied, each one having a particular influence on the deposit characteristics:

- (1) the partial Ar pressure is varied by combined effect of MFC and throttle valve in the stable plasma range, from 0.1 to 100 mTorr ; an intermediate pressure range, around 10 mTorr, has been individuated as the optimal deposition condition for every material considered in this thesis, since both above and below this value the homogeneity of the deposit is not adequate;
- (2) the RF signal power is varied in the stable plasma range, from 25 to 300 W; magnesium has shown plasma instability and strong metal ionisation above 200 W; generally the optimal power range is below 100 W, since above the homogeneity of the deposit is not adequate and ionic implantation is possible, unless a cap layer has to be realised with high throughput and low homogeneity requirements;
- (3) the substrate temperature may be varied in the stability range of the substrates, from

10 to 500°C; above the upper bound, silicides may be formed by diffusion of Si towards the metallic layers; the formation of oxides via oxygen diffusion from the native/thermal oxide is possible above 350° C; the effect of temperature is a general dewetting of the substrate and the gradual formation of islands from an interconnected percolative structure up to a completely uniform structure of elliptical drops (see page 48); the optimal substrate temperature is room temperature;

- (4) the deposition time may be varied, which is linear with respect to the deposit thickness; growth mode is not influenced by the deposition time, but for extremely thin layers one obtains that the *ex situ* thickness determination via atomic force microscopy (AFM) shows a nonlinear *incipit* corresponding to nucleation followed by a regular linear behaviour corresponding to the growth of complete monolayers (ML).

In the following subsections single film properties will be analysed. In particular the deposition rate is fundamental for subsequent processes. Rate is extrapolated from the thickness versus deposition time plot, as the slope of a linear fit with null intercept. The thickness of a sample is determined using an AFM equipment and acquiring a wide area over a step (usually  $50 \times 50 \mu\text{m}^2$ ), artificially produced by a lithographic process; multiple row averaging is then accomplished and a mean thickness value is obtained.

### 3.2.1 Cobalt

Co in the form of fcc thin films has been prepared in the following conditions: Ar partial pressure 10 mTorr, RF power 75 W, substrates at room temperature. The deposition rate has been estimated to be  $12.6 \pm 0.3 \text{ pm/s}$ , as it's possible to deduce from the slope of the linear fit adapted to experimental thickness determinations in figure 3.3. The Co deposition rate, confronted to the rate of other metals, is ten times smaller, since the magnetic field flux lines generated by the magnetron are shunted by the thick target and their enhancing effect is nearly killed. As it may be seen from the field effect scanning electron microscopy (FESEM) map of figure 3.15 (A), the morphological homogeneity of the sample is rather high. The magnetic properties of so produced single layer films have been investigated by different techniques: alternating gradient force magnetometry

(AGFM) and magnetic force microscopy (MFM), which have been used to evaluate the coercivity dependence upon film thickness (see figure 3.4) and the surface magnetic configuration of domains in as grown samples (see figure 3.5), respectively. The coercivity has been extrapolated from experimental measurements using a numerical tool, written in the Matlab ® environment; for details see page 70. As ideal Co hard/soft electrodes for MTJs, films with a thickness of 5 and 20 nm respectively have been chosen, having an in plane coercivity of 230 and 50 Oe respectively.

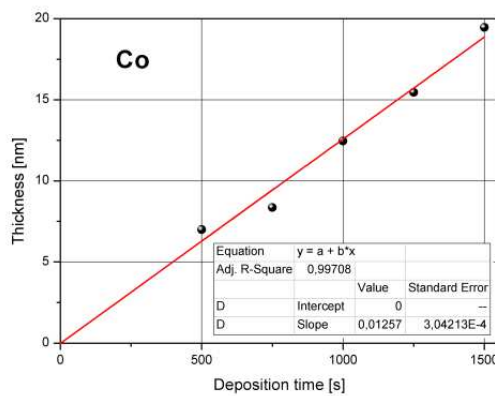


Figure 3.3. Estimate of Co deposition rate from a linear fit with zero intercept of thickness data.

AFM and MFM images are used to evaluate the magnetic anisotropy of the film; since the magnetic data matrix appears to be uncorrelated from the topographic dataset, useful extrapolations about magnetic roughness versus the film thickness may be extracted from the grain analysis computed on the MFM. Figures 3.5, 3.6, 3.7 and 3.8 represent the acquired data. It is possible to see that the perpendicular anisotropy decreases with increasing film thickness, as the sharp small grains (figure 3.5), where magnetisation is more likely to point out of the film plane, evolve into broader and smoother structures (figure 3.8), where in plane magnetisation varies smoothly from one region to the other of the sample.

The parametres elaborated for each grain individuated by the thresholding algorithm are the following (for details, see page 81):

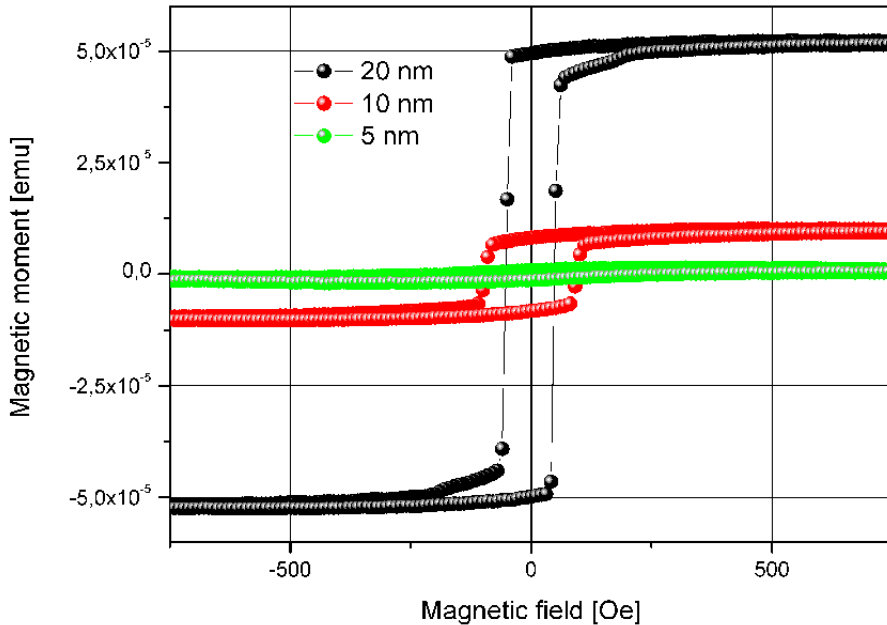


Figure 3.4. *Hysteresis loops acquired at room temperature with a magnetic field applied in the plane of the film, up to 18kOe (the present figure shows a magnified portion close to origin), on 5, 10 and 20 nm thick Co films.*

- (1) equivalent diametre (*ED*), computed as the diametre corresponding to a circle having the same area of the grain under analysis;
- (2) relative orientation (*RO*), computed as the angle between the horizontal axis and the major axis of the ellipse that has the same second moment as the grain under analysis;
- (3) equivalent eccentricity (*EE*), computed as the ratio between the distance between the foci and the major axis length of the ellipse that has the same second moment as the grain under analysis;
- (4) branching factor (*BF*), computed as the ratio between the area of the ellipse and the area of the grain.

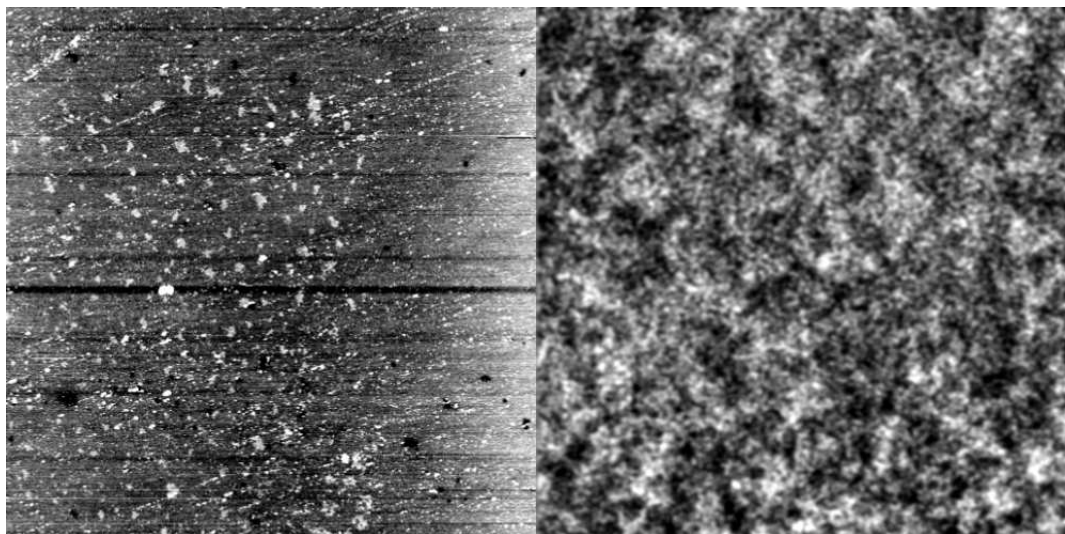


Figure 3.5. AFM (left) and MFM (right) data matrices relative to an area of  $10 \times 10 \mu\text{m}^2$ , acquired on a Co sample obtained with a deposition time of 500s, corresponding to a nominal thickness of 6.3 nm. Lift scan height was 80 nm.

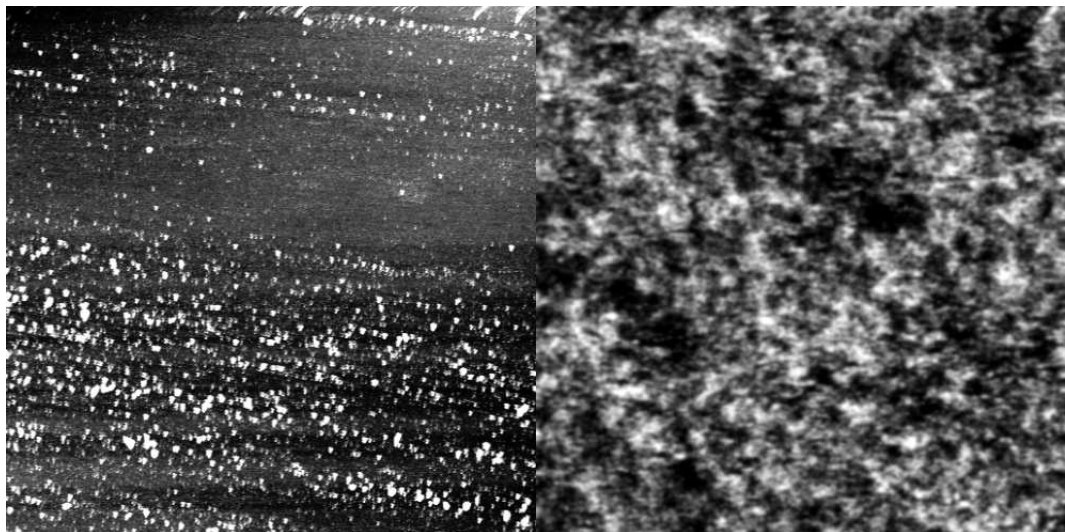


Figure 3.6. AFM (left) and MFM (right) data matrices relative to an area of  $10 \times 10 \mu\text{m}^2$ , acquired on a Co sample obtained with a deposition time of 750s, corresponding to a nominal thickness of 9.45 nm. Lift scan height was 80 nm.

Successively, statistics are summarised by the median value of each distribution and

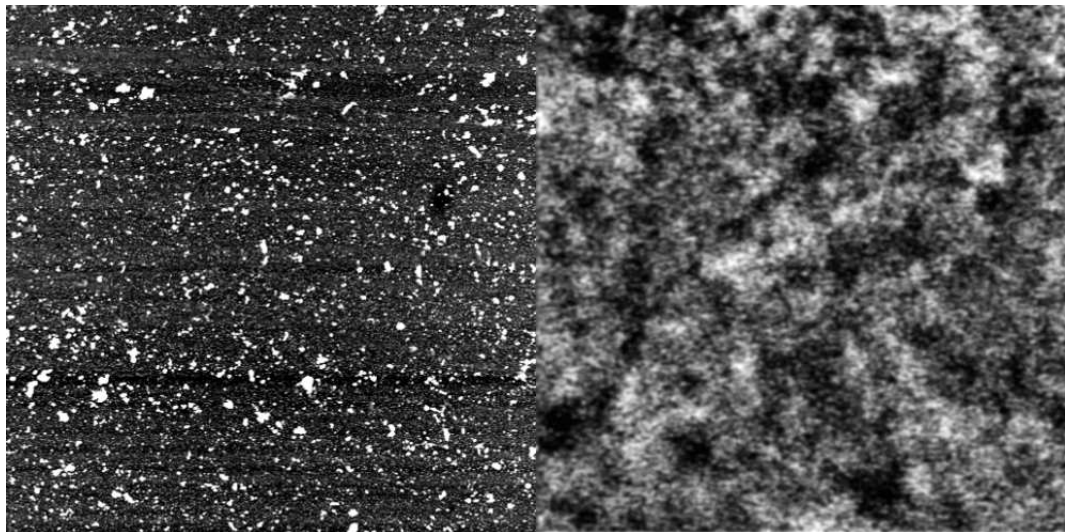


Figure 3.7. AFM (left) and MFM (right) data matrices relative to an area of  $10 \times 10 \mu\text{m}^2$ , acquired on a Co sample obtained with a deposition time of 1000s, corresponding to a nominal thickness of 12.6 nm. Lift scan height was 80 nm.

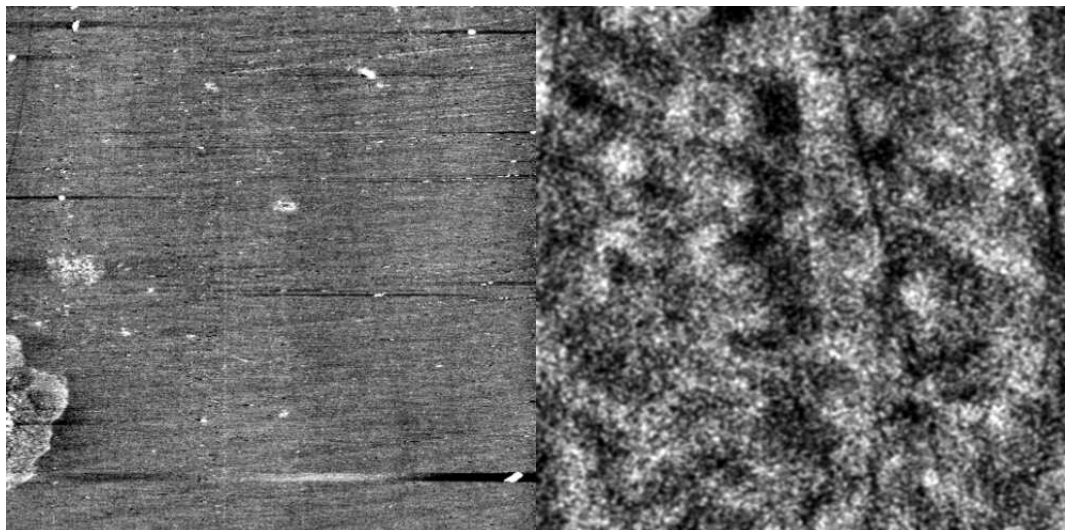


Figure 3.8. AFM (left) and MFM (right) data matrices relative to an area of  $10 \times 10 \mu\text{m}^2$ , acquired on a Co sample obtained with a deposition time of 1500s, corresponding to a nominal thickness of 18.9 nm. Lift scan height was 80 nm.

its standard deviation; in particular, since the branching factor distribution contains interesting information besides from the sharpest peak positioned at zero branching ( $BF = 1$ ),

the corresponding median has been computed considering non-unity population. Both the median equivalent diametre evolution and the percentage of branched grains on the total amount of grains show a peculiar trend, as represented in figure 3.9. Furthermore, the *RO* distribution is symmetric with respect to zero degrees and the *EE* has been found to be  $0.8 \pm 0.2$  for every sample (data not shown).

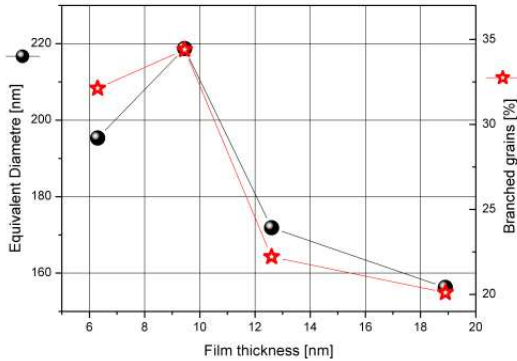


Figure 3.9. Extrapolations relative to the magnetic roughness of MFM matrices of figures 3.5, 3.6, 3.7 and 3.8: median equivalent diametre (black dots) and percentage of branched grains (red stars) as a function of nominal thickness.

## Temperature and pressure effect

The combined effect of higher Ar pressures and higher substrate temperatures has been also investigated. Portions of FESEM maps of Co films grown with a substrate temperature of  $300^\circ\text{C}$  at different partial Ar pressures are shown in the area of the graph in figure 3.10. The island like structure, developed after a dewetting from the substrate, does not allow to use this material for device fabrication. A detailed grain analysis has been done using a numerical tool, written in the Matlab ® environment; for details see page 81. Thanks to this tool it has been possible to extract grain structure characteristics; in particular a correlation between the equivalent diametre and the eccentricity has been found.

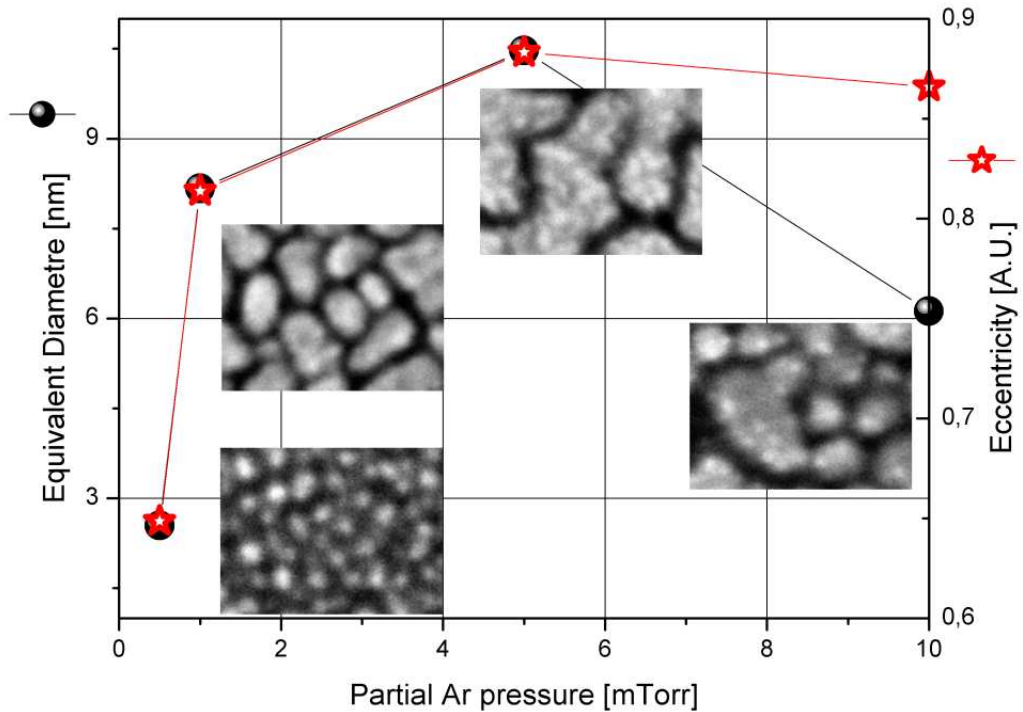


Figure 3.10. *Extrapolations relative to the median equivalent diametre and eccentricity, as a function of partial Ar pressure during deposition. Inside the graph area the corresponding portions of very high resolution FESEM maps are reported, showing an area of  $55 \times 40 \text{ nm}^2$ .*

### 3.2.2 Magnesium

Mg in the form of fcc thin films has been prepared in the following conditions: Ar partial pressure 10 mTorr, RF power 60 W, substrates at room temperature. The deposition rate has been estimated to be  $135 \pm 8 \text{ pm/s}$ , as it is possible to deduce from the slope of the linear fit adapted to experimental thickness determinations in figure 3.11. This rate is ten times higher than the rate of Co, due to the soft nature of Mg and the low energy required for the deposition; no magnetron has been used, to reduce the rate and gain a better control on the deposition itself. The FESEM map of figure 3.15 (B) confirms the morphological homogeneity of the samples before oxidation. A DUV deuterium lamp has been used to oxidize in a ozone-saturated atmosphere the samples (see page 35), at a pressure of 100 Torr. After the oxidation, the sample surface appears very different from

the grained metal structure, as shown in figure 3.12 (A), where big polyhedric grains with flat surfaces appear, as big as a hundred nm.

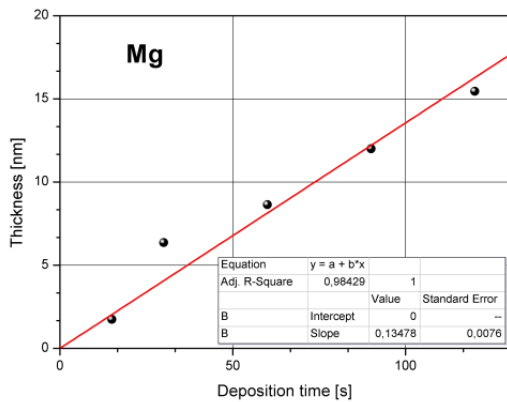


Figure 3.11. Estimate of Mg deposition rate from a linear fit with zero intercept of thickness data.

### 3.2.3 Cromium

Cr in the form of fcc thin films has been prepared in the following conditions: Ar partial pressure 10 mTorr, RF power 100 W, substrates at room temperature. The deposition rate has been estimated to be  $130 \pm 5$  pm/s, as it's possible to deduce from the slope of the linear fit adapted to experimental thickness determinations in figure 3.13. This rate is comparable to the one of Mg, but one may consider that the deposition is magnetron-assisted (and this increases both yield and rate) and that Cr is a hard metal; the two effects are balanced and the deposition rate is perfectly in line with the one of Mg. As it may be seen from FESEM map of figure 3.15 (C), the morphology of the samples is very peculiar and cross-shaped geminates appear. A full characterisation of Cr morphologies as a function of deposition time is shown in figure 3.12; at thicknesses of about 50 nm the sample surface is composed by a patchwork of rounded grains (B), while as soon as the thickness is increased, cross-shaped geminates appear and grow in size (C, D and E), until bigger and flat textured surfaces are presented (F).

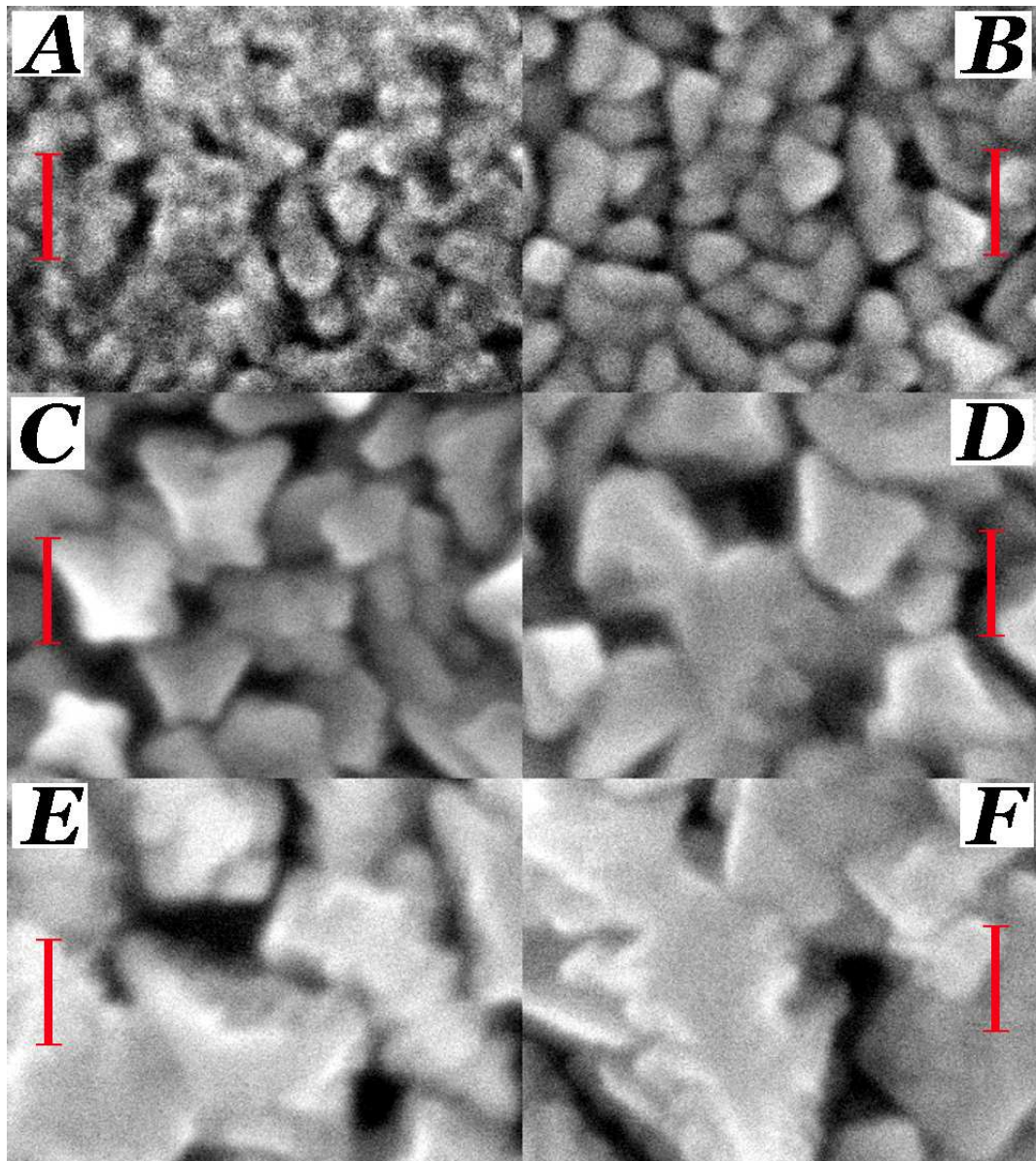


Figure 3.12. Morphologies explored by FESEM. A: surface of 16.2 nm thick Mg sample (Ar partial pressure 15 mTorr, RF power 20 W, substrates at room temperature) after ozone UV assisted oxidation; the red bar corresponds to 100 nm (500 k $\times$ ); B: extremely high resolution image representing the surface of a 52 nm thick Cr sample (Ar partial pressure 10 mTorr, RF power 100 W, substrates at room temperature); the red bar corresponds to 50 nm (1M $\times$ ); C: as in B, sample nominal thickness 97.5 nm; D: as in B, sample nominal thickness 130 nm; E: as in B, sample nominal thickness 195 nm; F: as in B, sample nominal thickness 260 nm.

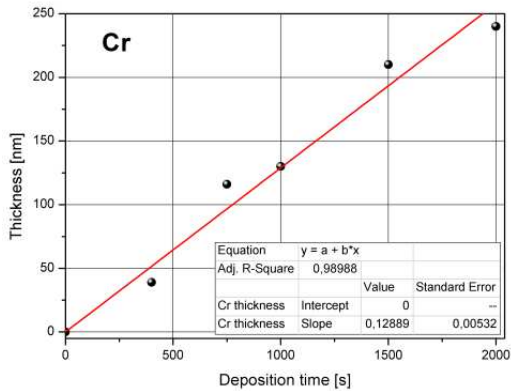


Figure 3.13. Estimate of Cr deposition rate from a linear fit with zero intercept of thickness data.

### 3.3 MTJ: process and characterisation

A full description of the process steps completed to realise the MTJ is reported here, for reference see figure 3.14:

- (1) cleaning of a p:Si(100) substrate with acetone and ethanol, in an ultrasonic bath at room temperature;
- (2) 30 nm bottom copper electrode deposition, via thermal evaporation and shadow masking; the masks were obtained by LASER microablation on a stainless steel thin foil, in collaboration with Microla Optoelectronics S.r.l.;
- (3) junction area definition via positive resist;
- (4) 20 nm Co soft electrode deposition via RF magnetron sputtering (10 mTorr, 50 W, 900 s);
- (5) 1.5 nm Mg tunnel barrier precursor deposition via RF sputtering (10 mTorr, 20 W, 15 s);
- (6) oxidation of the precursor to MgO in 100 Torr ozone atmosphere obtained by UV irradiation of pure O<sub>2</sub>, for 30 min;

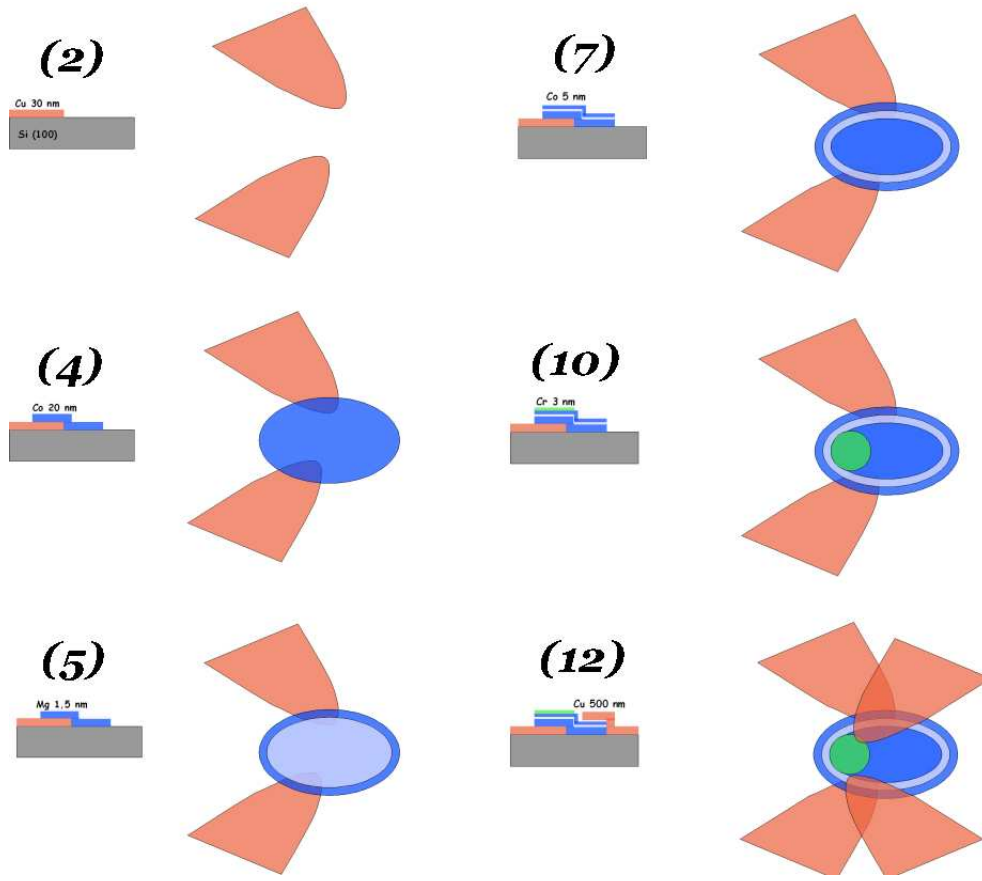


Figure 3.14. Sketch of the process adopted to realise the first prototype of MTJ. From top to bottom, left column: Cu 30 nm bottom electrodes, Co 20 nm soft layer, Mg 1.5 nm tunnel barrier precursor; right column: Co 5 nm hard layer, Cr 3 nm pinning layer, Cu 500 nm top electrodes.

- (7) 5 nm Co hard electrode deposition via RF magnetron sputtering (10 mTorr, 50 W, 150 s);
- (8) lift-off;
- (9) junction texturisation thermal annealing in inert gas atmosphere (Ar 1 mTorr): heating from room temperature to 300° C in 2 h, then to 350° C in 15 min, permanence of 15 min, cooling to room temperature in 30 min with a nitrogen overpressure of 1330 Torr to force heat transfer;

- (10) 3 nm Cr AFM pinning layer deposition, via thermal evaporation (*ex situ*) and shadow masking; the masks were handmade on a copper thin foil;
- (11) junction ridge isolation with a polymeric mask;
- (12) 500 nm Cu thick cap electrodes deposition, via thermal evaporation and shadow masking; the masks were obtained by LASER microablation on a stainless steel thin foil, in collaboration with Microla Optoelectronics S.r.l.;
- (13) 500 nm Cu thick pads for bottom electrodes deposition, via RF magnetron sputtering.

For what concerns step (6), the UV assisted ozone treatment has been widely studied, for example in [67]; in [68] the optimal process parametres have been individuated: the higher TMRs are achieved with a pressure-by-time product comprised between  $10^4$  and  $10^6$  Langmuir ( $1L = 1e-6 \text{ Torr} \cdot \text{s}$ ), our case being positioned around the lower limit. Furthermore the oxidation process consists of two phases, the first one dominated by immediate reaction with oxygen and the other one dominated by the slow diffusion of oxygen across the film. The annealing discussed in step (9) has been shown to result in structural changes [66], taking place already in the first minutes: the lattice constant of MgO changes and recrystallisation occurs.

### 3.3.1 Morphological characterisation

The optical figure 3.16 shows the aspect of the first MTJ which has been realised. The total junction area is  $1.57 \text{ mm}^2$ . The two bottom electrodes are on the left. The FESEM map of figure 3.15 (D) confirms that grains are pretty homogeneous; median grain size is 8.6 nm, the distribution is heavily scaled because of aggregation of very close clusters; the fraction of branched grains is 43.7% and the median branching factor is  $0.94 \pm 0.02$ , very close to unity.

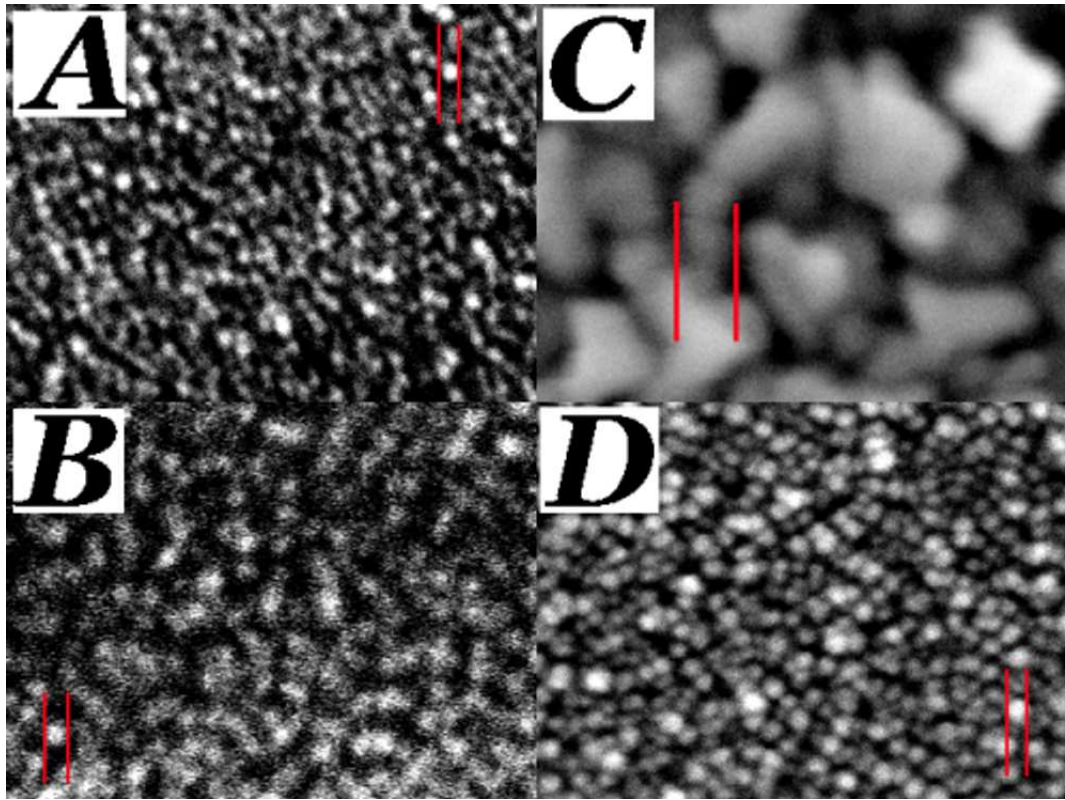


Figure 3.15. Very high resolution FESEM maps showing the top grain structure: A) 13.6 nm Co single layer on Si(100), resolution of 1.2 nm/px, grain within red bars 9 nm; B) 33.75 nm nominal thickness Mg single layer on Si(100), resolution of 1.5 nm/pixel, grain within red bars 10 nm.; C) 65 nm Cr single layer on Si(100), resolution of 0.36 nm/px, grain within red bars 10 nm; D) MTJ top (corresponding to Cr), resolution 1.5 nm/px, grain within red bars 10 nm..

### 3.3.2 Electrical measurements

TMR and R versus T measurements have been done from room temperature down to 30 K in a liquid helium cryostat, with a magnetic field up to 70 kOe applied parallel to the device/substrate plane and a constant current of 10  $\mu$ A; the voltage drop has been monitored after allowing the thermalisation of the biased sample and resistance has been computed. In a typical measure, the field is raised up to positive (negative) saturation and then is slowly decreased (increased) until the opposite saturation is reached. The second branch is acquired in a similar manner. Usually resistance for millimetre-sized

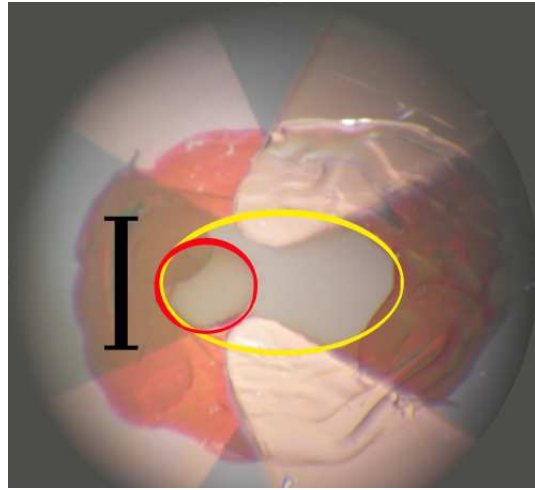


Figure 3.16. Optical image of the first MTJ prototype. The red circle encloses the Cr AFM pinning layer, while the yellow ellipses represents the contour of the junction. The black bar is 1 mm in length.

MTJs is in the order of the tenth of k $\Omega$ s. External leads have been soldered using an In-Sn alloy which provides the adequate wettability to evaporated/sputtered Cu. The curve proposed in figure 3.17 has been subtracted from normal quadratic magnetoresistance and normalised with respect to the zero value:

$$TMR = \frac{R(H) - R(H = 0)}{R(H = 0)} \cdot 100 \quad (3.1)$$

A TMR of 0.1% has been found at 100 K; above and below this temperature level some problems are encountered. Below 100 K the junction resistance becomes so high that the substrate starts to drain a significant amount of injected carriers, and the p:Si magnetoresistive response is found to dominate the signal; above the thermal noise covers the signal.

The R versus T curve shows a linear trend down to 40 K, temperature where the resistance starts to grow exponentially; when it becomes comparable to the input resistance of the volt metre, no further reading is significant. This behaviour has been also documented in literature, for example in [69]. A linear fit to the curve gives a resistance increment of 70  $\Omega$  / K with reducing temperature. No magnetic effect is observed in room temperature IV characteristics, acquired by imposing a voltage drop across the device and measuring the current that flows through the device, while a coil provides the magnetic field, up to

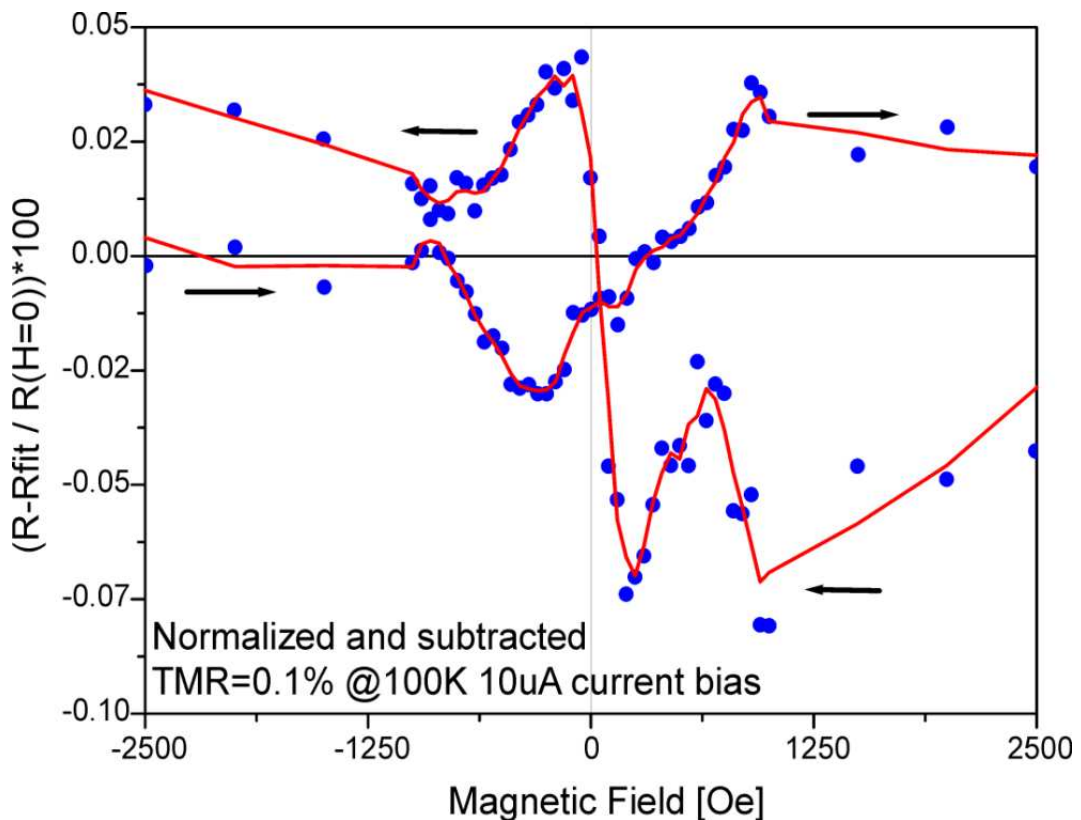


Figure 3.17. Subtracted and normalised TMR curve, recorded at 100 K, with an injected current of  $10 \mu \text{A}$ .

150 Oe, applied in the device plane. The bias voltage should be kept low, to avoid voltage-induced reduction of TMR; as it is possible to see, the two linear fits to asymmetric tails of the curve give two different threshold voltages for the device, -3.6 and 7.2 V respectively. Measures performed on the substrate by itself, let us deduce that silicon contributes to the conduction of 1% of total current density, at room temperature.

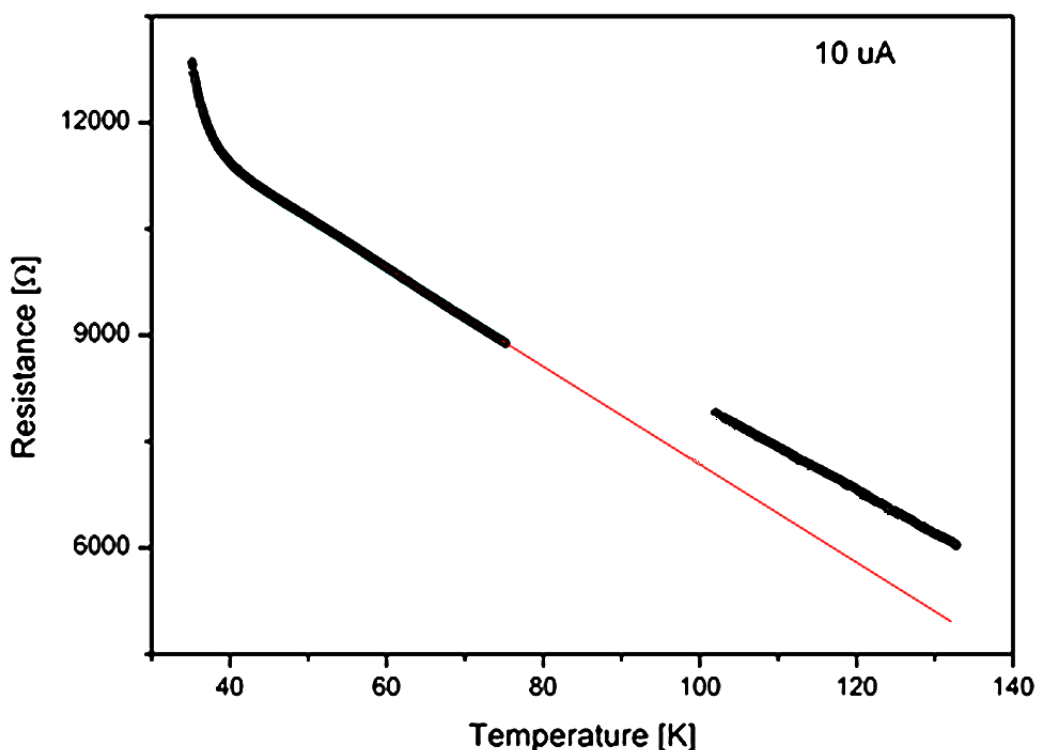


Figure 3.18.  $R$  vs  $T$  curve in the range from 30 up to 100 K.

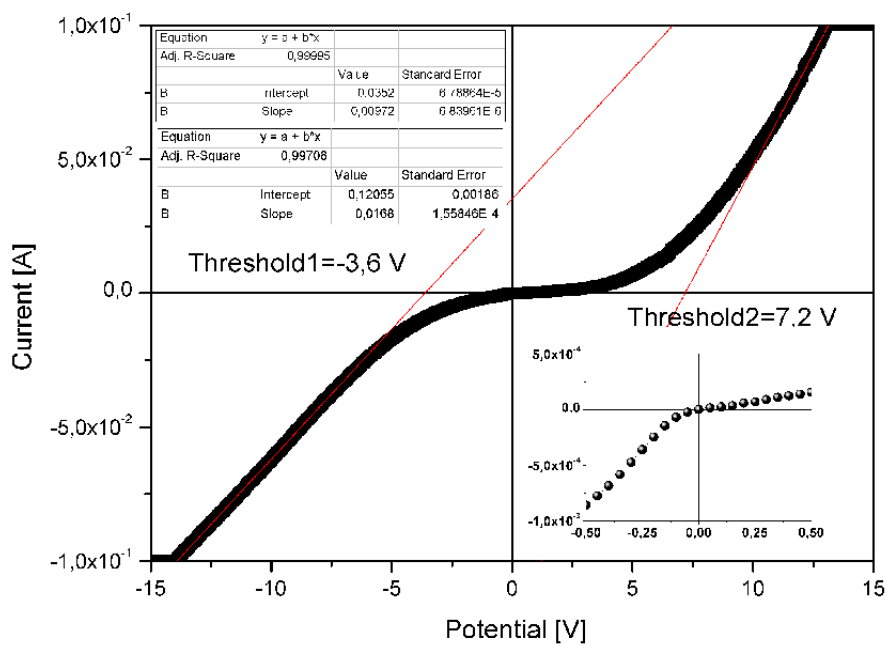


Figure 3.19. IV measurements taken at room temperature. The inset shows the low voltage part of the measure, while red lines are linear fit used to evaluate the threshold voltage for conduction both at forward and at inverse polarisation. Notice that the experimental setup clamped the system at a maximum current of 100 mA.

## 3.4 Real-time measurements

The determination of sample thickness via AFM is particularly difficult in the case of Mg or MgO, since the thin film tends to adsorb solvents used during the lift-off step. After the adsorption some detachments from the substrate may happen and the height reading is heavily biased. This difficulty brought us to conceive a particular experiment to measure directly during the deposition the sample height, without leaning on resonant quartz crystals that dramatically interfere with RF. The solution has been found in a dedicated sample for real-time resistance measurements, composed by a square thermally oxidised Si of  $1 \text{ cm}^2$  area, with two (four) thermally evaporated thin Cu films to realise a two (four)-points-probe-ready sample.

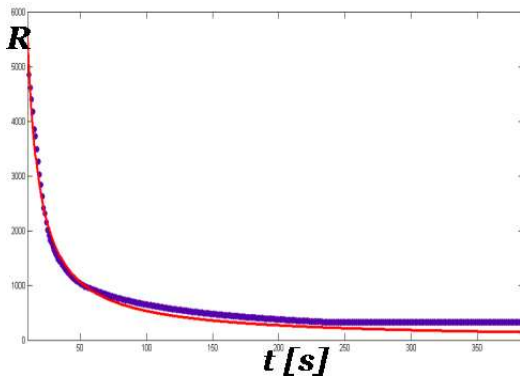


Figure 3.20. *Real-time measure of electrical resistance across an open circuit, during the deposition of a thin Mg layer (blue dots: experimental data); fit with the Fuchs-Sondheimer thin film conduction model (red line).*

A sketch of the measure setup is presented in figure 3.21 (A), where the growing Mg film is indicated by arrows and by the transparent-hatched region. Initially the open circuit has a rather high resistance across the 1 mm gap, but as soon as metal deposition starts, a steep decrease in resistance is found, sampling the so called Fuchs-Sondheimer conduction regime, which is simplified by the following model:

$$\frac{\rho}{\rho_b} = \left(1 + \frac{3\lambda}{8h}\right) \quad (3.2)$$

where  $\rho$  is the thin film resistivity,  $\rho_b$  is the bulk resistivity,  $\lambda$  is the mean free path

in the sample and  $h$  is the film thickness; equation 3.2 is valid when  $h > \lambda$ . Inserting the parametres of the actual experiment, one has:

$$R_{sample} = \frac{\rho_{b,Mg} l_{Mg} (8r_{Mg}t + 3\lambda_{Mg})}{8(r_{Mg}t)^2 w_{Mg}} \quad (3.3)$$

where  $\rho_{b,Mg}=3.8 \cdot 10^{-8} \Omega \cdot m$  from literature,  $l_{Mg}=1 \text{ mm}$  and  $w_{Mg}=10 \text{ mm}$  (geometrical parametres),  $\lambda_{Mg}=1 \cdot 10^{-11} \text{ m}$  (from the fit),  $t$  is the deposition time and  $r_{Mg}=7.3 \cdot 10^{-12} \text{ m}$  (from the fit). This rate is more than one order of magnitude lower than the one predicted from thickness data, but realistic indeed since this particular experiment has been carried on with a polymeric shadow mask to define the rectangular profile of the Mg shunt layer, which may acquire an electric charge during the process and originate a shielding Coulomb blockade. The fit to experimental measurements with equation 3.3, presented in figure 3.20, allowed to extrapolate interesting data.

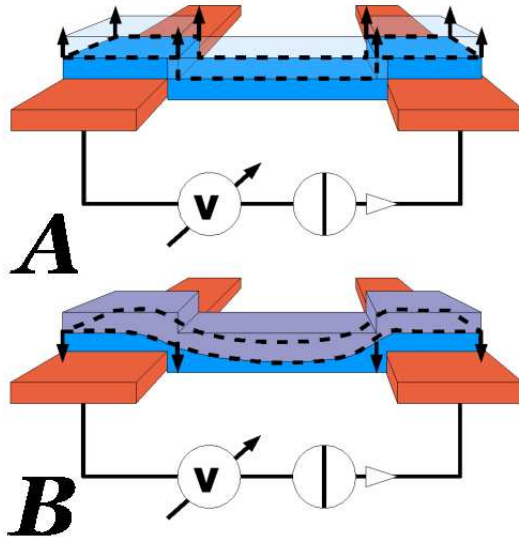


Figure 3.21. Sketch showing the real-time measurement setup. A: during the deposition of a thin Mg shunting layer across two Cu leads; the transparent-hatched region is the active deposition area, where the film is growing, as indicated by the dashed contour. B: during UV assisted oxidation of Mg to MgO; the region in violet is growing at the metal expenses, the moving interface is represented by the dashed lines.

The same experiment has been implemented to monitor the resistance increase during

the oxidation of the same Mg sample to MgO, as sketched in figure 3.21 (B), where the violet portion across leads is the growing oxide and the interface moving downwards has been indicated by a dashed contour and by arrows. This process in particular shows a linear kinetic, as it may be shown by the experimental data of figure 3.22, resulting in a resistance increase of  $0.910 \pm 0.005 \Omega /s$ . The proposed explanation of this linear trend is the following: there are actually two resistive elements whose absolute resistivity is increasing: the first is the growing oxide layer, whose transversal section is becoming wider; the second is the thinned metal layer, whose resistivity is simplified by the same hyperbolic Fuchs-Sondheimer model, with a time reversal. The metal will carry the greatest current density until its resistivity, close to the singularity of its inverted hyperbola, would be comparable to the insulator resistivity. Sampled data, covering a range of 1000 s, are not enough to reach this regime and the linear trend prevails.

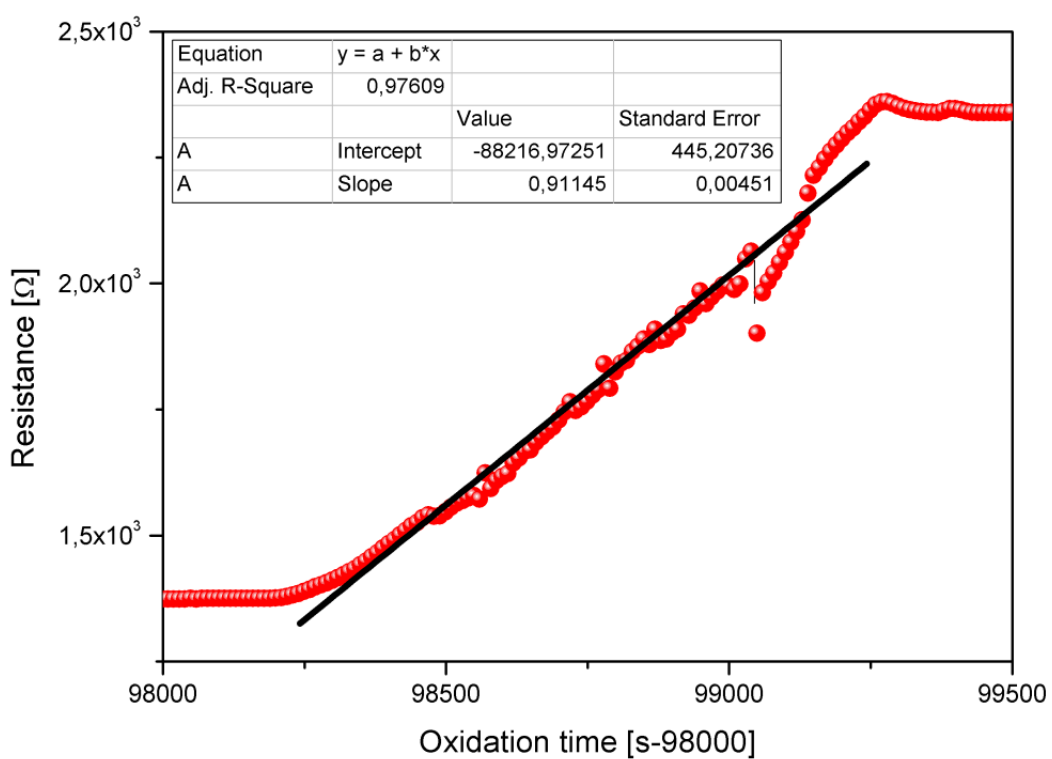


Figure 3.22. Real-time measure of electrical resistance across a Mg thin film, during the ozone UV assisted oxidation treatment.

### 3.5 Problems presented by the first MTJ prototype

The proposed MTJ prototype resulted in a very low TMR; a detailed analysis of the causes evidenced the following points:

- (1) junction leakage through Si substrate is the principal conduction mechanism at very low temperatures, where the highest TMR is expected; this mechanism is not activated at room temperature;
- (2) millimetre-sized FM electrodes have multi-domain structure, produce smooth switching and even result in a switching field distribution, rather than a sharp localised transition; the probability of inhomogeneities and inclusions is greatly increased;
- (3) current is injected at  $45^\circ$  with respect to the normal to the junction, generating Hall-effect contributions to magnetoresistance;
- (4) local electric field enhancements may originate from the sharp edges of the Cu electrodes;
- (5) Co electrodes may be substituted by different materials; a possible choice is CoCr alloy as hard spin injector, allowing a greater difference between coercive fields;
- (6) an AFM pinning layer would reduce the dipolar coupling field that tends to keep aligned the magnetisations in the two electrodes.

In particular, work has been done in the optimisation of both the prototypal deposition apparatus and in the process workflow; these innovations will be presented at page 97. In the following section, preliminary work about CoCr alloys will be presented.

### 3.6 CoCr alloys

Spin-polarized currents across an insulating tunnel barrier, needed for the development of efficient magnetic tunneling junctions (MTJs), may be obtained using hard spin injector electrodes [70] [71]. CoCr alloys have been studied intensively for perpendicular magnetic data storage purposes. Thin films of CoCr solid solutions have been fabricated involving the following steps:

- (1) deposition of Co/Cr alternated layers via thermal evaporation;
- (2) deposition of Co/Cr alternated layers via RF magnetron sputtering;
- (3) diffusion and field cooling treatment, realized in sequence keeping the sample in the high vacuum chamber, and instrumental to the increase of the sample coercivity [72].



Figure 3.23. FESEM image of a tilted cross section of sample C2, positioned perpendicular to the electron beam. A portion of the multilayer has been hatched to show the stack: from bottom to top the system is composed by Si (black), SiO<sub>2</sub> native oxide (yellow), Co (blue) and Cr (green) alternated following the nominal scheme (Co<sub>16</sub>/Cr<sub>5</sub>)<sup>2</sup>Co<sub>18</sub>.

Both silicon (100) substrates and thermally oxidized wafers have been used in order to better characterise the residual anisotropy given by conformal growth on the monocrystalline material or by free growth on the amorphous silica. Thermally evaporated samples have been realised in two different stacks: (Co<sub>5</sub>/Cr<sub>1</sub>)<sup>4</sup>Co<sub>6</sub> and (Co<sub>16</sub>/Cr<sub>5</sub>)<sup>2</sup>Co<sub>18</sub> (see figure 3.23), where the subscript represents the nominal thickness<sup>2</sup> in nm and the superscript the number of repetitions. They will be referred to as C1 and C2, respectively, and C3, C4 for their annealed counterparts. These particular choices of thin film succession/thicknesses respect the particular Co/Cr 80/20 ratio and are aimed to assure a high interdiffusion probability (C1 and C3) and to allow FESEM cross-sectional analysis (C2 and C4). The thermal treatment has been done in a partial Ar pressure of 1 mTorr to help homogenize the temperature with convection (base vacuum 10<sup>-7</sup> Torr); the annealing profile is composed by a first heating step at 80° C, which has the purpose of desorbing water from the sample surface; successively samples have been heated at 450° C for 4 hours (raising speed 6°

<sup>2</sup>thickness is easily determined in the case of thermal evaporation with a resonant quartz rate monitor, since no RF can interfere with the resonant crystal.

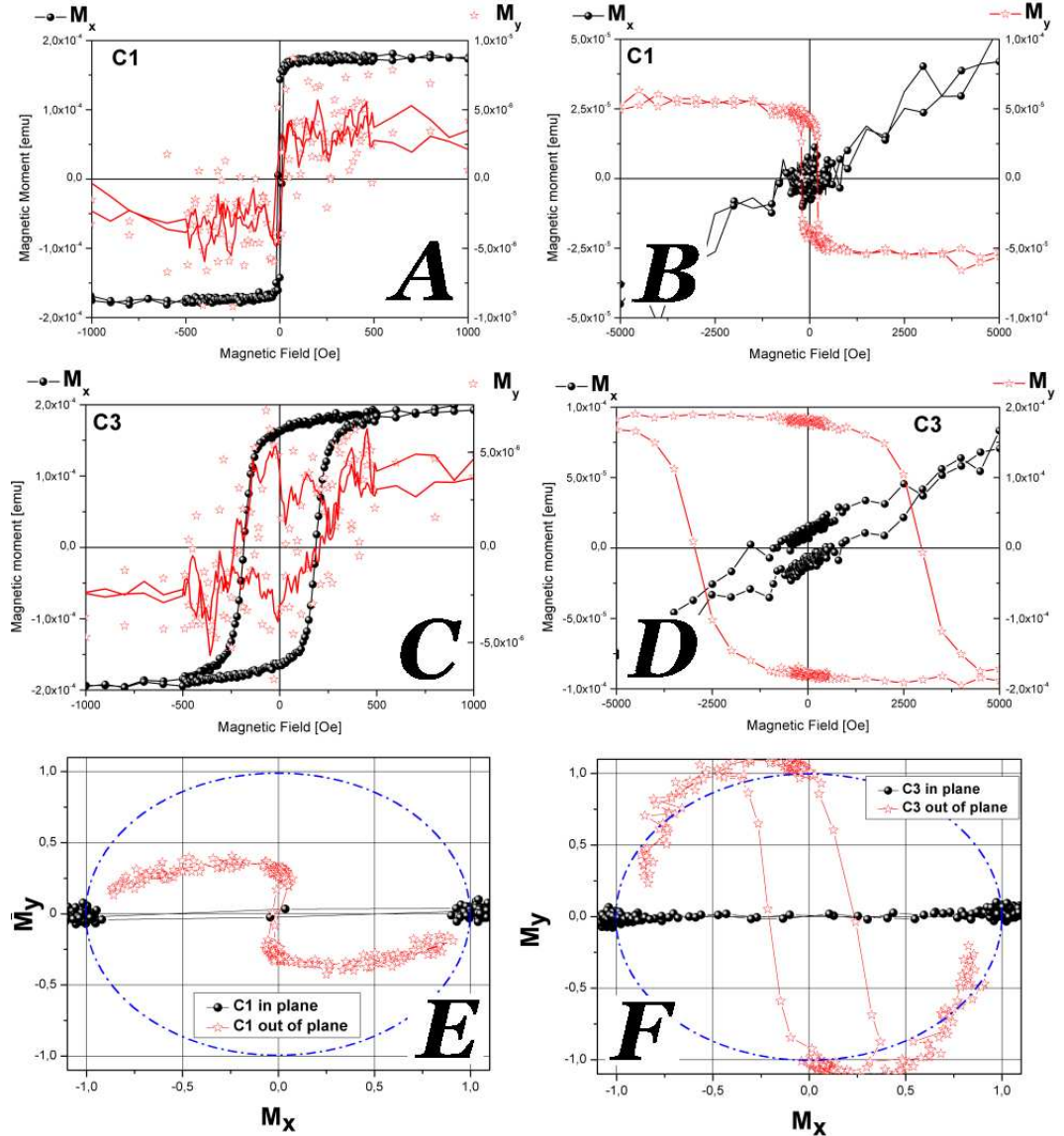


Figure 3.24. Collection of vectorial VSM analysis, relative to samples C1 (as grown) and C3 (annealed). A: field applied in plane, magnetisation in plane (black circles) and out of plane (red stars and 10-points average, red line); B: field applied out of plane, magnetisation out of plane (black circles) and in plane (red stars); C: same as A, sample C3; D: same as B, sample C3; E: polar plot for sample C1, representing the out-of-plane magnetisation as a function of the in-plane one; F: same as E, sample C3.

C/min) to allow the interdiffusion of Co and Cr atoms in the alloy. Vectorial magnetisation measurements with a vibrating sample magnetometre (VSM) (figure 3.24), together with MFM scans (figure 3.25), have been performed. Vectorial measurements allow the simultaneous sampling of two mutually orthogonal magnetisation components, which are fixed with respect to an inertial reference frame; one of the two components,  $M_x$ , is always parallel to the applied field, while the other component  $M_y$  is always perpendicular to it; by rotating the sample within this fixed configuration, one may acquire interesting information about the in plane / in plane or in plane / out of plane components [73]. The most interesting effects are those induced by the thermal treatment, evidenced comparing for example sample C1 and sample C3. The in plane coercivity is increased from 10 to 185 Oe (figure 3.24 A and C) while the out of plane coercivity is increased from 205 to 780 Oe (figure 3.24 B and D) for the component aligned with the external magnetic field, and up to 2940 Oe for the component acquired in the plane of the film. This tremendous increase has been found to be connected with a slight misalignment of a couple of degrees of the sample [74], but is also a confirm of the increased out-of-plane anisotropy and magnetic hardness of the annealed sample. The polar maps here proposed, figure 3.24 E and F, show that the as grown sample when measured with the field applied in plane, tends very easily to move the magnetisation in the same direction of the field (black circles concentrated in correspondence with the unitary circle along horizontal axis, magnetisation fully aligned with external magnetic field); when the field is applied out of the film plane, the magnetisation first moves in the plane and then, very slowly, is forced out of plane (red stars approaching towards the horizontal axis). The annealed sample in the contrary is both harder for what concerns the in plane configuration (black circles more distributed close to the origin) and easier in the out of plane configuration (a few red stars are found close to the origin).

The same behaviour may be deduced also from MFM maps proposed in figure 3.25: sample C1 shows faint stripe-like domains; sample C2 shows bubble-like domains; sample C3 shows high contrast domains, where the magnetisation is more likely to be oriented perpendicularly with respect to the film plane. The main drawback of the approach *multilayer thermal evaporation / diffusion annealing* is the poor morphology of the annealed sample, whose surface is heavily craterised. An EDX analysis has shown also that

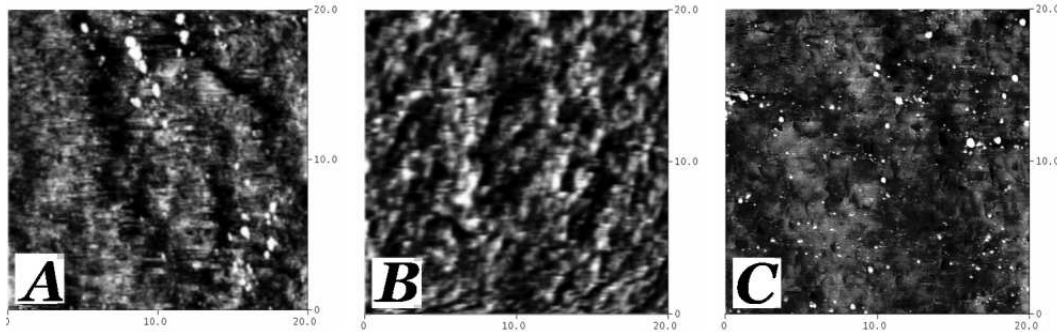


Figure 3.25. MFM images acquired over a  $20 \times 20 \mu\text{m}^2$  area with a lift scan height of 100 nm in the demagnetised out-of-plane configuration; A: sample C1; B: sample C3; C: sample C2.

the composition of the high-temperature-alloyed sample is inhomogeneous, probably because of a metastable miscibility gap that favours discontinuous precipitation and, thanks to grain boundary diffusion, generates regions with about 8 and 40 at.% of Cr [75].

The RF sputtering deposition has been experimented, together with a reduction of the annealing time, to avoid poor surface homogeneity; the thickness of each layer has been reduced, thus promoting interlayer diffusion; the new structure is  $(\text{Co}_{10}/\text{Cr}_2)^3\text{Co}_{10}$ , referred to as C4. The annealing has been done at a partial Ar pressure of 1 mTorr and keeping the sample for 1 hour at 350° C (annealed sample referred to as C5). A detailed numerical correlation of FESEM images and EDX micromaps has been used to evaluate the oxygen diffusion from the substrate towards the magnetic film C5, in order to exclude the formation of mixed magnetic oxides. The surface appears constituted by separated islands (figure 3.26 A and B, due to dewetting from the thermally oxidised silicon substrate. Depending on the greyscale value, FESEM-EDX micromap correlations have been computed making use of a technique described in detail in [76] and at page 79. Both panel C and D show that a colour transparent-hatched region has been chosen to compare EDX spectra of O, Co and Cr: from 0 to 50 and from 155 to 255 grey threshold<sup>3</sup>, respectively, corresponding to regions that are in the middle of CoCr islands, and regions that are on top of the islands; as it may be seen in panels E and F, the oxygens peaks are not over-imposed on the Co or Cr peaks, demonstrating that no diffusion occurred. An AGFM

<sup>3</sup>both FESEM and EDX images have been converted to 16 bit maps, hence featuring 256 grey values.

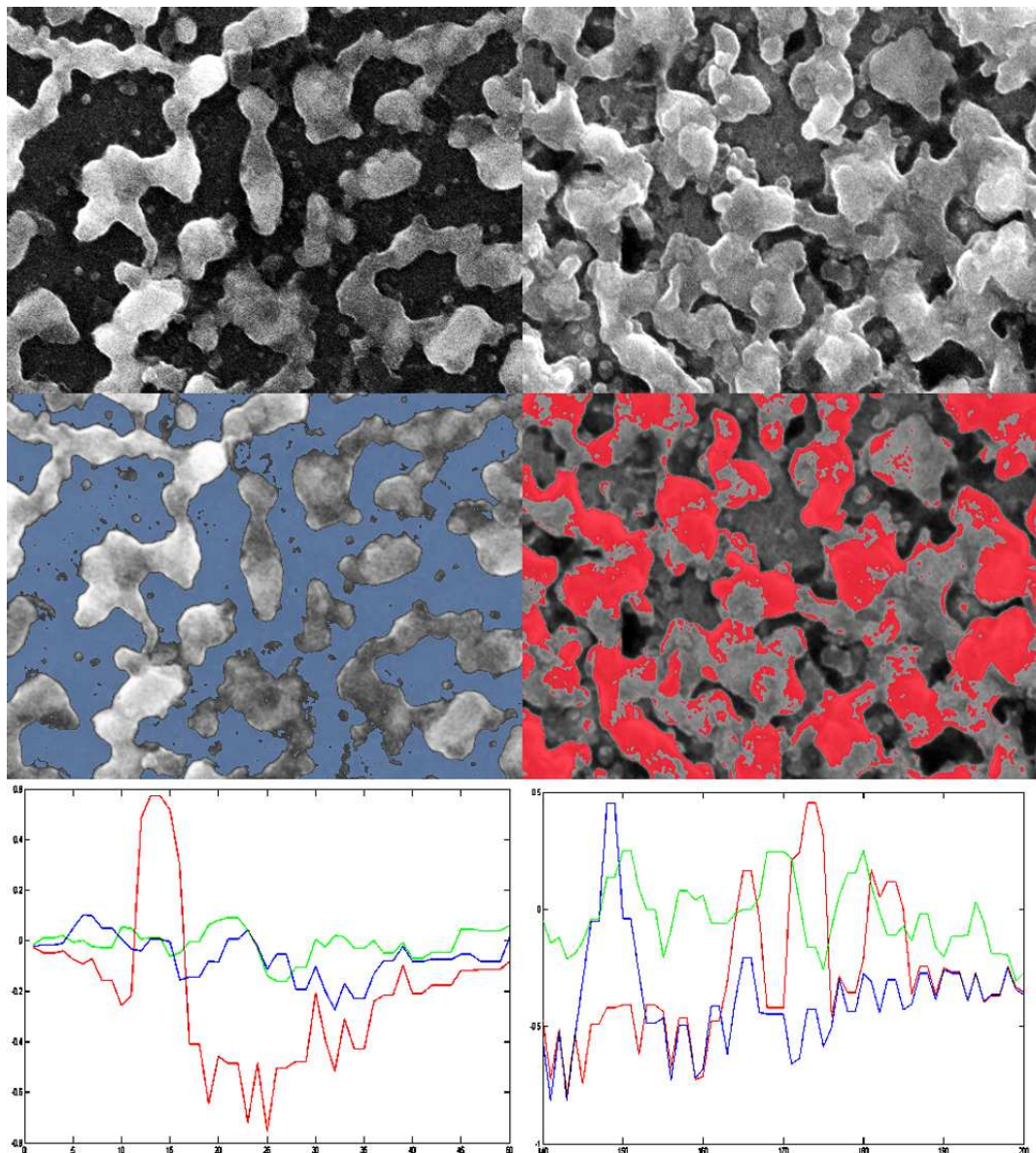


Figure 3.26. A and B: FESEM images of C5 annealed sample surface, on different sites. The area represented in panels A and B has been also used to acquire EDX spectra with 2-dimensional resolution. C and D: colour-hatched areas have been chosen for the correlation analysis. E and F: output of the correlation, spectra of oxygen (red), cromium (green) and cobalt (blue), after subtraction of the silicon spectrum background.

apparatus has allowed to evaluate at room temperature both coercivity and magnetic bias obtained after the field cooling treatment (figure 3.27): referring to the geometrical easy axis of the samples, the annealing resulted in a slight reduction of coercivity from 27 to 25 Oe, with a great increase of the bias field, from 1.5 to 10 Oe, producing a visible shift of the hysteresis loop towards positive fields. This bias may be due also to the exchange coupling provided by AFM Cr domains in close contact with ferromagnetic CoCr grains or pure Co grains. Further work is scheduled, in the direction of defining the optimal thermal treatment to provide reliable hard spin injectors for MTJs, as summarised at page 97.

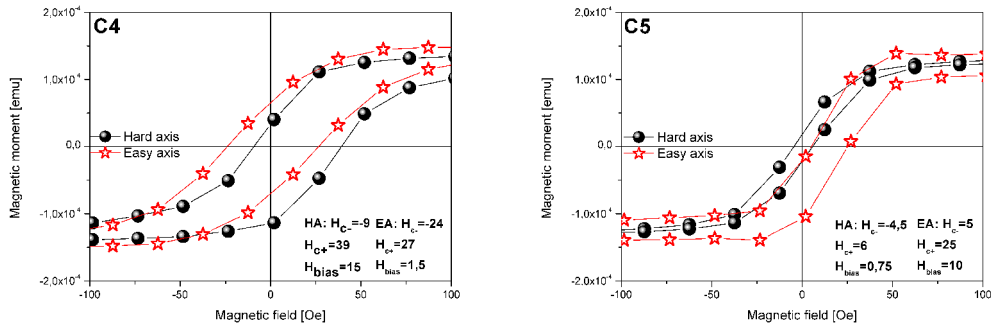


Figure 3.27. AGFM magnetisation measurements of sample C4 and C5. Indicated in the graph frame the values of positive and negative coercivities  $H_{c+}$  and  $H_{c-}$  respectively, for both easy (EA) and hard axis (HA), which may be originated by geometrical aspects such as imperfect sample cleavage; magnetic bias is also indicated ( $H_{bias}$ ).

# **Chapter 4**

## **Innovative numerical methods for data analysis and feature extraction**

### **4.1 Introduction to Vectorial and Matricial Data Handling**

A number of peculiar numerical techniques have been developed during my thesis, to face with some practical needs; all of them have been written for the Matlab ® environment. The first presented techniques are relative to vectorial data manipulation: the extrapolation of characteristic parametres from experimental curves and a genetic algorithm for data fitting. Successively, numerical techniques involving elaborations of matricial data are presented: a regional roughness analysis algorithm, a correlation algorithm to be used with SEM and EDX maps, an image registration algorithm and finally an innovative 2-dimensional entropic analysis scheme are presented.

## 4.2 Numerical extrapolation of curve characteristics

### 4.2.1 Magnetisation measurements

Magnetisation measurements, in the vectorial form (unidimensional data arrays), often suffer from thermal noise and require a postprocessing before the automated extrapolation of useful data, such as coercivity, remanence, susceptibility and saturation. The approach I propose is a direct confront between an interpolating continuous function for each of the hysteresis branches and the experimental data, which are rejected if lying outside a confidence interval. The continuous functions used to interpolate data are chosen from the Savitzky-Golay polynomial functions (SGF), also known as finite impulse response (FIR) filtering functions. The magnetic field domain of a dataset is divided into three regions, each one characterised by a different noise and a different spectral fingerprint of experimental data:

- (1) the transition region, localised between coercivity and remanence, where experimental data have a high frequency contribution;
- (2) the intermediate cycle closure region, where the two branches slowly approach and magnetic noise is stronger because of domain wall pinning;
- (3) the saturation region, where experimental data show the lowest frequency spectral contribution.

For each of those regions, the user defines the SGF parametres: polynomial order, number of points (frames) used to evaluate with the least mean squares method the best fitting function and confidence interval. Generally, the transition region requires higher polynomial orders, to follow the steep evolution of magnetisation, and a smaller confidence interval. On the contrary, the cycle closure region requires interpolating over a great number of points to increase the signal to noise ratio (SNR). The algorithm provides boundary continuity conditions (imposed on the polynomial and on the first derivative) and produces a piecewise fitting function. In figure 4.1 an example of noise reduction, together with the elimination of the diamagnetic contribution from the silicon substrate and the numerical extrapolation of magnetic characteristics, is shown.

The numerical extrapolation algorithm is used to evaluate:

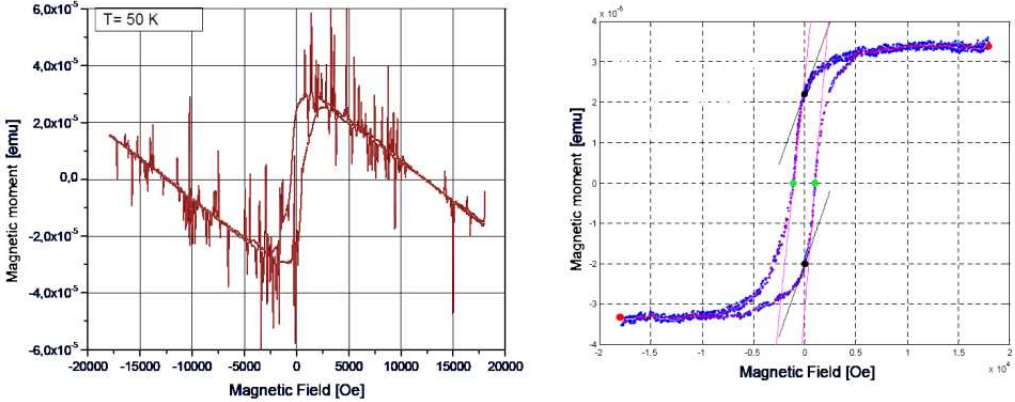


Figure 4.1. AGFM magnetisation measurements taken at 50 K of a sample of top spin valve, before (left) the noise reduction postprocessing and after (right). Notice that the diamagnetic contribution from the silicon substrate has been subtracted. The numerical extrapolation algorithm has individuated some magnetic characteristics: the two coercivities (green circles), the two remanences (black circles), the two saturations (red circles), the susceptibility at coercivity (pink straight lines), the susceptibility at remanence (black straight lines) and the overall piecewise SGFs (pink curve over blue experimental data).

- (1) positive and negative coercivities;
- (2) positive and negative remanences;
- (3) positive and negative susceptibilities at remanence;
- (4) positive and negative susceptibilities at coercivity;
- (5) positive and negative saturations or in alternative positive and negative high field susceptibilities;
- (6) magnetic bias (cycle asymmetry);

introducing as input also the magnetic film area and thickness, the algorithm converts the magnetic moment [emu] in magnetisation [emu/cm<sup>3</sup>]. Magnetic characteristics are computed as intersections of linear functions with the coordinated axis, where these functions correspond to local linearisations of the piecewise SGFs. In order to give also an estimate of the numerical error, which in the case of susceptibilities at remanence is considerably high, the linearisations are done varying the sampling step of the SGFs. A parametre

statistic is then collected and the output is built from the mean and standard deviation of those statistics.

### 4.2.2 Magnetoresistance measurements

Magnetoresistance (MR) measurements require a more complex postprocessing routine. This has been devided into optional functions that are activated with dedicated flag values depending on specific needs. These are:

- (1) data conversion and MR computation;
- (2) data resampling;
- (3) symmetrisation of upper and lower branches;
- (4) minima characterisation;
- (5) optimisation of FIR fit;
- (6) maxima characterisation;
- (7) fit and extrapolation of fit parametres;
- (8) R vs T virial coefficients extrapolation;

For the computation of MR (function (1)), I propose the following formula, with an estimate of the maximum resistance given by statistical evaluations:

$$MR = \frac{R(H) - R_{max,Gumbel}}{R_{max,Gumbel}} \quad (4.1)$$

where, as indicated, the maximum value is extrapolated using the Gumbel statistical distribution with location parametre  $\mu$  and scale parametre  $\sigma$ :

$$y_{Gumbel} = f(x, \mu, \sigma) = \left(\frac{1}{\sigma}\right) \exp\left(-\exp\left[-\frac{(x-\mu)}{\sigma}\right] - \frac{(x-\mu)}{\sigma}\right) \quad (4.2)$$

The motivation for this choice is that extremal value distributions are used to characterise wide statistics of data, represented in this case by a macroscopic resistance measure that implies an enormous statistic of microscopic scattering events. Data resampling (function (2)) is done building a standard magnetic field vector and interpolating,

where necessary, MR data with the piecewise cubic Hermite interpolating polynomials (PCHIP) method, which preserves the shape of the function (where data has a monotone slope, so interpolated values do and where data has a local extremum, so does the interpolant), avoiding slope inversions which are typical of spline interpolants (which in turn are smoother than PCHIP). MR minima (function (4)) are tracked by means of the first derivative  $dR / dH$ ; the subroutine looks for the derivative maximum and minimum, which is supposed to lay on the wall of the dip. Resistance data are sampled until a variation in the derivative sign occurs. The optimisation function (5) is a subroutine that seeks for the best fit, within the range of interest, in a least-squares sense. A parametre matrix is built, whose elements are the (odd) number of nodes used to compute the SGF FIR functions and the polynomial order of the fit. Within the error matrix, the best selection for the input parametres is chosen, corresponding to the lowest error. MR maxima (function (6)) are found by means of a subroutine which computes a fit of experimental data, using SGFs (unless the optimisation subroutine has been called) and then calculating the first numerical derivative of the fit; once again a FIR function is found for the derivative vector, in order to work on a smooth function that slowly passes through zero in correspondence of those field values that maximize the resistance. Easily this field is computed making use of a linear fit extrapolation, in a range across zero. Function (7) is used to compute analytical fits of MR curves, with user-defined functions whose  $n$  parametres are identified in the least-squares framework. Function (8) extrapolates the thermoresistive behaviour of the samples, finding the coefficients of the virial, a polynomial with user defined degree fitting the R versus T experimental points.

## 4.3 Genetic Algorithm for Data Fitting

### 4.3.1 Generalities

Optimisation problems are often characterised by the seek for a global minimum of a multiple variable function. Different approaches are possible, keeping in mind that when the problem is complex and the function to minimise has many different local minima, a Newton dichotomic approach may result in a poor fit. Hence other innovative methods

have been developed, such as the Neural Network and the Genetic Algorithm (GA) [78] [79], featuring a nonlinear approach. I adapted a GA in the Matlab ® environment in order to perform an optimisation seek in the multidimensional phase space of a multi-parametre magnetoresistive model. In figure 4.3 (A) an experimental MR curve (black line) is shown, together with the fits generated by a population of a certain generation (lines in colour).

Basically the same approach that will be described may be used to fit vectorial data with a physical model, regardless of its complexity.

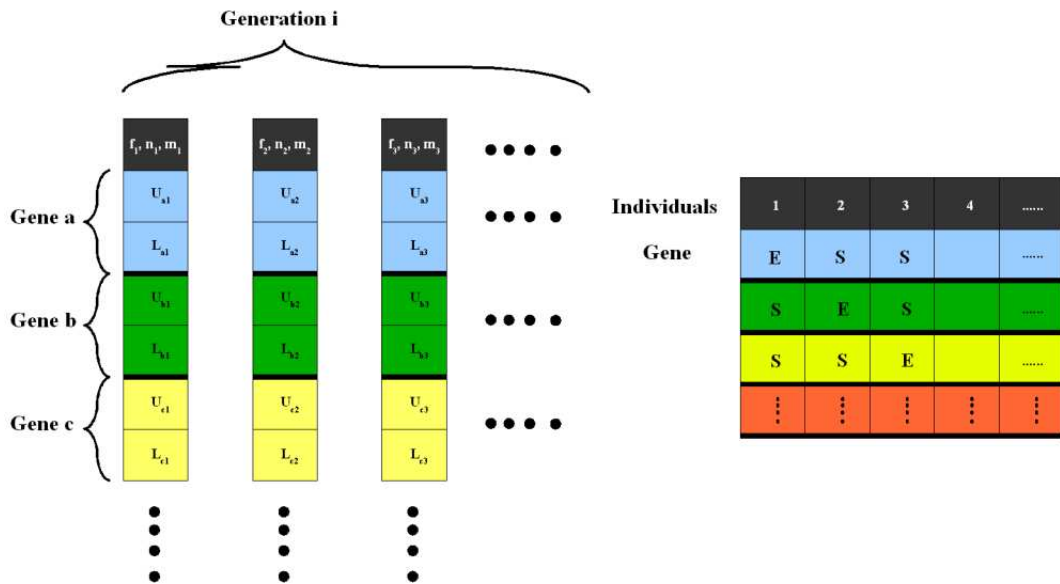


Figure 4.2. Sketch representing the code structure of each individual: vertical stripes are organised to present a flag chromosome, containing the reference name of the individual (number at subscript) and the position corresponding to its best expression; the expressed genes, with their upper and lower bounds ( $U_n, L_m$ ); the unexpressed genes where ( $U_n = L_m$ ). On the right side, the expression matrix, with the indication Expressed/Silenced in correspondence of the genes.

The concept is that a population, composed by different individuals each one having different parametres stored in its chromosomes, is tested and compared to the experimental vector. If the fit is good and the error (difference between model and experiment) is

low, a good fitness rank is associated to the individual and a higher probability of transmitting its chromosomes to the future generation is assigned; on the contrary, if an individual shows poor fitting characteristics then the probability to loose information about the values of its parametres will be higher. Each chromosome has two genes, one concerning the lower bound of the varying parametre and one concerning the upper bound (see sketch 4.2). The minimum and maximum values of the ensemble of parametres delimit a physically meaningful box in the phase space of the numerical algorithm, and a subroutine verifies at every generation that the genes respect this boundary. Only one couple of genes is expressed in the structure of an individual, in order to limit the simultaneous number of varying parametres and help one to visualize the convergence process in a 3-dimensional space (2 parametres and the fitness, see figure 4.3 B). When the chromosome remains unexpressed, its genes are set at the same value and the lower bound coincides with the upper one. A special table that I called the *expression matrix* is used to store the varying chromosomes within the genome of each individual (see sketch 4.2), since the population is redundant and there are more individuals with the same expressed chromosomes (variable parametres). When it's possible to separate shape from scale parametres, the expressed chromosomes are equally distributed between them [77]: this helps to speed up the convergence of the fitting routine, clearly separating the effects generated on the output vector by the parametres. The parametre space hence is a 2-dimensional grid, usually  $25 \times 25$  and the population  $n$  is generally composed by 16 individuals, exploring thus  $10^4$  possible configurations per generation in parallel. Each parametre is varied 25 times for each individual within the physical box using a variable step, depending on the convergence degree: when the convergence is still far (error  $\approx 1$ ) the entire parametre space is explored while when convergence proceeds the step is progressively reduced in order to refine the seek. The GA stops when error  $< 10^{-6}$ . In figure 4.3 (B) an example of individual error evaluation is shown, plotting the two expressed parametres and the computed error. In figure 4.3 (C) I propose the population evolution representation: the convergence of two randomly chosen parametres is shown, as the logarithm of the variability interval; the red circles, representing individuals of successive generations, are converging towards lower variabilities together with the ensemble convergence. An additional *flag* chromosome contains information about the best fit of each individual: the position in the  $25 \times 25$

parametre grid that minimizes the distance from experimental data and the mean square difference, which is used to assign the fitness.

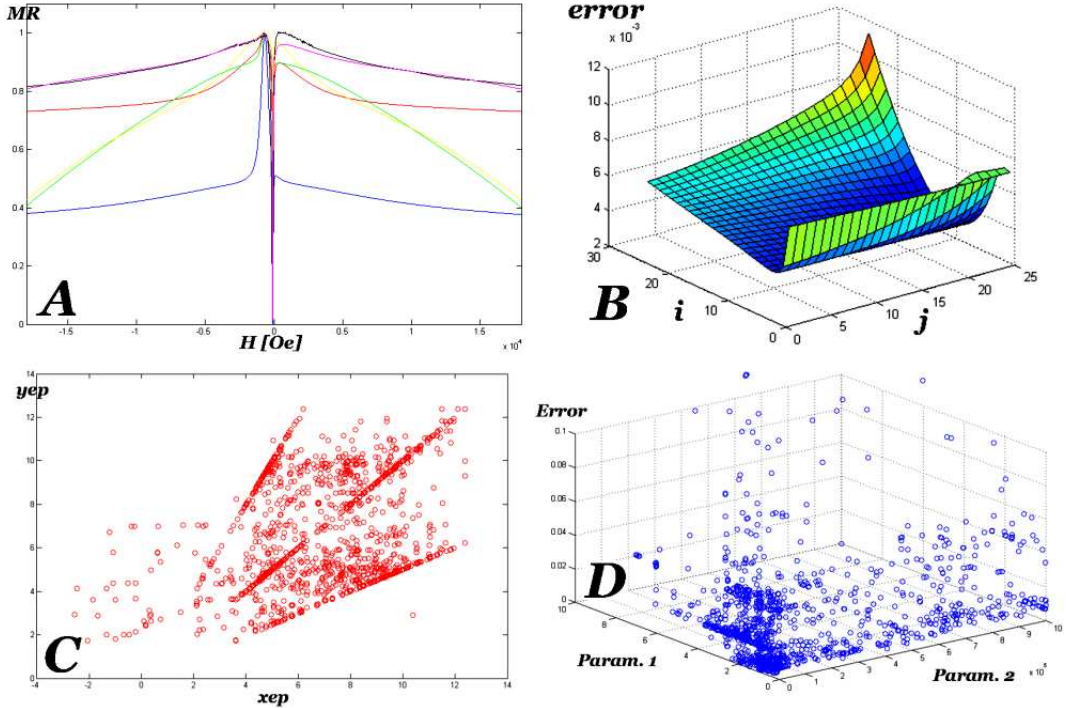


Figure 4.3. GA environment; application: fitting of experimental MR curve with a resistor network output, as described in [77]. Panel A: experimental normalised curve (black line) and some individuals with their best expression, at generation 135 (colour lines). Panel B: error surface computation for one single individual, the best of generation 135, where axis  $i$  and  $j$  individuate the expressed parametres in the multidimensional phase space. Panel C: population evolution towards convergence at generation 135, graph where each red circle represents the logarithm of the width of the seek interval relative to the expressed parametres; the linear aggregates appear because of the seek refinement mechanism, which works on logscale jumps. Panel D: population absolute error at generation 135, where the two param. axis represent a linear correlation of the phase space dimensions; each blue circle represents the best expression of each individual.

### 4.3.2 Subroutines: roulette-wheel selection, crossover, mutation and elitism

The parallel computation scheme that lies behind a GA is due to the concurrent evolution towards the local minimum error configuration of the whole population; the main drawback lies in the heavy importance of the initial *ancestor* population, the first guess for the free parametres of the physical model. A good choice is represented by a uniform distribution of the parametres within the configuration space, even if the optimal choice depends strongly on the problem that one wants to solve. In the evolution from one generation to the next one, the fitness of each individual is evaluated through the flag chromosome; a selection probability is assigned depending on the fitness and the best individuals are more likely to be chosen as example for future generations by the roulette-wheel selection subroutine. The roulette-wheel selection divides a unitary interval into  $n$  segments of different size, one for each individual of a generation, whose length is proportional to the fitness factor; then it generates a random number, uniformly distributed on the unitary interval and selects the segment that includes between its bounds the random number. Hence there is a greater probability of selecting those individuals with a best fitness, to whom a longer segment is assigned. A unique selection code prevents from selecting the same individual more than once, in order to generate homogeneous couples of different individuals. It is possible, at occurrence, to hinder the selection of the same individual for a whole cycle of  $n$  selections in order to avoid information loss and mantain the width of the configuration space. After the selection of  $2n$  old individuals is accomplished,  $n$  individuals belonging to the next generation are generated through pairing of the parents and mixing of the information stored in their chromosomes. Only the flag chromosome is left blank for the evaluation step that will assign the fitness to each individual afterwards. The next generation genome expression is assigned making use of the expression matrix, so that the order of varying parametres is blocked. The configuration space is explored thanks to two different subroutines: the first one is used to mix the available information and converge towards the local minimum (up-climb process) and is called *crossover*; the second one is used to extend the physical space of tested parametres regardless of the minima (down-climb process) and is called *mutation*. Four cases may be found:

- (1) if in correspondence of the expressed chromosome one of the parental chromosome is expressed (two is not allowed by the unique selection code), then the best choice for the children code is pointed out by the flag genes of the expressing parent, while the other parent is simply ignored; the step of the expressed chromosome children interval is chosen as explained in the following paragraph;
- (2) if in correspondence of the expressed chromosome none of the parental chromosomes is expressed, then the best choice for the children code is represented by an interval centered on the parametre value of one of the two parents (either of the best fitness parent or of an arbitrarily chosen one); the step of the expressed chromosome children interval is chosen as explained in the following paragraph;
- (3) if in correspondence of the unexpressed chromosome one of the parental chromosome is expressed, then the best choice for the children code is pointed out by the flag genes of the expressing parent; in this case the upper and lower bound coincide;
- (4) if in correspondence of the unexpressed chromosome none of the parental chromosome is expressed, then the best choice for the children code is represented by the genes of one of the two parents (either of the best fitness parent or of an arbitrarily chosen one).

The configuration space is shown in figure 4.3 (D), in a 3-dimensional subspace of it, where the error takes the z-dimension and two parametres have been chosen to represent the population; blue circles represent each individual. During the crossover process, the upper and lower bound of the next-generation-individual-parametres are chosen in such a way as to be centered with respect to the best value identified in the previous generation, whose position is stored in the flag chromosome; or they extend the fitting interval to include new values, if the best configuration is found in correspondence to either one of the two bounds or the other. The density factor that describes the sampling step for each parametre interval is generally computed as a multiple of the damping factor: the difference between the error of the actual individual and the error of the best individual, over the error of the best individual; the lower the difference between actual individual and best one, the higher the density of the sampling step. The mutation subroutine is randomly

activated in a certain percentage<sup>1</sup> of the analysed configurations to explore entirely the physically significant configuration subspace. Individuals that have been affected by a puntual mutation present altered unexpressed chromosomes and may originate either a poorer fit or a better one but help the GA to overcome local minima and complete the seek for the global minimum in the whole configuration space. In order to speed up the convergence, elitism is introduced: the best ever individual is affected neither by crossover nor by mutation but is simply transferred without modifications from the parent generation to the children one, avoiding to loose its characteristics. Only the worse individuals are affected by crossover and mutation; the worst individual is substituted by the elitism subroutine and overwritten with the best one.

## 4.4 Correlation of 2-dimensional data matrices: an application to EDX and FESEM maps

The numerical correlation between SEM and EDX maps has been proposed as a robust method to determine the superficial distribution of elements in inhomogeneous systems, such as granular alloys and patterned materials [76]. Instead of using the classic 2-dimensional cross-correlation factor, defined by the following equation:

$$ccf = \frac{\sum_{i,j} (E_{ij} - \bar{E})(F_{ij} - \bar{F})}{\sqrt{(\sum_{i,j} (E_{ij} - \bar{E})^2)(\sum_{i,j} (F_{ij} - \bar{F})^2)}} \quad (4.3)$$

where  $E_{ij}$  and  $F_{ij}$  represent the EDX and SEM data matrices respectively, and the  $\sum_{i,j}$  is made over their rows and columns, the algorithm looks for correlations between the two physical measures relative to the same specimen area making a detailed analysis at each greyscale value. An application is associated to each SEM / EDX map, usually called the colourmap:

$$\eta_{ij} : E_{ij} \subset \mathbb{N}^2 \longrightarrow GL \subset \mathbb{N} \quad (4.4)$$

---

<sup>1</sup>generally below 5%, the mutation probability may be also a function of the overall convergence, being switched off for close-to-convergence generations.

The colourmap assigns to every point of the discrete space a corresponding value on the greyscale vector ( $GL$ ). The colourmap has been divided into a certain number of slices, with a degradation of bit depth, and a number of discrete-colour matrices have been generated from the original SEM map. Each partition contains the pixel whose value ranges in a particular interval, from 0 (black) to 255 (white). As an example, in figure 4.4 the same SEM morphological image presented at page 67, figure 3.26 has been drawn applying different threshold levels: 100 (panel A), 150 (B) and 200 (C); the image-wise differential matrices, representing those pixels with greyscale value ranging from 150 to 100 and from 200 to 150 are shown in panels D and E. The EDX map is divided into finite intensity slices, from 0 (no X photon signal) to plus infinity (either an infinite number of counts coming from the same pixel or an infinite number of counts coming from a finite-size cluster of adjacent pixels). For each pixel in the image and each reduced bit depth, a positive correlation is found if an X photon signal comes from a pixel localised within the specific greyscale valued-region. If, within the same area, no X photon counts are found, a zero correlation is assigned. A normalisation step is introduced, because of the bell-shaped greyscale distribution of values found in the SEM image that can artificially increment the positive correlation for those pixels that correspond to more frequent areas.

The EDX signal distribution is much more homogeneous, instead. The algorithm output is represented by a 3-dimensional surface whose space is constituted by the secondary electron contrast, the X photon intensity and, on the vertical axis, the relative correlation (figure 4.5). A more readable representation of this correlation matrix is a 2-dimensional curve obtained by cutting said surface with a plane, positioned at a certain value of the X photon intensity, as proposed in the CoCr analysis at page 67. In that case, since the number of counts was too low to generate high intensity clusters, a mean of all the values of X photon intensity has been considered. The extended technique published in [76] features also an X photon scattering model, that produces synthetic patterns and fits experimental data, providing a robust and reliable tool to characterise inhomogeneous materials.

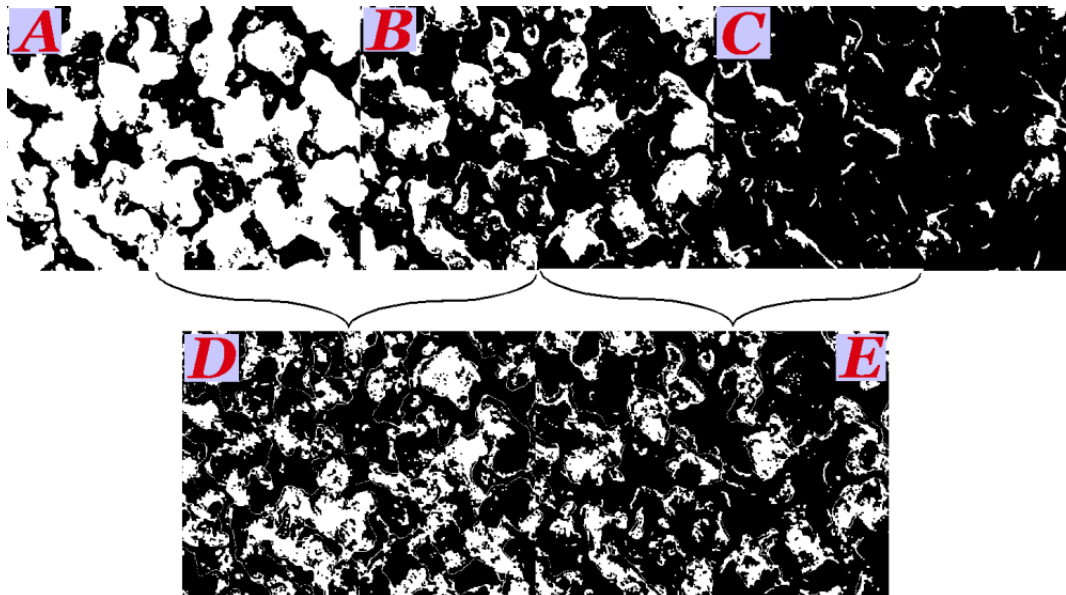


Figure 4.4. CoCr SEM map (see page 67 for details) thresholded at a greyscale value of 100 (panel A), 150 (B) and 200 (C), represented with image-wise differences ( $D=A-B$  and  $E=B-C$ ).

## 4.5 Regional analysis

Regional analysis is used to extract quantitative information from a morphological or magnetic pattern, working on the following successive phases on the input FESEM/AFM map:

- (1) conversion of the eventual colourmap into a greyscale;
- (2) contrast increment;
- (3) automatic bit depth degradation, conversion to a 2-bit image;
- (4) filling of closed areas corresponding to grains;
- (5) creation of a progressive map of recognized grains;
- (6) computation of regional properties:  $FA$  area of filled grain [pixel $^2$ ],  $C$  centroid coordinates [px],  $ED$  equivalent diametre [px],  $MA$  major axis length [px],  $ma$  minor

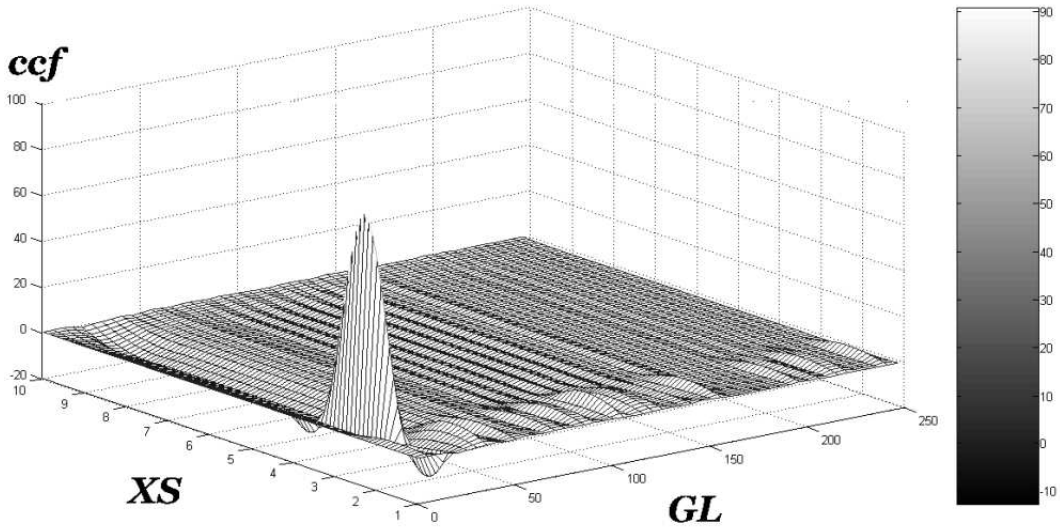


Figure 4.5. 3-dimensional correlation plot for a CoCr sample, oxygen elemental signal. The XS axis represents the X photon intensity; GL axis represents the greyscale value; ccf represents the cross-correlation factor. Notice that the entire elemental signal is found in correspondence with very dark GL values (around 20).

axis length [px],  $O$  orientation [ $^{\circ}$ ],  $EC$  eccentricity [-],  $S$  solidity [-],  $BG$  branched grains fraction [%],  $BF$  branching factor [-];

- (7) creation of regular elliptical grains with the same second moment of detected grains and synthetic representation.

It is worth mentioning that all the extracted parametres are represented by their median value and standard deviation; furthermore, the branching factor (defined as the ratio of the actual area over their fitting elliptical approximation) is given as the median value of all branched grains, excluded perfectly circular or elliptical grains. An example of the elaborations performed by the regional analysis algorithm is given in the composition of figure 4.6: starting from the MFM map shown in figure 3.6, a particular thresholding transform is applied on the colourmap, which initially is a linear application, ranging from black to white, from 0 to 255. The most common transformation is the contrast enhancement, where the normal distribution of the colour of the pixels contained in the matrix is modified in order to emphasize the image, brightening the lighter greys and darkening the darker ones. This is done modifying the linear application of the colourmap, steepening

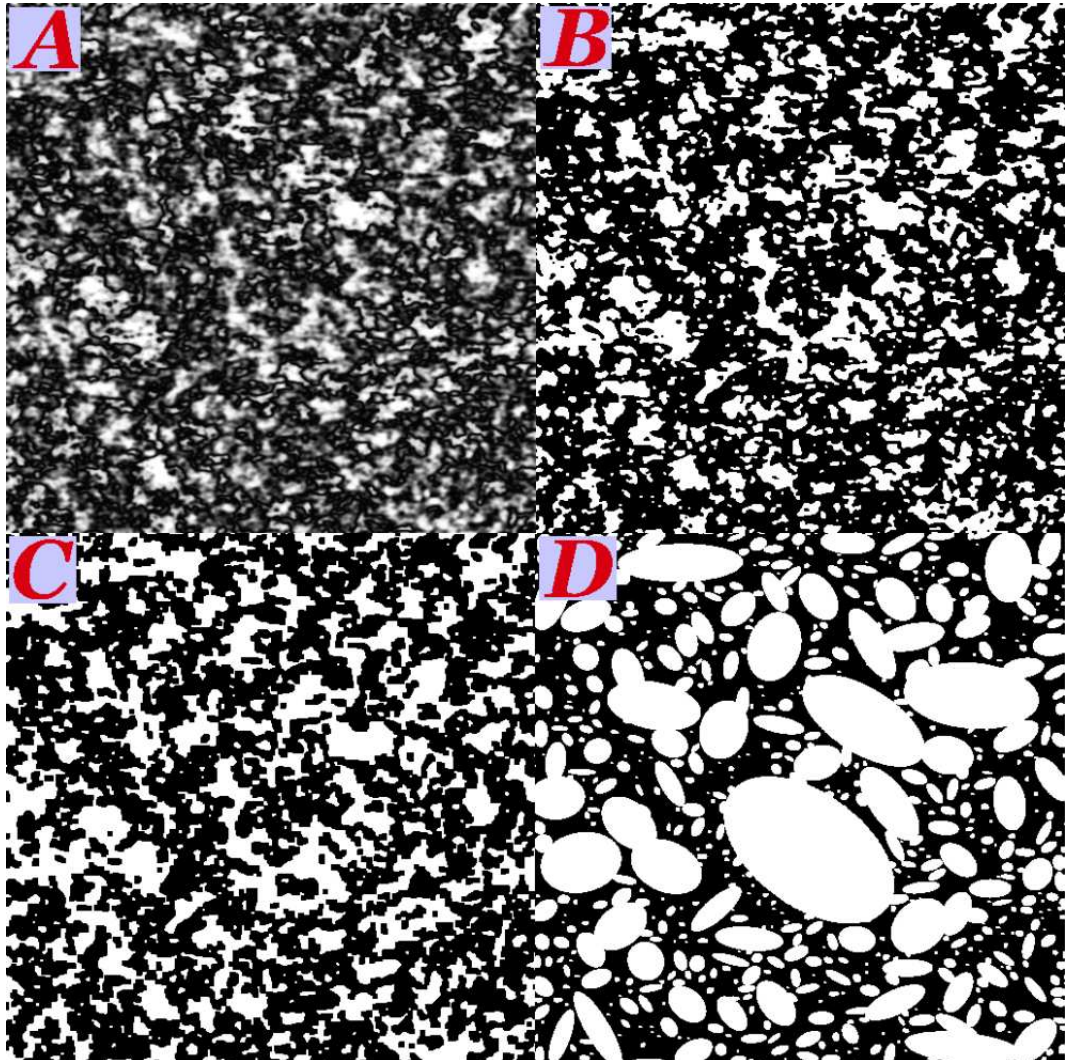


Figure 4.6. Successive elaborations on the MFM map shown at page 45, figure 3.6, generated by the regional analysis algorithm: step (2), representing the MFM image after thresholding (A); step (3), 2-bit degradation (B); step (4), filled 2-bit map (C); step (7), regular fitting grains map (D).

the slope and thresholding the upper and lower parts of the line at the respective saturation value (0 or 255). In this particular case, in order to characterise the grain roughness of a magnetic image, one has to take into account both positive and negative sample/probe interactions, so the linear application is transformed into a nonlinear "V-shaped" function that transforms black into white inverting the gradient sign, keeps white and assigns black

to an intermediate grey level. The result is shown in figure 4.6 (A). Step (3) produces the 2-bit map shown in panel (B). Step (4) produces the 2-bit map shown in panel (C). The progressive map generated after the recognition of the grains is an indexed map, where each grain is assigned to a progressive colour, as shown in figure 4.7. The representation is a 3-dimensional image, where the height is proportional to the colour index. The computation of regional properties for each of the detected grains produces a numerical output, as well as a synthetic pattern of grains, a collection of ellipses whose second moment coincides with the second moment of detected grains, as shown in figure 4.6 (D).

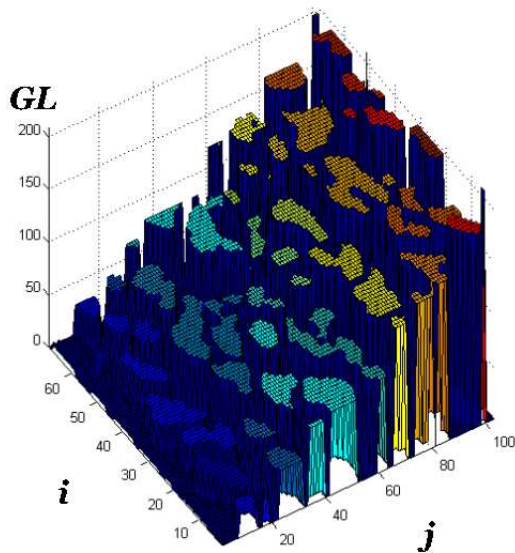


Figure 4.7. 3-dimensional representation of indexed image, showing detected grains from a topographic FESEM image. The grain height is proportional to the colour index.

## 4.6 Image Registration for matricial data handling

### 4.6.1 Introduction: MFM data acquisition

The image registration (IR) technique has been widely used in the postprocessing of aerial and satellite photographs [81] [82] [83]: by applying a geometrical transform it is possible either to overimpose different frames representing the same terrain area and

realise a patchwork of images covering a wider surface or to increase the information content of the image, if the different frames have been acquired at various wavelengths. In this framework I have developed an IR algorithm in the Matlab ® environment, making use of the Image Processing Toolbox 4.2, to MFM 2-dimensional data matrices, demonstrating its possibilities in matter of image contrast and quality enhancement [80]. Since the scanning probe microscopy is a time-consuming characterisation technique, stability problems may be found during the acquisition of an image: nanometric shifts of the sample during the probe movement result in an affected image that may be wrongly interpreted. Furthermore the high precision piezo drive that moves the probe back and forth suffers from the so called *creep* effect: when a large voltage is suddenly applied to the piezo, the displacement response of the tip follows a slow saturation curve, reaching the expected deformation after a finite time, typically while the acquisition process is already started. In order to compensate the artifacts and deformations induced by the described phenomena, the IR technique is able to completely recover them, providing that at least one image is deformation free. When the MFM apparatus has been carefully left stabilise acquiring data along one single fast track, the first data matrix is probably deformation free; a subsequent acquisition of the same sample region will be affected, without the same stabilisation, by the creep induced by the repositioning of the tip from the position  $(n,m)$  to the position  $(1,1)$ , where  $(n,m)$  is the size of the data matrix. This happens also because the typical size of the investigated region is in the tenth of  $\mu\text{m}$  and the creep is evident at that scale.

#### 4.6.2 Acquisitions with mutually orthogonal fast scan axis

We found interesting, in order to apply the IR, the use of subsequent scans acquired with mutually orthogonal fast scan axis; the principal reason of considering magnetic images of the same area with different fast scan axis resides in the complex magnetic configuration of the magnetic tip, which is far from being an ideal magnetic dipole. When the probe cannot be considered as a dipole, one must take into account, in interpreting the MFM data matrix, also the relative orientation of the tip anisotropy axis with respect to the normal to the film plane. Interpolating the information of the two subsequent scans can compensate the influence of such a complex probe magnetic configuration. As an

example, we show the IR algorithm input and output, consisting of two AFM data matrices (figure 4.8, panel A and B) and the corresponding two MFM datasets (figure 4.8, panel C and D), relative to a patterned soft magnetic material which represents an optimal case study due to its regularity. The reference image, which is believed not to have been affected by deformations, is called the *base* image, while the deformed image that has to be adapted to the base is called the *input* image. After applying the inverse transform, the images are perfectly matched over the same area and their information content may be manipulated using simple algebraic operators. The topographic differential matrix of figure 4.8, panel H (red contour lines), computed on the AFM datasets

$$D_{ij}^{AFM} = A_{ij}^{0^\circ} - A_{ij}^{90^\circ} \quad (4.5)$$

shows that the greatest difference between the subsequent scans resides in the single dot edge, due to the imperfect circular symmetry of the tip section profile, whose convolution with a steep wall produces different outputs depending on the angular profile in contact with the sample, which in last analysis depends on the fast scanning direction of the tip. The magnetic differential matrix, computed on the MFM datasets

$$D_{ij}^{MFM} = M_{ij}^{0^\circ} - M_{ij}^{90^\circ} \quad (4.6)$$

shown in figure 4.8, panel H (greyscale bitmap in the background), confirms that the greatest difference is localised in regions completely uncorrelated with the previous matrix; the convolution process above described is not responsible for the  $D_{ij}^{MFM}$  data, since the tip is not any more in contact with the sample, but raised of a well defined value and flown above the sample. A physical source for nonzero elements in the magnetic differential matrix comes from the nonuniform magnetisation configuration of the scanning tip or from a magnetically unstable sample that changes its configuration evolving towards a more stable state after a finite time.

### 4.6.3 Preprocessing: thresholding and filtering

Both the raw AFM and MFM datasets come as double signed floating point matrices ranging from  $-2^{16}$  to  $2^{16}$ . The greyscale vector length is reduced to  $2^8$  bit with a discretisation subroutine. A thresholding subroutine is performed on the so codified AFM

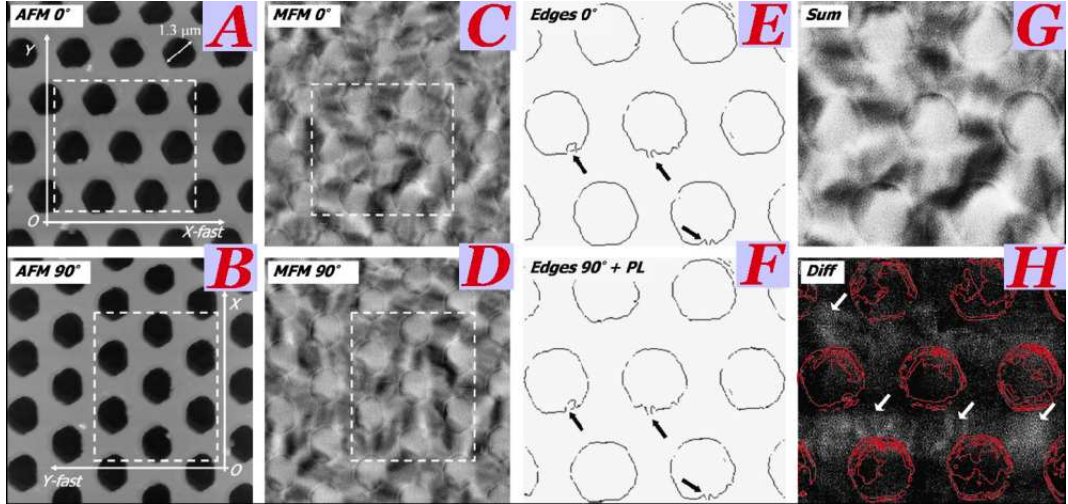


Figure 4.8. MFM image registration process, adapted from [80]. A patterned Co 65 nm thick-film, with an hexagonal lattice of 1.3  $\mu\text{m}$  in diametre and 1  $\mu\text{m}$  in pitch, has been analysed by AFM/MFM acquiring two subsequent scans with mutually orthogonal axis (A, C: 0°, B, D: 90°). A portion of the image has been filtered in order to put in evidence the edges and manually identify matched pair points (E). After applying the transform, edge image features are perfectly matched with the base ones (F: edge 90° image after transformation obtained with a piecewise linear function). Matched maps may be treated by means of algebraic operators: sum (G) and difference (H). If compared to untreated images, panel G features an increased SNR and optimised contrast. A closer look at panel H confirms that the difference between topographic maps (red contour lines) is localised on the edge of anti-pillars, while the differences between magnetic maps (greyscale bitmap in the background, pointed by white arrows) are not correlated with topography.

and MFM datasets histogram: histogram curves are generally belly-shaped, with a global asymmetry and some spikes localised at the two saturations and at other greyscale values; after the application of the thresholding subroutine the histograms are slightly stretched and the number of pixels lying in the saturation spikes is augmented. After this preconditioning, only the AFM images are treated since it is easier to identify corresponding spatial locations in the morphological matrices  $A_{ij}^{0^\circ}, A_{ij}^{90^\circ}$  than in the magnetic ones. In order to increase the image readability a Wiener filter is applied to the datasets, whose purpose is the noise reduction; this subroutine computes the local average and variance for every pixel in a block-wise tessellation of the matrix and substitutes each pixel with a weighed value based on the local mean. Qualitatively the Wiener acts as a high-pass filter and removes the high frequency noise, making topographic structures emerge from

the background. In cascade after the noise removal a Sobel filter is applied: the horizontal and vertical gradients of the topographic datasets are computed and their absolute values sum is given as output. This operation qualitatively corresponds to an edge enhancement, since local high-gradient regions represent the transition between a topographically low area and a high one (or viceversa); found edges appear as white lines and spots on a black background, revealing defects and other morphological features (see figure 4.8, panel E, F).

#### 4.6.4 Pair matching and inverse transforming

So called control points are user-identified in the base  $A_{ij}^{0^\circ}$  and mapped to new and corresponding locations in the input image. There are different spatial transformation applications handled by the IR algorithm; these transformations are categorised in two groups: global and local, depending on the portion of matrix that is processed by the algorithm. A very simple example of global application is the conformal transform, which accounts for a scaling  $S_{x,y}$ , a rotation  $\alpha$  and/or a translation  $T_{x,y}$  of the input matrix  $A_{ij}$ :

$$B_{ij} = \begin{pmatrix} S_x \cos(\alpha) & -\sin(\alpha) & 0 \\ \sin(\alpha) & S_y \cos(\alpha) & 0 \\ T_x & T_y & 1 \end{pmatrix} \begin{pmatrix} A_{ij} \\ 1 \end{pmatrix} \quad (4.7)$$

Other supported transformations are the affine, corresponding to a shear of the metric space on a particular direction, where each dimension is scaled independently; the projective transform, which is a generalisation of an affine transform, where each dimension scales depending on the other; the polynomial transform, where the metric is warped following a polynomial function (up to third order polynomials are considered); the piecewise linear transform, which is a local linear deformation of the metric, allowing different warps on each triangulation of the image area [84] [85].

#### 4.6.5 Acquisitions with external magnetic field

Quantitative MFM analysis have represented so far a very difficult task, because of the complex reconstruction needed to transform the sample/tip interaction map into a magnetic surface charge map, without a high gain in definition, accuracy and effectiveness

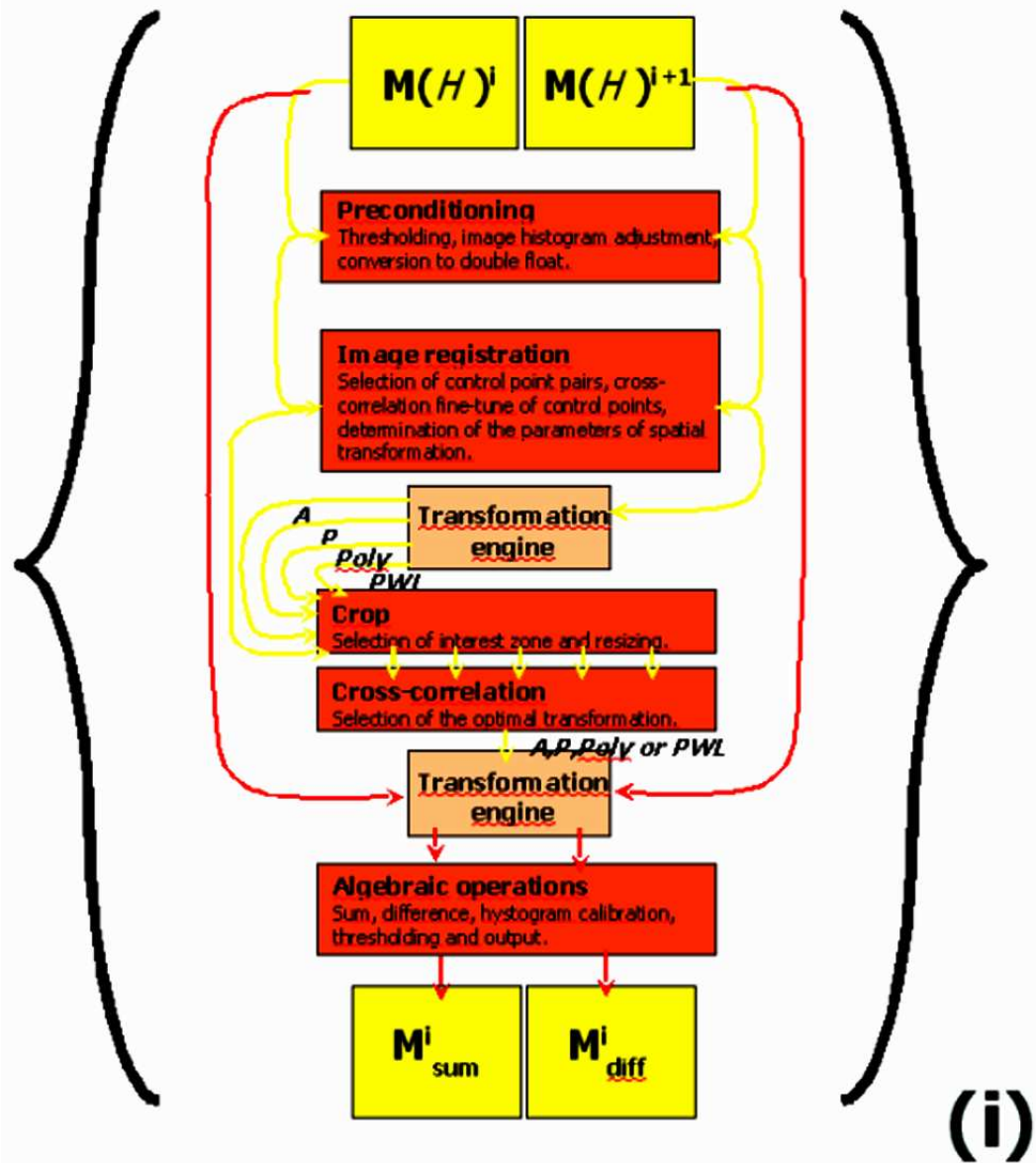


Figure 4.9. Flow chart representing the IR algorithm core, modified in order to operate on MFM data matrices acquired with different magnetic fields. Here the progressive index  $i$  denotes the sequential acquisition. The output is represented by the algebraic sum and difference between two adjacent maps.

[86] [87] [88] [89]. In the following section a set of statistical instruments will be introduced, to extract some precise, quantitative information from MFM data matrices. Before

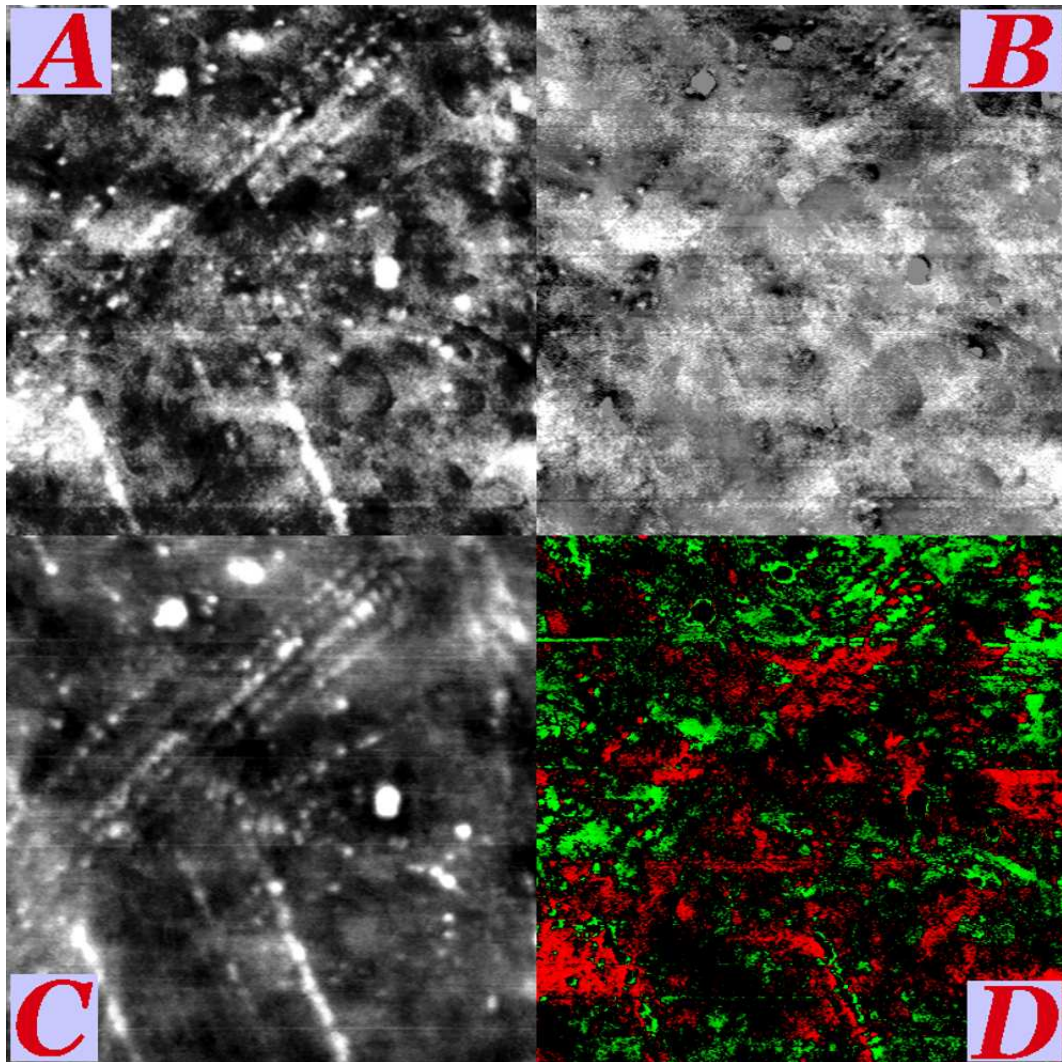


Figure 4.10. Example of elaborations obtained as output from the algorithm sketched in figure 4.9. A: registered MFM image of a CoCr sample surface, acquired at  $H = -100$  Oe (in plane), over an area of  $15.5 \times 15.5 \mu\text{m}^2$ . B: overall sum of MFM registered images of the same area, acquired at the following in plane fields:  $H = -100, -32, -16, -8, 0, 8, 16, 32, 100$  Oe. C: resulting image at  $H = -100$  Oe after the subtraction of the SEMap. D: differential magnetic matrix obtained from the two frames,  $H = -100$  and  $H = -32$  Oe, with a peculiar colourmap assigning green to the positive interaction, red to the negative one and black as intermediate value.

this, it is necessary to introduce the application of the IR algorithm in case of frames acquired with the same fast scan axis but with a parametric external magnetic field applied to the sample. The first frame, usually taken with a saturating field applied in the plane of

the film, generated by a Helmholtz coil, is used as a reference; other frames are perfectly matched to this one thanks to the IR routine above introduced. Topographic images are not considered here. In figure 4.9 a flow chart diagram is shown, representing the same IR core algorithm above discussed but restricted to MFM matrices  $M(\mathcal{H})^i$  acquired with different magnetic fields. Once all the matrices have been treated, it is possible to compute the overall sum; this map, shown in figure 4.10 (C), does not contain those features that during the field cycle are averaged to zero, for example a field dependent tip/sample interaction whose sign changes from positive to negative, or viceversa. On the contrary, all those systematic interactions independent from the external field whose value is not averaged but increased, such as stray fields either diverging from or converging to topographic inhomogeneities, are enhanced. For this reason I called figure 4.10 C a *systematic error map* (SEMap); it may be subtracted from each frame, increasing the SNR proportionally to the square root of the number of frames.

## 4.7 Statistical Analysis on 2-Dimensional Data Matrices

A statistical analysis approach on 2-dimensional data matrices has been investigated in the pattern recognition and artificial vision field [90] [91] [92]; tools developed for numerical extrapolations and image compression are proposed as extremely precious in the quantitative analysis of MFM data. A first glimpse on the importance of such analysis is given by figure 4.11: the histogram representing the greyscale distribution of pixels relative to the MFM image of a patterned material, demagnetised in the plane of the film, shows a uniform coverage. The magnetisation also should be uniformly averaged in the plane of the film. A connection between the two quantities has to be found.

Here the most important spectral and statistical measures of randomness are introduced [93]:

$$E(M_{ij}, m, n) = -\frac{1}{mn} \sum_{u=1, v=1}^{m, n} \sum_{\eta=0}^{255} h_\eta(x_u, y_v) \log(h_\eta(x_u, y_v)) \in [0, +\infty) \quad (4.8)$$

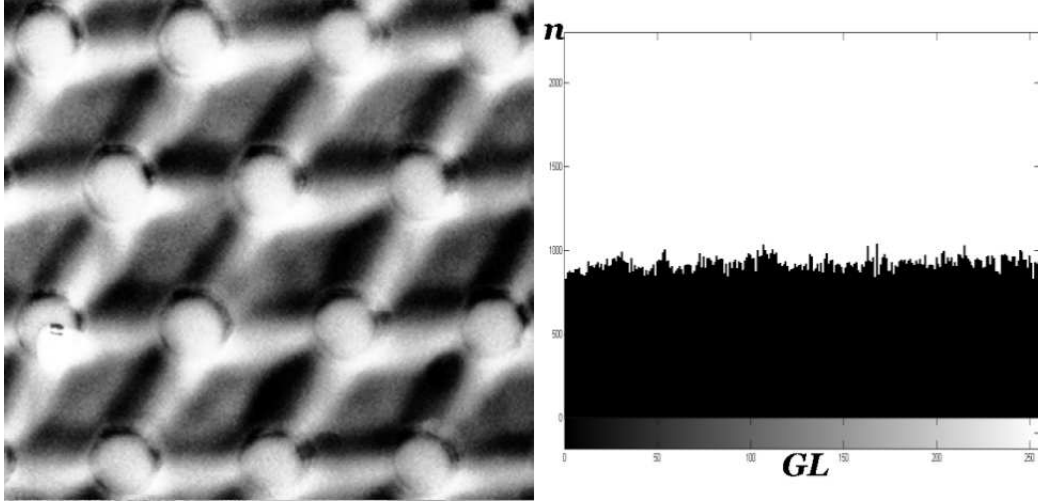


Figure 4.11.  $20 \times 20 \mu\text{m}^2$  MFM sum image ( $0^\circ + 90^\circ$  registered) of an hexagonal pattern of Co anti-pillars, adapted from [94]. On the right, histogram of the greyscale distribution of the pixel, surprisingly uniform over the whole domain.

$$GLCM_{\eta_i, \eta_j, \theta}(M_{ij}, u, v) = p_{\eta_i, \eta_j, \theta}(x_u, y_v) \quad (4.9)$$

$$C(M_{ij}, m, n) = \sum_{u=1, v=1}^{u=m, v=n} |u - v|^2 \langle GLCM(u, v) \rangle_\theta \in [0, \eta_j^2 - 1] \quad (4.10)$$

$$H(M_{ij}, m, n) = \sum_{u=1, v=1}^{u=m, v=n} \frac{\langle GLCM(u, v) \rangle_\theta}{1 + |u - v|} \in [0, 1] \quad (4.11)$$

Equation 4.8, defining the statistical entropy based on Shannon formulation and obeying the Boltzmann-Gibbs-Shannon statistics (BGS), is a scalar when  $M_{ij}$  is an  $m \times n$  matrix, otherwise it is a matrix composed by the entropies computed on the tessellation of  $M_{ij}$ , in a block-wise analysis. The other texture quantities, contrast and homogeneity, require the definition of the statistical matrices. One of them is global, the grey level co-occurrence matrix (GLCM), which has been defined in equation 4.9. The GLCM is a multidimensional array, composed by slices of square matrices, computed depending on the cartesian coordinates of a displacement vector  $(u, v)$  that is used to compare the pixel of interest  $(i, j)$  with a reference pixel pointed by the characteristic radius  $(r_i, r_j)$ . Since the statistics are mediated on a  $360^\circ$  angular space with a  $45^\circ$  step, for each radius 10

GLCM slices are generated by the computation process. Characteristic features will be extracted loosing the angular resolution as mean values, but keeping the linear resolution. The rows of each square matrix represent the grayscale value of the pixel of interest, while the coloumns represent the grayscale value of the reference pixel; the function  $p_{\eta_i, \eta_j, \theta}$  counts how many pixels in position  $(i,j)$  of intensity  $\eta_i$  are found in position  $(r_i, r_j)$  with an intensity  $\eta_j$ . Intuitively, an extremely rough texture on a certain length scale generates a diagonal GLCM over a corresponding characteristic radius: this means that there is no correlation between different portions of the image. Depending on the original image depth (8 or 16 bits), the GLCM should have stacked layers of up to  $256 \times 256$  elements; generally it consists of a sparse matrix, for a partially ordered pattern of magnetic domains, and a diagonal matrix, for a random noise pattern. In order to speed-up computing time and reduce the risk of extracting low density information the bit depth is decreased to only 4 bits (one single GLCM layer is a  $16 \times 16$  matrix). Intuitively, the contrast defined in equation 4.10 is a measure of the difference between the pixel of interest and its neighbour over the whole image, ranging from 0, which corresponds to a constant image, to  $(\eta_i - 1)^2$ . Homogeneity (equation 4.11) is a scalar indicating quantitatively how much the GLCM is close to be a diagonal matrix (uniformly distributed noise in the MFM image), ranging from 0 to 1 (diagonal case). As a preliminary analysis some results are proposed. In figure 4.12 the extension of the IR algorithm is presented; in figure 4.13 an innovative 3-dimensional diagram, showing entropy, homogeneity and contrast of each analysed map as a *texture trajectory diagram* (TTD) in the ECH volume. In particular it is worth noting that the overall sum SEMap texture characteristic (black continuous line) traces a path which is definitely separate from the other cases (coloured lines); the circles are used to track the investigated dimension, ranging from the least significant bit (1 pixel  $\approx 20$  nm) up to half of the image (100 px  $\approx 2 \mu\text{m}$ ). In conclusion, another innovative graphic representation is shown, a 3-dimensional *magnetic texture phase diagram* (MTPD), where the entropy has been reported in function of the two independent variables: magnetic field and feature size.

In this particular graph entropy has been computed in a block-wise analysis, keeping a spatial resolution, and subtracted by the mean saturation value. After interpolation, a smooth 3-dimensional surface is generated, giving interesting information about high

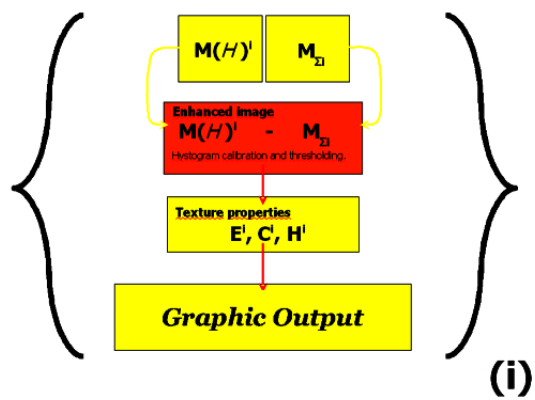


Figure 4.12. Flow chart of the entropic analysis algorithm, that analyzes MFM maps acquired with different magnetic fields

entropy patterns corresponding to disorder developed at certain scales close to zero field (remanence) and low entropy patterns corresponding to order developed close to coercivity.

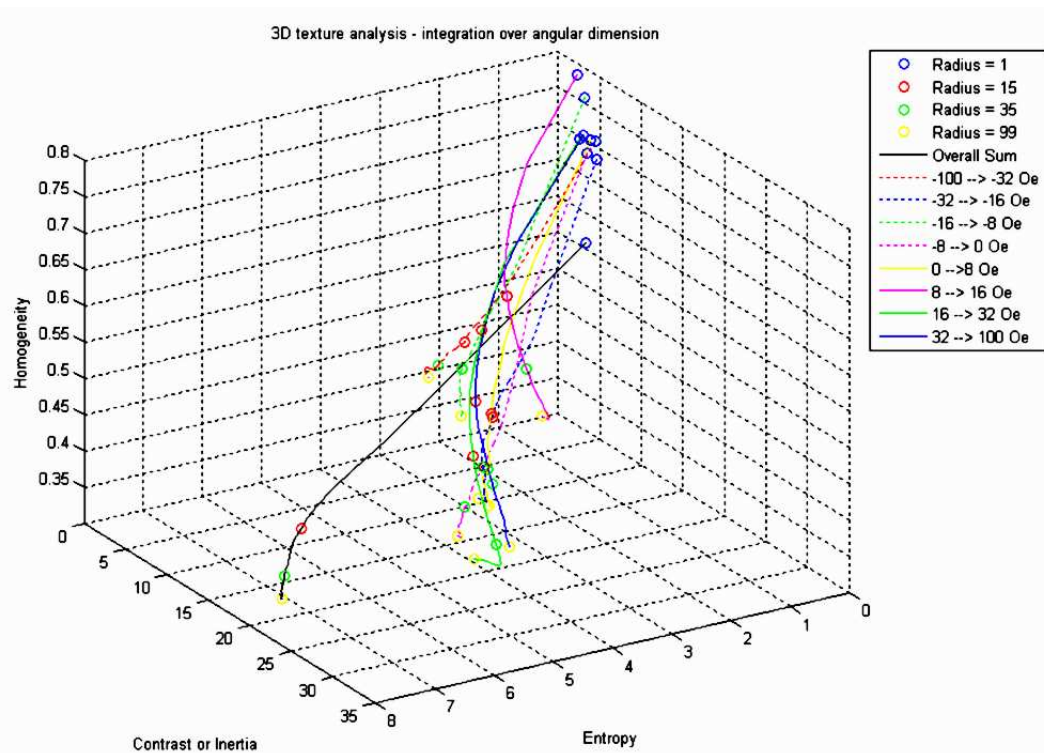


Figure 4.13. Texture trajectory diagram (TTD) in the entropy-contrast-homogeneity (ECH) volume, for a CoCr specimen analysed at various fields, as indicated, sampling the MFM maps from the maximum instrument resolution (20 nm, radius = 1) up to half of the map size (2  $\mu$ m, radius = 99).

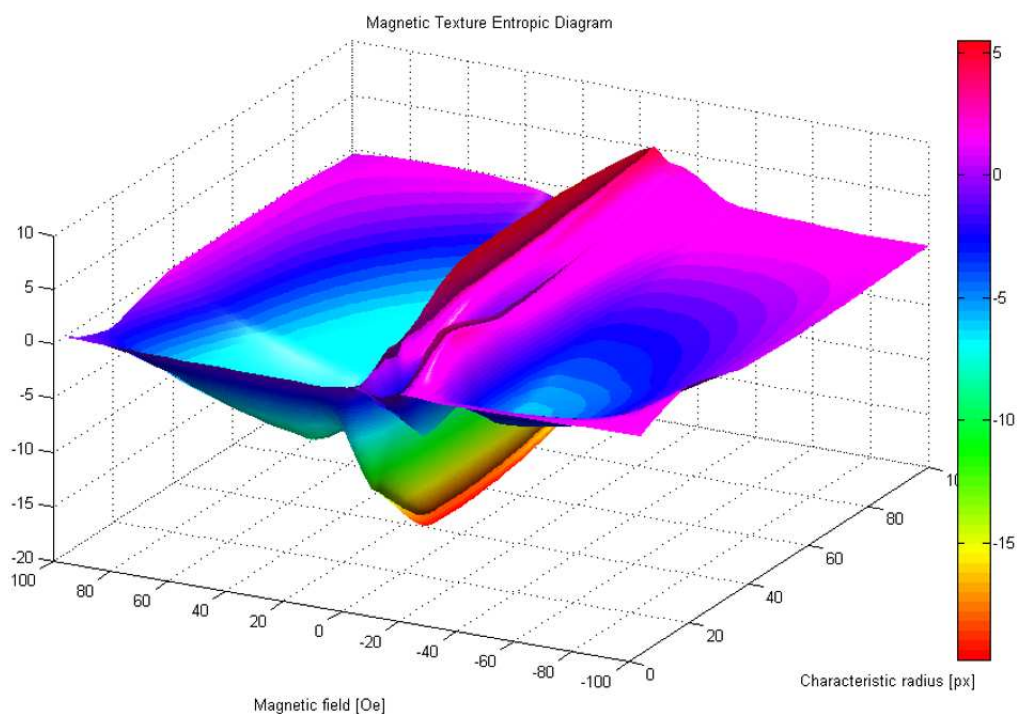


Figure 4.14. *Magnetic texture phase diagram (MTPD); the vertical axis is represented by an entropy which has been subtracted by its saturation value.*

# **Chapter 5**

## **Future Developments**

Many improvements have been scheduled for future research work in spintronics at Politecnico.

### **5.1 Prototypal deposition system development**

The vacuum degree and in ultimate analysis the quality of interfaces and devices may be improved with the implementation of a cryosorption system and an ionic pump; in particular the liquid-nitrogen-cooled copper plate that will adsorb gases and vapours in the chamber is a custom and cost-effective solution (figure 5.1).

### **5.2 Process development**

Preliminary work will be done to standardize the process for obtaining at least micrometric tunnel junction areas (figure 5.2). Preoxidation will be experimented as a method for suppressing the orange-peel coupling, as recently reported [95]. CoCr will be implemented as hard spin injector.

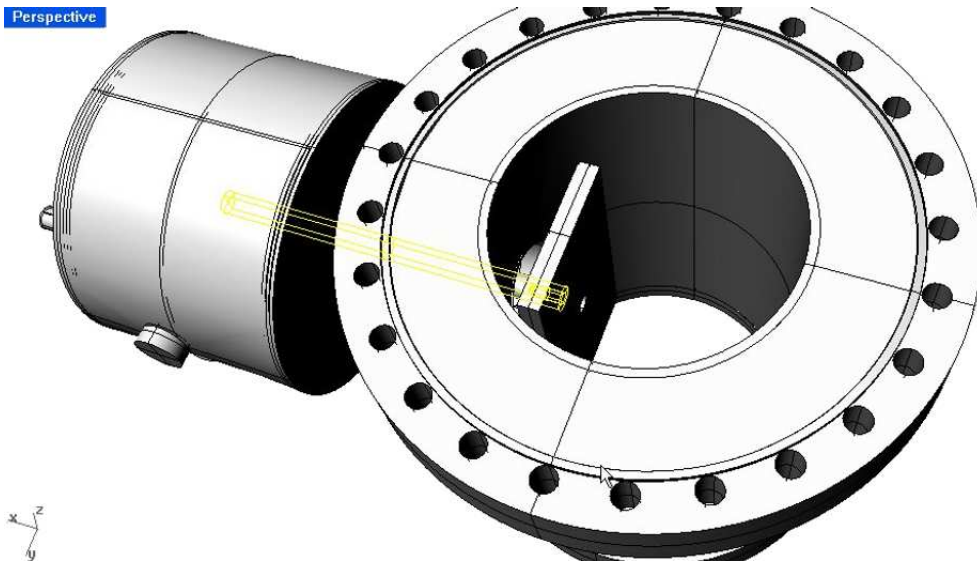


Figure 5.1. Courtesy of Eng. Paolo Mori. Vacuum tank for the liquid nitrogen storage (left), with a steel thermal pipeline (yellow prism lines) posed in thermal contact with a copper adsorption trap (plate inside the flange).

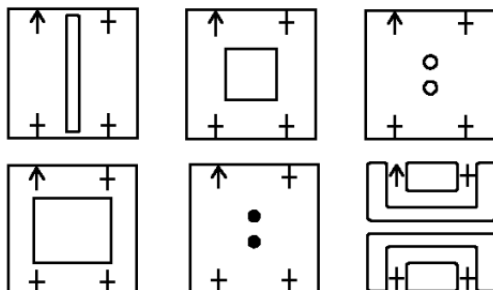


Figure 5.2. Optical lithography masks that will be used to standardize the fabrication process. From top to bottom, from left to right: bottom copper electrode, AFM mask, MTJ mask, insulator mask, MTJ inverted mask, top copper electrodes.

### 5.3 Numerical analysis

For what concerns the numerical entropic analysis, a test on synthetically generated patterns (figure 5.3) is necessary to calibrate the innovative TTD and MTPD diagrams. Implementation of a 2-dimensional block-wise entropic analysis, based on the Abutaleb definition of entropy or on esoteric definitions, such as the Tsallis entropy [96] [97] [98],

will be evaluated.

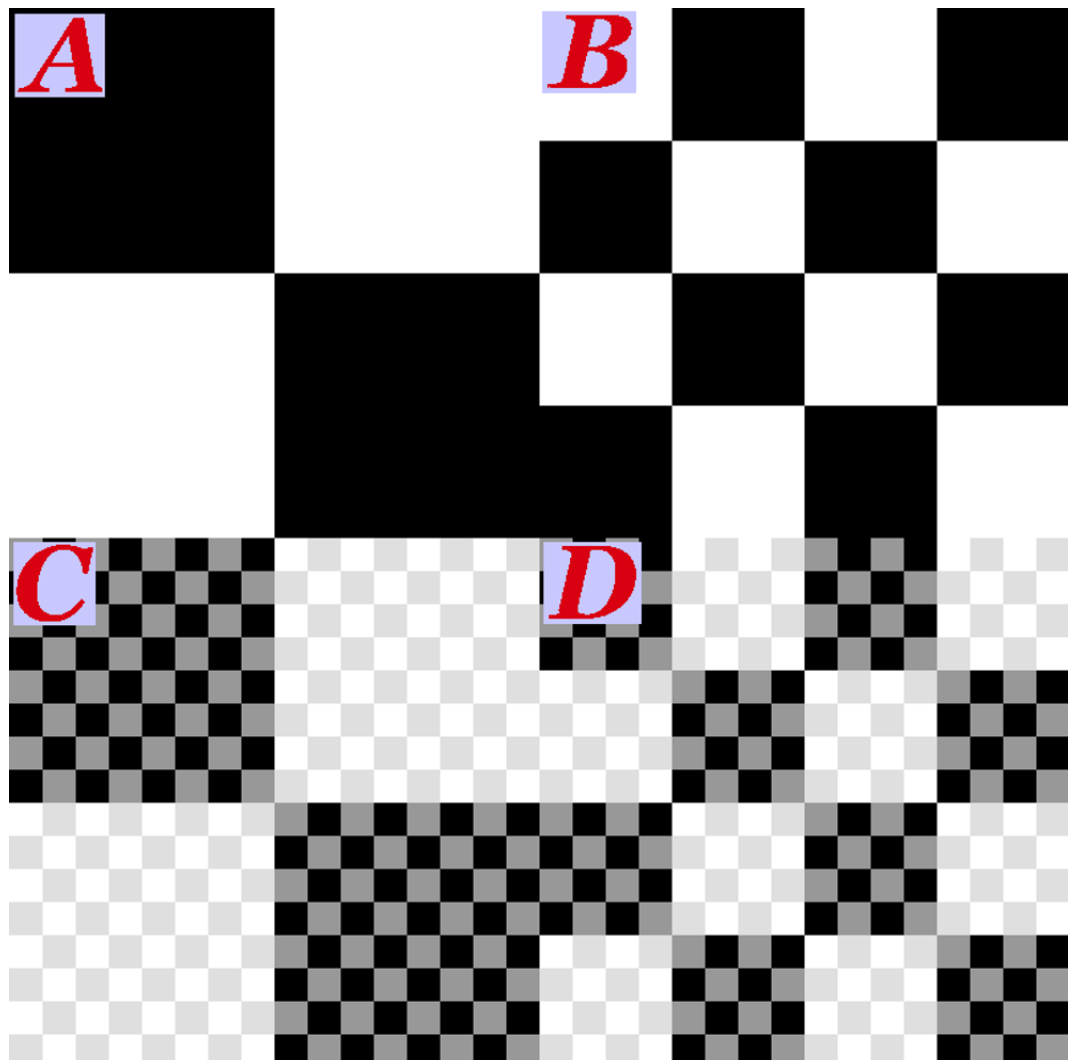


Figure 5.3. Artificial patterns generated to evaluate the TTD and MTPDs. A: two bit pattern with a square lattice and a periodicity of 200 pixel unities; B: two bit pattern with a periodicity of 100 px; C: 4 bit pattern with a multiple periodicity, at 200 and at 25 px; D: 4 bit pattern with 100 and 25 periodicities.



# Chapter 6

## Conclusions

In conclusion this thesis work consisted of three principal activities: the refurbishment and optimisation of a prototypal multitarget sputtering for thin film deposition, the realisation of a Co/MgO/Co magnetic tunnel junction demonstrator and the development of dedicated numerical tools.

For what concerns the deposition apparatus, the system that has been realised is reliable and stable, its minimum operative pressure being  $9 \cdot 10^{-8}$  Torr and its lowest deposition rate  $13.6 \pm 0.3$  pm/s, allowing a great control over grown films. Since this machine has been customised, great importance has been given to future improvement capabilities, leaving a degree of freedom for experimenting new technologies.

The realised MTJ demonstrator exhibited a tunneling magnetoresistance of 0.1 % at 100 K, which is far from the best ever results reported in literature. Possible causes have been individuated in the geometry, in the wrong substrate and in the process design. In parallel, new hard spin injector alloys have been studied as future improvement of the device.

Finally, some interesting numerical algorithms have been developed in parallel to the experimental activity. Among them a genetic algorithm for experimental data fitting and a sophisticated image registration routine used to increment the signal to noise ratio and to extract magnetic texture characteristics from magnetic force microscope images. In particular the entropic analysis computed on registered, unbiased MFM maps acquired with an external magnetic field has shown the possibility of representing the magnetic properties in terms of a basically new approach, such as the texture trajectory and the magnetic

texture phase diagram.

# Bibliography

- [1] S. Das Sarma, *Am. Sci.* 89 (2001) 516-523;
- [2] F. Mott, *Proc. Roy. Soc. A* 153 (1936) 699;
- [3] R. Meservey and P. M. Tedrow, *Phys. Rev. Lett.* 26 (1971) 192-195;
- [4] M. Jullière, *Phys. Lett. A* 54 (1975) 225;
- [5] T. Miyazaki and N. Tezuka, *J. Magn. Magn. Mater.* 139 (1995) L231;
- [6] J. S. Moodera, L. R. Kinder, T. M. Wong, and R. Meservey, *Phys. Rev. Lett.* 74 (1995) 3273;
- [7] M. N. Baibich, J. M. Broto, A. Fert, F. Nguyen Van Dau, F. Petroff, P. Etienne, G. Creuzet, A. Friederich, and J. Chazelas, *Phys. Rev. Lett.* 61 (1988) 2472;
- [8] G. Binash, P. A. Grünberg, F. Saurenbach, and W. Zinn, *Phys. Rev. B* 39 (1989) 4828;
- [9] A. Fert, *Nobel Lecture, 8<sup>th</sup> December 2007*;
- [10] P. A. Grünberg, *Nobel Lecture, 8<sup>th</sup> December 2007*;
- [11] S. Datta and B. Das, *App. Phys. Lett* 56 (1990) 665;
- [12] M. Johnson, *IEEE Spectrum* 31 (1994) 47;
- [13] B. Huang, D. Monsma and B. Appelbaum, *Appl. Phys. Lett.* 91 (2007) 072501;
- [14] A. Chiolerio, P. Allia, A. Chiodoni, F. Pirri, F. Celegato and M. Coïsson, *J. App. Phys.* 101 (2007) 123915;
- [15] W. J. Gallagher and S. S. P. Parkin, *IBM J. Res. & Dev.* 50 (2006) 5;
- [16] S. I. Kiselev, I. N. Krivotorov, N. C. Emley, R. J. Schoelkopf, R. A. Buhrman and D. C. Ralph, *Nature* 425 (2003) 380;
- [17] S. Yuasa, *J. Phys. Soc. Jpn.* 77 (2008) 031001;
- [18] S. Murakami, N. Nagaosa and S. C. Zhang, *Science* 301 (2003) 1348;

- [19] W. H. Butler, X.-G. Zhang, T. C. Schulthess and J. M. McLaren, *Phys. Rev. B* **63** (2001) 054416;
- [20] J. Mathon and A. Umerski, *Phys. Rev. B* **63** (2001) 220403;
- [21] J. G. Simmons, *J. App. Phys.* **34** (1963) 1793;
- [22] M. B. Stearns, *J. Magn. Magn. Mater.* **5** (1977) 1062;
- [23] E. Y. Tsymbal, O. N. Mryasov and P. R. LeClair, *J. Phys.: Cond. Matt.* **15** (2003) R109;
- [24] J. Slonczewski, *Phys. Rev. B* **39** (1989) 6995;
- [25] J. M. de Teresa, A. Barthelemy, A. Fert, J. P. Contour, R. Lyonnet, F. Montaigne, P. Seneor and A. Vaurès, *Science* **286** (1999) 507;
- [26] J. S. Moodera and L. R. Kinder, *J. Appl. Phys.* **79** (1996) 4724;
- [27] S. Yuasa, T. Sato, E. Tamura, Y. Suzuki, H. Yamamori, K. Ando and T. Katayama, *Europhys. Lett.* **52** (2000) 344;
- [28] J. Z. Sun and D. C. Ralph, *J. Magn. Magn. Mater.* **320** (2008) 1227;
- [29] S. Zhang, P. M. Levy, A. Marley and S. S. P. Parkin, *Phys. Rev. Lett.* **79** (1997) 3744;
- [30] S. O. Valenzuela, D. J. Monsma, C. M. Marcus, V. Narayanamurti, M. Tinkham, *Phys. Rev. Lett.* **94** (2005) 196601;
- [31] P. LeClair, J. P. Kohlhepp, C. H. van de Vin, H. Wieldraaijer, H. J. M. Swagten and W. J. M. de Jonge *Phys. Rev. Lett.* **88** (2002) 107201;
- [32] W. Wulfhekel, H. F. Ding and J. Kirschner, *J. Magn. Magn. Mater.* **47** (2002) 242;
- [33] P. G. Mather, A. C. Perrella, E. Tan, J. C. Read and R. A. Buhrman, *Appl. Phys. Lett.* **86** (2005) 242504;
- [34] C. H. Shang, J. Nowak, R. Jansen and J. S. Moodera, *Phys. Rev. B* **58** (1998) R2917;
- [35] A. Vedyayev, D. Bagrets, A. Bagrets and B. Dieny, *Phys. Rev. B* **63** (2001) 064429;
- [36] L. F. Schelp, A. Fert, F. Fettar, P. Holody, S. F. Lee, J. L. Maurice, F. Petroff and A. Vaurès, *Phys. Rev. B* **56** (1997) R5747;
- [37] D. Ristoiu, J. P. Nozières, C. N. Borca, T. Komesu, H.-K. Jeong and P. A. Dowben *Europhys. Lett.* **49** (2000) 624;
- [38] J. H. Park, E. Vescovo, H. J. Kim, C. Kwon, R. Ramesh and T. Venkatesan, *Nature* **392** (1998) 794;

---

*Bibliography*

---

- [39] Y. Ji, G. J. Strijkers, F. Y. Yang, C. L. Chien, J. M. Byers, A. Anguelouch, G. Xiao and A. Gupta, *Phys. Rev. Lett.* **86** (2001) 5585;
- [40] C. Heiliger, P. Zahn, B. Yu, I. Yavorsky and I. Mertig, *preprint*;
- [41] S. S. P. Parkin, N. More and K. P. Roche, *Phys. Rev. Lett.* **64** (1990) 2304;
- [42] C. L. Platt, B. Dieny and A. E. Berkowitz, *J. Appl. Phys.* **81** (1997) 5523;
- [43] M. Sharma, S. X. Wang and J. H. Nickel, *Phys. Rev. Lett.* **82** (1999) 616;
- [44] C. L. Platt, B. Dieny and A. E. Berkowitz, *Appl. Phys. Lett.* **69** (1996) 2291;
- [45] M. Sharma, J. H. Nickel, T. C. Anthony and S. X. Wang, *Appl. Phys. Lett.* **77** (2000) 2219;
- [46] J. Wang, P. P. Freitas, E. Snoeck, P. Wei and J. C. Soares, *Appl. Phys. Lett.* **79** (2001) 4387;
- [47] J. S. Moodera, X. Hao, G. A. Gibson and R. Meservey, *Phys. Rev. Lett.* **61** (1988) 637;
- [48] Z. Li, C. de Groot and J. S. Moodera, *Appl. Phys. Lett.* **77** (2000) 3630;
- [49] P. LeClair, H. J. M. Swagten, J. T. Kohlhepp, R. J. M. van de Veerdonk and W. J. M. de Jonge, *Phys. Rev. Lett.* **84** (2000) 2933;
- [50] S. Yuasa, T. Nagahama, A. Fukushima, Y. Suzuki and K. Ando, *Nat. Mater.* **3** (2004) 868;
- [51] B. Window, *Surf. Coat. Tech.* **71** (1995) 93;
- [52] U. Mizutani, H. Hazama, T. Matsuda, Y. Yanagi, Y. Itoh, H. Ikuta, K. Sakurai and A. Imai, *Supercond. Sci. Tech.* **16** (2003) 1207;
- [53] A. Chiolerio, P. Martino, *Vacuum Int.* **2** (2008) 2;
- [54] W. Nicodemi, *Acciai e leghe non ferrose*, Zanichelli (2000) ISBN 88-08-03237-X;
- [55] V. Nemanic, B. Zajec and J. Setina, *J. Vac. Sci. Tech. A*, **19** (2001) 215;
- [56] K. Jousten, *Vacuum*, **49** (1998) 359;
- [57] B. Ferrario, *Introduzione alla tecnologia del vuoto*, Pàtron (1999) ISBN 88-555-2510-7;
- [58] P. Rottlander, H. Kohlstedt, H. A. M. de Gronckel, E. Girgis, J. Schelten and P. Grünberg, *J. Magn. Magn. Mater.*, **210** (2000) 251;
- [59] X.-G. Zhang and W. H. Butler, *Phys. Rev. B*, **70** (2004) 172407;
- [60] H. L. Meyerheim, R. Popescu, J. Kirschner, N. Jedrecy, M. Sauvage-Simkin, B.

- Heinrich and R. Pinchaux, *Phys. Rev. Lett.*, 87 (2001) 076102;
- [61] S. Yuasa, A. Fukushima, H. Kubota, Y. Suzuki and K. Ando, *Appl. Phys. Lett.*, 89 (2006) 042505;
- [62] S. S. P. Parkin, C. Kaiser, A. Panchula, P. M. Rice, B. Hughes, M. Samant and S.-H. Yang, *Nat. Mater.*, 3 (2004) 862;
- [63] D. D. Djayaprawira, K. Tsunekawa, M. Nagai, H. Maehara, S. Yamagata, S. Yuasa, Y. Suzuki and K. Ando, *Appl. Phys. Lett.*, 86 (2005) 092502;
- [64] Y. M. Lee, J. Hayakawa, S. Ikeda, F. Matsukura and H. Ohno, *Appl. Phys. Lett.*, 90 (2007) 212507;
- [65] K. Tsunekawa et al., *IEEE Int. Magnetics Conf. (Intermag)*, (2005) HP-08;
- [66] W. G. Wang, C. Ni, A. Rumaiz, Y. Wang, X. Fan, T. Moriyama, R. Cao, Q. Y. Wen, H. W. Zhang and J. Q. Xiao, *Appl. Phys. Lett.*, 92 (2008) 152501;
- [67] T. Dimopoulos, G. Gieres, J. Wecker, N. Wiese, Y. Luo and K. Samwer, *J. Appl. Phys.*, 98 (2005) 073705;
- [68] S. Yoshimura, Y. Narisawa, Y. Watanabe, M. Tsunoda and M. Takahashi, *J. Magn. Magn. Mater.*, 312 (2007) 176;
- [69] M. Hehn, C. de Buttet, G. Malinowski, E. Snoeck, C. Tiusan and F. Montaigne, *Eur. Phys. J. B*, 40 (2004) 19;
- [70] J. S. Moodera and G. Mathon, *J. Magn. Magn. Mater.*, 200 (1999) 248;
- [71] M. Justus, H. Brückl and G. Reiss, *J. Magn. Magn. Mater.*, 240 (2002) 212;
- [72] Y. C. Feng, D. E. Laughlin and D. N. Lambeth, *IEEE Trans. Magn.*, 30 (1994) 6;
- [73] M. Coisson, C. Appino, F. Celegato, A. Magni, P. Tiberto and F. Vinai, *Phys. Rev. B*, 77 (2008) 214404;
- [74] A. Chiolerio, P. Martino, M. Coisson and P. Allia, *J. Magn. Magn. Mater.*, submitted 09 Oct 2008;
- [75] A. Pundt and C. Michaelsen, *Phys. Rev. B*, 56 (1997) 14352;
- [76] A. Chiolerio, A. Chiodoni and P. Allia, *Thin Solid Films*, 516 (2008) 8453;
- [77] A. Chiolerio, P. Allia, P. Tiberto and M. Coisson, *J. Phys. Cond. Mat.* 20 (2008) 345213;
- [78] J. H. Holland, *Adaptation in natural and artificial systems* (1992) Cambridge, MA: MIT press;

- [79] K. Chwastek and J. Szczyglowski, *Math. Comput. Simul.* 71 (2006) 206;
- [80] A. Chiolerio, E. Celasco, F. Celegato, S. Guastella, P. Martino, P. Allia, P. Tiberto and F. Pirri, *J. Magn. Magn. Mater.* 320 (2008) e669-e673;
- [81] B. Zitova and J. Fussler, *Image and Vision Computing* 21 (2003) 977;
- [82] Y. Jianchao, C. T. Chiern, Y. C. Hwang and Y. C. L. Adrian, *Geoscience and Remote Sensing Symposium, IEEE 2001 International* 7 (2001) 3297;
- [83] Y. Xiong and F. Quek, *4<sup>th</sup> IEEE International Conference on Computer Vision Systems Proceedings, January 2006, New York City (NY) USA*;
- [84] A. Goshtasby, G. C. Stockman and C. V. Page, *IEEE Trans. Geosc. Rem. Sens.* 24 (1986) 390;
- [85] A. Goshtasby, *Pattern Recognition* 19 (1986) 459;
- [86] H. J. Hug, B. Stiefel, P. J. A. van Schendel, A. Moser, R. Hofer, S. Martin, S. Porthun, L. Abelmann, J. C. Lodder, G. Bochi and R. C. O'Handley, *J. Appl. Phys.* 83 (1998) 5609;
- [87] T. Chang, M. Lagerquist, J.-G. Zhu, J. H. Judy, P. B. Fischer and S. Y. Chou, *IEEE Trans. Magn.* 28 (1992) 3138;
- [88] X. Che, M. Lederman, G. A. Gibson, H. N. Bertram and S. Schultz, *J. Appl. Phys.* 73 (1993) 5805;
- [89] M. V. Rastei, R. Meckenstock and J. P. Bucher, *Appl. Phys. Lett.* 87 (2005) 222505;
- [90] W. Jacquet and P. De Groen, *ArXiv 0705.3593v2*, 19 June 2007;
- [91] A. Pinz, M. Prantl and H. Ganster, *J. Univers. Comput. Sci.* 1 (1995) 614;
- [92] J. Jian-qiu, W. Zhang-ye and P. Qun-sheng, *J. Zhejiang Univ. Sci.* 6A (2005) 94;
- [93] R. C. Gonzalez, R. E. Woods and S. L. Eddins, *Digital Image Processing using MATLAB*, (2003) New Jersey, Prentice Hall, chap. 11;
- [94] A. Chiolerio, P. Allia, E. Celasco, P. Martino, F. Spizzo, F. Celegato, *J. Magn. Magn. Mater.*, submitted 24 Sep 2008;
- [95] W. F. Egelhoff, R. D. McMichel, C. L. Dennis, M. D. Stiles, A. J. Shapiro, B. B. Maranville and C. J. Powell, *IEEE Trans. Magn.* 42 (2006) 2664;
- [96] D. O. Soares-Pinto, M. S. Reis, R. S. Sarthour and I. S. Oliveira, *J. Stat. Mech.*, 08 (2007) P08011;
- [97] M. S. Reis, V. S. Amaral, R. S. Sarthour and I. S. Oliveira, *Phys. Rev. B*, 73 (2006)

*Bibliography*

---

- 092401;  
[98] C. Beck and E. G. D. Cohen, *Physica A*, 322 (2003) 267.

# Index

- Affine transform, Image Registration, 88  
Alternating gradient force magnetometry, (AGFM), 43, 66  
Alumina, tunnel barrier, 5, 17  
Antiferromagnetic (AFM), pinning layer, 13, 40  
APIEZON ® H, 27  
Ar pressure effect, sputtering, 41  
Atomic force microscopy, AFM, 42  
Austenitic stainless steel, 26  
  
Baking, vacuum vessel, 26  
Base image, Image Registration, 86  
Bayard-Alperth vacuum sensor, 21  
Bias dependence, TMR, 13  
Bloch analysis, 92  
Boltzmann-Gibbs-Shannon statistics (BGS), 92  
  
Capacitive vacuum sensor, 21  
Chromosome, Genetic Algorithm, 74  
CoCr, hard layer, 5, 62, 97  
CoFeB, soft layer, 5  
Colormap, matricial analysis, 79  
Conformal transform, Image Registration, 88  
Copper flanges, CF, 22  
  
Coulomb blockade effects, TMR, 15  
Creep, Image Registration, 85  
Cross-correlation factor, 79  
Crossover, Genetic Algorithm, 77  
  
Damping factor, Genetic Algorithm, 78  
DAQ control, 30  
Datta-Das transistor, 3  
DC brushless motor, 30  
Density of states, DOS, 9, 10  
Deposition rate, 42, 48, 49  
Deposition time effect, sputtering, 42  
Deuterium lamp, 35, 48  
Dewetting, 42, 47, 66  
Differential matrix, magnetic, 86  
Differential matrix, topographic, 86  
dynamical electrical contact, 33  
  
Electric tunnel effect, 6  
Elitism, Genetic Algorithm, 79  
Energy dispersive X-ray analysis (EDX), 65  
Epitaxial MTJs, 5, 16, 39  
Expression matrix, Genetic Algorithm, 75  
Extremely low interstitial stainless steels, ELI, 26  
  
Fert A., 1

---

**INDEX**

---

- Field cooling, 35  
Field effect scanning electron microscopy, (FESEM), 42  
Finite impulse response (FIR) filtering functions, 70  
Fitness, Genetic Algorithm, 75  
Fluoroelastomeric o-ring, 27  
Fuchs-Sondheimer model, 59  
  
Gate valve, 23  
Gene, Genetic Algorithm, 75  
Generation, Genetic Algorithm, 75  
Genetic Algorithm, 74  
Giant magnetoresistance (GMR), 2  
Giant TMR, GTMR, 17, 39  
Grünberg P.A., 1  
Grain branching factor, 44, 46  
Grain equivalent diametre, 44, 47  
Grain equivalent eccentricity, 44, 47  
Grain relative orientation, 44  
Grey level co-occurrence matrix, (GLCM), 92  
Greyscale vector, matricial analysis, 80, 86  
  
Half-metallic ferromagnets, 15  
Hard disk read heads, 4, 21, 39  
Hard layer, 13  
Heusler alloys, 15  
Histogram, Image Registration, 87  
Hot electron spin transistor, 3  
  
Image registration for matricial data handling, 84  
Individual, Genetic Algorithm, 74  
Input image, Image Registration, 86  
IV, measure, 55  
Johnson transistor, 3  
Jullière M., 2  
Jullière, polarisation model, 10  
  
K type thermocouple, 31  
  
LASER microablation, 51, 53  
Load-lock chamber, 35  
  
Magnesia, tunnel barrier, 5, 14, 17, 39, 53, 59, 61  
Magnetic force microscopy, (MFM), 43, 65  
Magnetic random access memories, (MRAMs), 4, 21, 39  
Magnetic texture phase diagram (MTPD), 93, 98  
Magnetic tunneling junction (MTJ), 4  
Magnetron, 29  
Mass flow control, MFC, 27  
Meservey R., 1, 9  
MFM, Image Registration, 85  
Miyazaki T., 2  
Moodera J. S., 2  
Moore law, 1  
Mott F., 1  
Multidimensional array, 92  
Multitarget sputtering, 21  
Mutation, Genetic Algorithm, 77  
N type thermocouple, 31

---

## INDEX

---

- Numerical extrapolation of curve characteristics, 43, 70
- Numerical grain analysis, 43, 47, 81
- Outgassing rate, 27
- Oxygen free copper, OFC, 33
- Parametre space, Genetic Algorithm, 75
- Patterned magnetic materials, Image Registration, 86
- Piecewise cubic Hermite interpolating polynomials (PCHIP), 73
- Piecewise linear transform, Image Registration, 88
- Pirani vacuum sensor, 21
- Policrystalline MTJs, 40
- Polynomial transform, Image Registration, 88
- Population, Genetic Algorithm, 74
- Projective transform, Image Registration, 88
- R versus T, measure, 55
- Radiative oven, 31
- Real-time resistance measure, 59
- Resistance per area product, RA, 39
- RF generator, 29
- RF power effect, sputtering, 41
- RF switch, 29
- Roulette wheel, Genetic Algorithm, 77
- Savitzky-Golay functions, SGFs, 70, 71
- Shannon entropy, 92
- Shutter, 30
- Slonczewski J., 11
- Slonczewski, polarisation model, 12
- Sobel filter, Image Registration, 88
- Soft layer, 13
- Solid phase epitaxy, 40
- Spatial transformation applications, Image Registration, 88
- Spin dependent tunneling, SDT, 6
- Spin transfer nano-oscillators (STNOs), 4
- Spin-flip scattering, 10, 14
- Spin-valve, 3
- Spintronics, overview, 1
- Static pressure curve, 27
- Stearns, polarisation model, 10
- Substrate temperature effect, sputtering, 41
- Syntethic antiferromagnet, SAF, 16
- Systematic error map, Image Registration, 91
- Target holder, 29
- Tedrow P., 1, 9
- Tedrow, polarisation model, 9
- Temperature dependence, TMR, 14
- Texture trajectories diagram (TTD), 93, 98
- Textured MTJs, 40
- Tezuka N., 2
- Thermal evaporation, 40, 51, 53, 59, 63
- Thresholding algorithm, 43, 82, 86
- Throttle valve, 23
- TMR, expression, 11
- TMR, measure, 54, 55
- Tunneling magnetoresistance (TMR), 2

*INDEX*

---

- Ultra-high-vacuum, UHV, 22, 23
- Vecotrial vibrating sample magnetometre, VSM,
  - 65
- Vectorial data handling, 69
- Wiener filter, Image Registration, 87